



# Time-lens oscilloscope of optical signal packets by nonlinear optics

Eva Ryckeboer

Examiner: Prof. Eilert Berglind  
Supervisor: dr. Ir. Mark Pelusi  
Assisting supervisor: Prof. Ben Eggleton

Master dissertation submitted in order to obtain the academic degree of  
Erasmus Mundus Master of Science in Photonics

Academic year 2008-2009



Vrije Universiteit Brussel



University  
of  
St Andrews



# Abstract

The demand for more bandwidth necessitates an increase in the data-rates of optical telecommunication systems. Continuously new all-optical techniques are developed to measure and process the sent ultrashort pulses with femtosecond accuracy. This thesis work focusses on the time-lens oscilloscope architecture which allows us to characterise sub-picosecond pulses. It is a so-called temporal imaging system that can easily be understood by comparison with a classical thin lens imaging system. Just like Fraunhofer diffraction after a thin lens results in the spatial Fourier transform of the incident field at the focal plane of the thin lens, the time-lens architecture performs a (temporal) Fourier transform on the incident pulse under test. The output pulse thus yields the spectrum of the incident pulse. Consecutive measurement of that output pulse with an optical spectrum analyser, gives the temporal waveform of the input pulse. State-of-the art time-lens oscilloscopes provide the measurement of signals with 200 fs resolution over a record length of 150 ps. By means of simulations we investigate in detail the most up-to-date time-lens architecture which exploits four-wave-mixing in a nonlinear medium. Based on the simulation results, we developed a new four-wave-mixing time-lens architecture using a reconfigurable pulse shaper to overcome the most important source of aberrations. Furthermore it is the first tuneable implementation of a time-lens architecture with femtosecond resolution. The first experimental results demonstrate the measurement of a 1 ps Sech pulse and a 25 ps long pulse train. The overall performance and limitations of our proposed implementation are determined to allow comparison with alternative pulse characterisation techniques and state-of-the art time-lens oscilloscopes.

# Acknowledgements

Firstly, I would like to thank my supervisors at CUDOS, Mark Pelusi and Ben J. Eggleton. It was a great opportunity to write my thesis at the University of Sydney and their encouragement and advice helped me a lot to finish my thesis successfully. I would also like to thank Professor Eilert Berglind, to take up the difficult task of examiner for this long-distance thesis project. Secondly, the experimental part of my thesis work had never succeeded if I didn't get the great help of Aisling Clarke and Jurgen Van Erps. Finally, I have so many good memories of the support of my friends in Sydney. They helped me to relax if I was tired or frustrated about the progress of my thesis project. Also all discussions about life, art and research with Lisa Roberts stimulated me enormously. I gained so many exciting academic and personal experiences. Of course I would also like to thank my family. Despite the long distance, we kept close contact. They motivated me to enjoy every second of my period here to the fullest.

# Statement of contribution of the student

I performed all simulations in this work using a Matlab® code written by myself for the ideal time-lens set-up. For the four-wave-mixing time-lens set-up, I wrote my own Matlab® code using one Matlab® function written by Michael Lamont. Other simulations to show the influence of all design parameters were made by myself. I designed all the experiments apart from the pulse burst experiment. The experiments were performed by Dr. Aisling Clarke as she has in depth experience with the Waveshaper® equipment. I collaborated with Dr. Aisling Clarke and my supervisors Dr. Mark Pelusi and Dr. Ben Eggleton to discuss the experimental results. During these discussions we also decided the future directions of the project.

I certify that this thesis contains work carried out by myself  
except where otherwise acknowledged.

Eva Ryckeboer 12th June 2009

# Contents

<b>1</b>	<b>Introduction</b>	<b>1</b>
<b>2</b>	<b>Theory of temporal imaging</b>	<b>4</b>
2.1	Introduction . . . . .	4
2.2	Space-time duality theory . . . . .	4
2.2.1	Origin duality . . . . .	4
2.2.2	Fundamental equations: . . . . .	6
2.3	Time-lens concept . . . . .	9
2.3.1	Thin lens action . . . . .	10
2.3.2	Time-lens action . . . . .	10
2.3.3	Focal time . . . . .	11
2.3.4	Temporal aperture: . . . . .	11
2.3.5	f-number . . . . .	12
2.4	Imaging systems . . . . .	12
2.4.1	Magnification regime . . . . .	13
2.4.2	Fourier transform regime . . . . .	14
2.5	Performance of temporal imaging systems . . . . .	20
2.5.1	Resolution . . . . .	20
2.5.2	Aberrations . . . . .	21
2.6	Conclusion . . . . .	22

---

<b>3</b>	<b>Literature review</b>	<b>24</b>
3.1	Introduction . . . . .	24
3.2	Time-lens methods and experimental set-ups . . . . .	24
3.2.1	Electro-optic modulator as time-lens . . . . .	24
3.2.2	XPM with parabolic pulses as time-lens . . . . .	27
3.2.3	FWM with chirped pulses as time-lens . . . . .	29
3.3	Alternative pulse measurement schemes . . . . .	34
3.3.1	Autocorrelation . . . . .	35
3.3.2	FROG . . . . .	36
3.3.3	Optical sampling . . . . .	37
3.4	Conclusion . . . . .	38
<b>4</b>	<b>Design guidelines and optimisation of the FWM time-lens set-up</b>	<b>39</b>
4.1	Introduction . . . . .	39
4.2	Split-step Fourier method . . . . .	40
4.3	Ideal time-lens . . . . .	41
4.3.1	Proof-of-concept . . . . .	41
4.3.2	Sensitivity to the Fourier transform condition . . . . .	45
4.4	FWM time-lens via NLS . . . . .	45
4.4.1	Proof-of-concept . . . . .	45
4.5	Design guidelines . . . . .	48
4.5.1	Length dispersive element . . . . .	49
4.5.2	Temporal overlap . . . . .	50
4.5.3	Spectral overlap . . . . .	54
4.5.4	Walk-off in HNLF . . . . .	57
4.6	Design strategy for a Gaussian signal . . . . .	58
4.7	Implementation for bit patterns . . . . .	61
4.7.1	Multiple-bit shot . . . . .	62
4.8	Optimization of the FWM set-up with use Waveshaper <sup>®</sup> equipment . . . . .	64
4.9	Conclusion . . . . .	65

<b>5</b>	<b>Design and simulation experiments with Waveshaper® set-up</b>	<b>66</b>
5.1	Introduction . . . . .	66
5.2	Specific Equipment . . . . .	66
5.2.1	Erbium doped fiber laser . . . . .	67
5.2.2	Waveshaper® . . . . .	68
5.2.3	Chalcogenide chip . . . . .	70
5.3	Experiment with FWM in HNLF . . . . .	71
5.3.1	Design experiment 1 . . . . .	71
5.3.2	Simulation experiment 1 . . . . .	71
5.3.3	Design experiment 2 . . . . .	74
5.3.4	Simulation experiment 2 . . . . .	75
5.4	Fundamental limitations of the Waveshaper® set-up . . . . .	76
5.5	Conclusion . . . . .	77
<b>6</b>	<b>Experimental results</b>	<b>78</b>
6.1	Introduction . . . . .	78
6.2	Experiment in HNLF . . . . .	78
6.2.1	Experiment I: 1ps Sech input pulse . . . . .	78
6.2.2	Experiment II: Asymmetric pulse . . . . .	81
6.2.3	Experiment III: Pulse burst . . . . .	82
6.2.4	Experiment IV: Sensitivity to the Fourier transform condition . . . . .	83
<b>7</b>	<b>Conclusions and future directions</b>	<b>85</b>
<b>A</b>		<b>87</b>
A.1	Phase function thin lens . . . . .	87
A.2	Impulse response temporal imaging system . . . . .	88
A.3	Magnification regime . . . . .	89
A.4	Waveguide parameters . . . . .	91
	<b>Bibliography</b>	<b>93</b>
	<b>List of Figures</b>	<b>97</b>



## List of Acronyms

**DCF:** Dispersion Compensating Fiber  
**DWP:** Waveshaper®  
**FOD:** Fourth Order Dispersion  
**EDFA:** Erbium doped fiber amplifier  
**FROG:** Frequency Resolved Optical Gating  
**FWHM:** Full Width Half Maximum  
**FWM:** Four-Wave-Mixing  
**GDD:** Group Delay Dispersion  
**GVD:** Group Velocity Dispersion  
**HNLF:** Highly Non Linear Fiber  
**NLS:** Non Linear Schrödinger equation  
**OSA:** Optical Spectrum Analyser  
**SHG:** Second Harmonic Generation  
**SMF:** (standard) Single Mode Fiber  
**SPM:** Self Phase Modulation  
**TOD:** Third Order Dispersion  
**XPM:** Cross Phase Modulation  
**ZDW:** Zero Dispersion Wavelength

## List of Symbols

$\alpha$ : attenuation constant  
 $\beta_2$ : second order dispersion parameter  
 $\beta_3$ : third order dispersion parameter  
 $\beta_4$ : fourth order dispersion parameter  
 $\gamma$ : nonlinear parameter  
 $\lambda$ : wavelength  
 $\tau$ : time parameter in the traveling-wave coordinate system  
 $\tau_{FWHM}$ : FWHM temporal width  
 $\tau_s$ : FWHM temporal width of signal  
 $\tau_p$ : FWHM temporal width of pump pulse  
 $\tau_{rec}$ : record length  
 $\tau_{res}$ : temporal resolution  
 $\omega_0$ : optical carrier frequency  
 $\Omega$ : base-band frequency  $\Omega = \omega - \omega_0$   
C: chirp parameter for Gaussian pulse  
D: total dispersion  $D = \beta_2 L$   
 $D_f$ : focal group delay dispersion  
 $f_T$ : focal time  
 $f^\#$ : f-number  
**i**: imaginary unit  
k: wavenumber  $k = \frac{2\pi}{\lambda}$   
K: chirp rate  
L: length of dispersive element  
m: order of super-Gaussian pulse  
 $n_2$ : nonlinear index  
S: dispersion slope  
v: speed of light in the medium  
 $v_g$ : group velocity  
z: distance parameter in the traveling-wave coordinate system

# Chapter 1

## Introduction

With the advent of femtosecond lasers and new insights into the possibilities of nonlinear optics, a new field of optical measurement techniques with femtosecond accuracy has opened up. The need for high resolution measurements is driven by interest in ultrafast chemical and physical phenomena and in ever increasing data rates in telecommunication systems. In the near future, these increasing data rates will necessitate data pulses with femtosecond duration, thus at the receiver side femtosecond resolution will be needed to read the sent information. In addition to high resolution, single-shot techniques are required to capture rapid time-varying and/or non-repetitive events. Using a single-shot technique makes sure that no averaging over the signal shape occurs. As the inevitable bandwidth limitations of electronic devices makes them insufficient for femtosecond waveform characterizations, optical solutions are the way to go.

Several nonlinear optical pulse measurement techniques are now utilized in high-bandwidth laboratories, of which the most popular are the autocorrelator and spectrographic methods like Frequency Resolved Optical Gating (FROG). The autocorrelator is a fast device but it can only give a rough estimate of the shape and duration of the pulse. Spectrographic methods offer the needed femtosecond accuracy and an acceptable single-shot record length of about 10 ps. But spectrographic devices need reconstruction algorithms for the final measurement output which makes them slow.

Recently a very interesting and potentially fully on-chip optical oscilloscope was developed with 220 fs resolution and a record length of more than 100 ps [*M.A. Foster et al. Nature 456, 81-84 (2008)*][1]. The imaging system is fully analogous to a spatial imaging system with a lens working in the Fraunhofer regime which offers a 2D spatial Fourier transform of the input field. The optical oscilloscope performs the Fourier transform of the incident temporal

waveform, essentially returning its optical spectrum. Hence the measurement of the spectrum at the Fourier plane yields the temporal amplitude of the incident waveform, allowing a direct measurement of the latter.

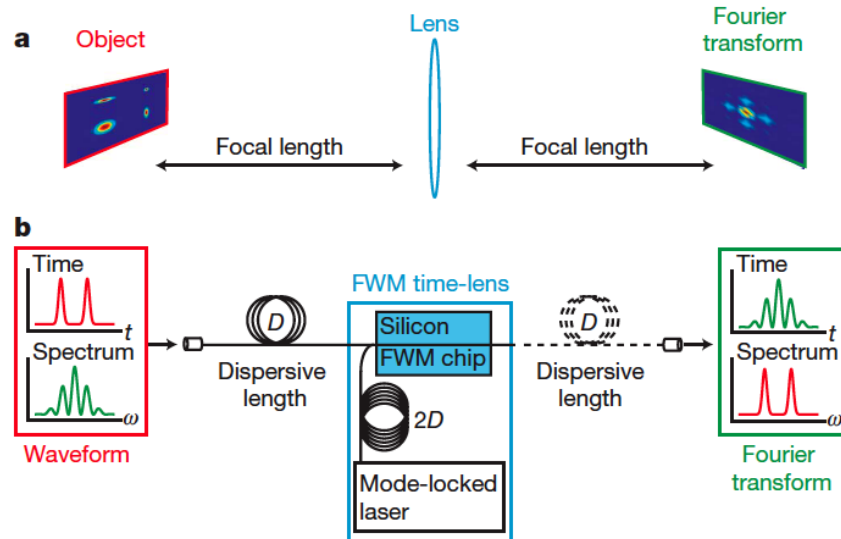


**Figure 1.1:** **a.** A spatial optical Fourier transform processor. **b.** A temporal optical Fourier transform processor. *M.A. Foster et al. Nature 456, 81-84 (2008)*[1]

A simple schematic as shown in figure 1.1 makes this visually clear. The principle of operation relies on the space-time duality between the equations governing paraxial diffraction and narrow-band dispersion. Replacing all elements of a spatial imaging system (diffractive element, lens) by its temporal analogs (dispersive element, time-lens) constitutes a temporal imaging system that allows for the above described Fourier transform property or e.g. temporal magnification (stretching of signals).

It is not the first time that a time-lens has been used in a temporal imaging system. Earlier implementations used for example an electro-optic modulator as a time-lens [2]. As this modulator is controlled by electronics, it is too slow for femtosecond operation. The shift to an optical solution was needed to make the time-lens imaging system capable of measuring femtosecond pulses.

The beauty of the proposed setup lies in the fact that the time-lens action is performed optically on a 1.5 cm silicon chip and the dispersive optical fibers used are potentially integratable on the same chip. At the same time it has some unsatisfying properties, leading to this thesis research.

Firstly, as long as the dispersive lengths are not integrated, the fiber lengths used countermands the compactness of the elegant chip-based solution. The question thus arises: is the reported 50m of dispersive fiber necessary to obtain their attractive results?

Secondly, the dispersive elements should only impose second-order dispersion for optimal performance and the inevitable third-order-dispersion (TOD) in the fiber causes limiting aberrations.

Finally, the proposed set-up is a very static implementation. We will show that the performance can be optimized by utilising a more flexible set-up.

An important added value of this thesis research is the new approach to the TOD aberration problem. Instead of using dispersive fibers we will use the advanced Waveshaper<sup>®</sup> equipment which can shape the amplitude and phase of pulses before we send them into the time-lens, hereby completely removing the source of TOD. Moreover the Waveshaper is a programmable device, allowing a dynamic implementation. We will also replace the silicon chip by a chalcogenide chip with the same functionality, as chalcogenide has no unwanted two-photon-absorption and free-carrier effects, which limit the dynamic range. Moreover, as the setup is a very delicate interplay of many actors and nonlinear effects, this project aims to elucidate the influence of all design parameters through simulation and experiment.

The structure of this thesis is as follows: In Chapter 2 we explain the theory of temporal imaging which forms the essential background for understanding temporal imaging systems. In Chapter 3 the key experiments of the past are reviewed as well as some alternative measurement techniques. The aim of Chapter 4 is to give a complete framework to understand the influence of all parameters and to develop a design strategy. With this knowledge we design and simulate the experiments as shown in Chapter 5. The results of the measurements performed in the lab are presented and discussed in Chapter 6. We conclude the work done and reflect on possible future directions in the final Chapter 7.

## Chapter 2

# Theory of temporal imaging

### 2.1 Introduction

This chapter begins with the basics in space-time duality theory. It examines the origins of this duality and overviews the fundamental equations of the theory. The applications of space-time duality theory lead to the concept of a time-lens which is analogous to a normal (thin) lens. Hence in the second section we elucidate the time-lens formalism. A lens is generally used in spatial imaging systems, this corresponds via the space-time duality to a time-lens, used in 'temporal' imaging systems. These can have a magnifying action (stretch a signal in time) or a Fourier transform property, yielding the spectrum of the incoming signal. After expanding on the basics of these two types of temporal imaging systems we discuss shortly the main performance issues of temporal imaging systems namely their resolution and (possible) aberrations.

### 2.2 Space-time duality theory

#### 2.2.1 Origin duality

There exists an intriguing duality between paraxial diffraction and narrow-band dispersion. The former is a fundamental property of propagating waves, manifesting itself in the spreading out of a wave when it passes through a small aperture. Important for our duality is the fact that the wave spreads out in space. This is shown in figure 2.2 [3]. Analogously, the dispersion phenomenon acts on modulated waves or pulses. When a pulse travels through a dispersive medium, it spreads out in time. The main reason for this is that modulated waves contain different frequencies which all have a slightly different speed as the refractive index of nearly every medium is frequency-dependent. As a result after a small distance not

all frequencies have travelled the same distance and the pulse is broadened in time. While diffraction causes the wave to spread out in space, dispersion imparts broadening in time. This duality is called space-time duality and has been known about 50 years [4, 5, 6].

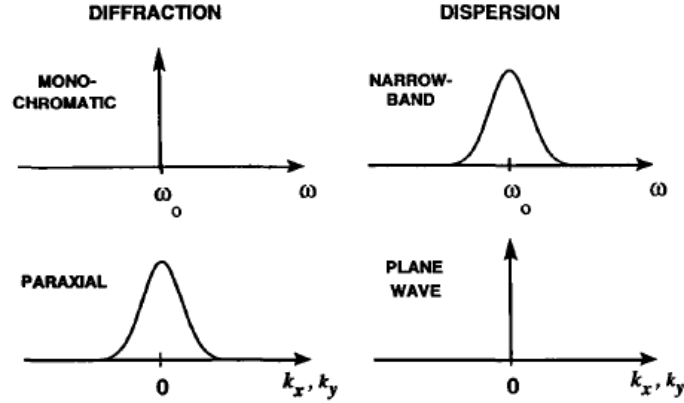


**Figure 2.1:** Duality between the assumptions for paraxial diffraction and narrow-band dispersion. [7]

We now take a closer look why the adjectives paraxial and narrow-band are used to specify the duality. For paraxial diffraction we consider a monochromatic wave with carrier frequency  $\omega_0$ , which leads to a delta function in the temporal-frequency spectrum at  $\omega_0$ . The paraxial approximation, which says that a wave is confined along the direction of the  $k_0$ -vector, means that the wave has a narrow band of spatial frequencies. In 2.5.1 we explain the spatial frequency concept more thoroughly but for now it is just important to know that the largest spatial frequency is a measure for the confinement of the wave. For dispersion it is the other way around: we assume a narrow-band temporal-frequency spectrum as we describe the evolution of modulated waves. At the same time we ignore the spatial profile of the wave and treat the wave as an infinite plane wave propagating along the z-axis. The spatial frequency spectrum reduces to a delta-function as the wave is perfectly aligned with the z-axis. The complementary characteristics are shown in figure 2.1.

Beyond this intuitive reasoning, simple mathematical derivations show that the equations which govern both diffraction and narrow-band dispersion belong to the same mathematical class of parabolic differential equations to which the heat diffusion equation also belongs. In order to understand the space-time duality concept more fully, we examine the governing equations in detail.

## 2.2.2 Fundamental equations:

We derive the equation for paraxial diffraction, and for the narrow-band dispersion equation we show that it is a simplified version of the nonlinear Schrödinger equation which describes the pulse evolution in a nonlinear dispersive medium. Of course one can also derive the narrow-band dispersion equation directly, as shown in reference [8], but in the framework of this thesis it is useful to introduce the important nonlinear Schrödinger equation.

### Paraxial diffraction:

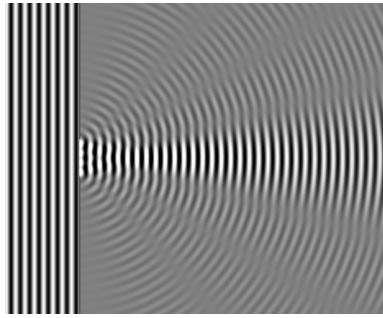


**Figure 2.2:** Diffraction of a monochromatic wave when passing through a slit [3].

We start off with determining the equation for paraxial diffraction. We use the (scalar) wave theory of light in which we represent light by a real scalar function  $u(\mathbf{r},t)$  which satisfies the wave equation  $\nabla^2 u - \frac{1}{v^2} \frac{\partial^2 u}{\partial t^2} = 0$ , with  $v$  the speed of the wave in the medium. The scalar function  $u(\mathbf{r},t)$  has the complex representation  $U(\mathbf{r},t)$  such that  $u(\mathbf{r},t) = \text{Re}\{U(\mathbf{r},t)\}$  in the (quasi-)monochromatic case. Assume a monochromatic paraxial wave propagating along the  $z$ -axis. We can represent the wave by its complex amplitude  $U(\mathbf{r}) = E(\mathbf{r}) \exp(-i k z)$ , with  $k = \frac{2\pi}{\lambda}$ . A paraxial wave has a complex envelope  $E(\mathbf{r})$  which is slowly varying with position compared to the wavelength  $\lambda$ . This implies the following conditions:

1.  $|\frac{\partial^2 E}{\partial z^2}|^2 \ll |\frac{\partial^2 E}{\partial x^2}|^2$
2.  $|\frac{\partial^2 E}{\partial z^2}|^2 \ll |\frac{\partial^2 E}{\partial y^2}|^2$
3.  $|\frac{\partial^2 E}{\partial z^2}|^2 \ll |2k \frac{\partial E}{\partial z}|$

These conditions basically mean that “*the curvature of the field envelope in the direction of propagation is much less than the curvature of the transverse profile*” [7]. The monochromatic assumption leads to the Helmholtz equation for  $U(\mathbf{r})$  which is used in diffraction theory.

Incorporating all assumptions stated above in the Helmholtz equation leads to the paraxial Helmholtz equation which governs the evolution of the slowly-varying envelope  $E(\mathbf{r})$  of the wave:

$$\frac{\partial^2 E}{\partial x^2} + \frac{\partial^2 E}{\partial y^2} - 2ik \frac{\partial E}{\partial z} = 0 \quad (2.1)$$

In shortened form using the transverse laplacian operator  $\nabla_t^2$  the equation is:

$$\frac{\partial E}{\partial z} = -\frac{i}{2k} \nabla_t^2 E \quad (2.2)$$

which is a parabolic equation.

### Narrow-band dispersion:

For narrow-band dispersion we show that we can simplify the nonlinear Schrödinger (NLS) equation to end up with the parabolic equation we are looking for. Consider the pulse:  $E(\mathbf{r}, t) = A(z, t) \exp(i(\omega_0 t - \beta_0 z))$ . The evolution of its slowly varying pulse envelope  $A(z, t)$  is described by the nonlinear Schrödinger equation which is stated here [9]:

$$\frac{\partial A}{\partial z} = -\frac{i}{2} \beta_2 \frac{\partial^2 A}{\partial \tau^2} + \frac{1}{6} \beta_3 \frac{\partial^3 A}{\partial \tau^3} + \frac{i}{24} \beta_4 \frac{\partial^4 A}{\partial \tau^4} - \frac{\alpha}{2} A + i\gamma |A|^2 A - \frac{\gamma}{\omega_0} \frac{\partial}{\partial \tau} (|A|^2 A) - i\gamma T_R A \frac{\partial}{\partial \tau} (|A|^2) \quad (2.3)$$

The above stated NLS equation 4.1 is derived assuming the  $\exp(-i\omega_0 t)$  dependence. In the rest of this thesis we work with the opposite convention  $\exp(i\omega_0 t)$ . In the NLS equation the traveling-wave coordinate system is introduced, which is defined via the following two variables:

$$\tau = (t - t_0) - \frac{(z - z_0)}{v_g}, \quad \xi = z - z_0 \quad (2.4)$$

This coordinate system is equivalent with ignoring the average pulse delay connected with the group velocity  $v_g$ . We choose  $z_0 = 0$  so that we can replace  $\xi$  by  $z$ .

This equation covers many linear and nonlinear effects which affect the pulse shape and spectrum. We now assign a *physical phenomenon* to every term of equation 4.1.

All terms  $\beta_j$  with  $j = \text{index}$  describe how dispersion affects the pulse to different orders. Dispersion is a linear effect, which broadens the pulse but doesn't affect the spectrum. It can be easily understood by considering that different frequencies travel at different speeds through the fiber due to group-velocity dispersion (GVD). As the different frequencies get delayed with respect to each other they don't arrive at the same time and thus the pulse spreads out. This is shown in figure 2.3. The term  $\alpha$  (attenuation constant) is a measure for the losses in the medium. All terms containing  $\gamma$  (nonlinear parameter) describe various nonlinear effects. The first term to include  $\gamma$  represents effects caused by the optical Kerr effect, the second term in  $\gamma$  reflects self-steepening and the third term in  $\gamma$  describes stimulated Raman scattering (SRS).



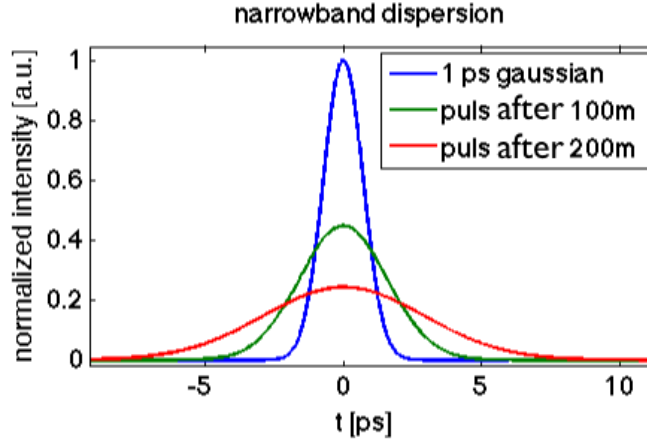


**Figure 2.3:** Narrowband dispersion causes the pulse to spread out in time with travelled distance.

To show the analogy between narrow-band dispersion and diffraction we start with eliminating most terms from the NLS equation. First of all we assume a medium in which no nonlinearities are present, so all terms containing the nonlinear parameter  $\gamma$  stop playing a role. This assumption originates from the fact that the nonlinear parameter of most materials is very small and the assumption is valid when we avoid using pulses with very high peak powers or materials with a high nonlinear parameter. Secondly we assume a lossless medium. The loss will just scale our solution and is in that sense not very fundamental. For the last assumption we use the narrow-band property of the pulse. Because the pulse is narrow-band ( $\frac{\Delta\omega}{\omega_0} \ll 1$ ) we can neglect the effects caused by third order dispersion (TOD)  $\beta_3$  and fourth order dispersion (FOD)  $\beta_4$ , because second order dispersion dominates strongly. There is one exception though: if the carrier wavelength is close to the zero-dispersion wavelength,  $\beta_2$  and  $\beta_3$  dispersion become comparable, and TOD must then be included.

Bearing the change of sign in mind (because we use the opposite convention), we end up with the parabolic equation:

$$\frac{\partial A(z, \tau)}{\partial z} = \frac{i}{2} \beta_2 \frac{\partial^2 A(z, \tau)}{\partial \tau^2} \quad (2.5)$$

A quick comparison confirms the parabolic form of the equations:

Paraxial diffraction

$$\frac{\partial E}{\partial z} = -\frac{i}{2k} \nabla_t^2 E$$

Narrowband dispersion

$$\frac{\partial A}{\partial z} = \frac{i}{2} \beta_2 \frac{\partial^2 A}{\partial \tau^2}$$

The equation for narrowband dispersion is easily solved in the spectral domain. The baseband ( $\Omega$ ) spectrum of the pulse envelope  $A(z, \Omega) = F(A(z, \tau))$  is described independently of the carrier frequency, yielding [10]:

$$A(z, \Omega) = A(0, \Omega) \exp\left(\frac{-i z \beta_2 \Omega^2}{2}\right). \quad (2.6)$$

As the spectrum of the pulse is the baseband spectrum  $A(z, \Omega)$  of the envelope centered around the carrier  $\omega_0$ :  $E(z, \omega) = A(z, \Omega) \exp(-i \beta_0 z)$ , the total solution is known.

## 2.3 Time-lens concept

After our elaboration on the origin and concept of time-space duality we come to a point where we explain how it can be used. The researcher Brian H. Kolner was the first to realize that a complete temporal analog of an imaging system could be made based on the duality as long as a temporal-analog of a normal thin lens was found [B.H. Kolner, IEEE J. Quant. Electron. 30, 1951-1963 (1994)[7]]. He was thus the founding father of the theory of temporal imaging. With this so-called 'time-lens' we could then either built a magnifier which allows for stretching of signals in the time domain or use the temporal analog of Fraunhofer diffraction and create a Fourier transform. Hence we can retrieve the spectrum of a signal. Figure 2.4 shows these two operation regimes.

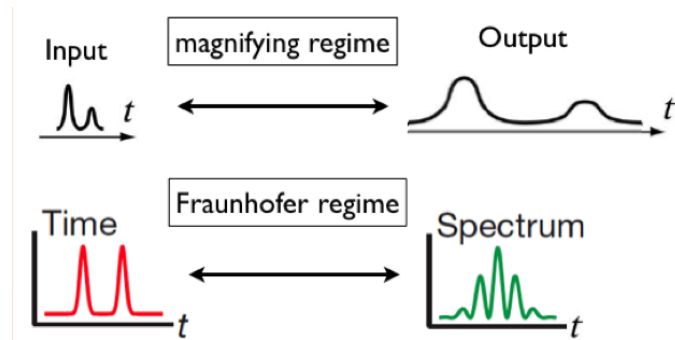


**Figure 2.4:** Magnifying and Fraunhofer regime of a temporal imaging system.

To understand what constitutes a temporal analog of a thin lens, we first explain and derive what the action of a thin lens in the spatial domain is and then look for an equivalent time-lens which acts on the time domain.

### 2.3.1 Thin lens action

Essentially a thin lens acts as a phase transformer. Because the lens has a different refractive index  $n$  than the surrounding air ( $n_{air} = 1$ ), the resulting phase shift of the light following transit depends on the time spent in the lens. We consider a thin lens so that a light ray propagating in the  $z$ -direction which enters the lens at a transverse position  $(x,y)$ , leaves the lens at the same transverse position. The resulting phase shift for each transverse position is dependent on the focal distance  $f$  of the lens and varies quadratically in the (spatial) parameters  $x$  and  $y$  [11]:

$$t(x, y) = e^{-ikn\Delta_0} e^{\frac{ik}{2f}(x^2+y^2)} \quad (2.7)$$

A derivation of this equation can be found in the appendix A.1. The first exponential is a (negligible) constant factor depending on the maximal thickness  $\Delta_0$  of the lens and the second exponential contains the fundamental lens-operation. The lens quadratically modulates the phase of the incoming field in the real space. In doing so for example the outgoing wavefront of an incoming plane wave will spherically diverge or converge depending on the sign of the focal distance  $f$  as shown in figure 2.5.

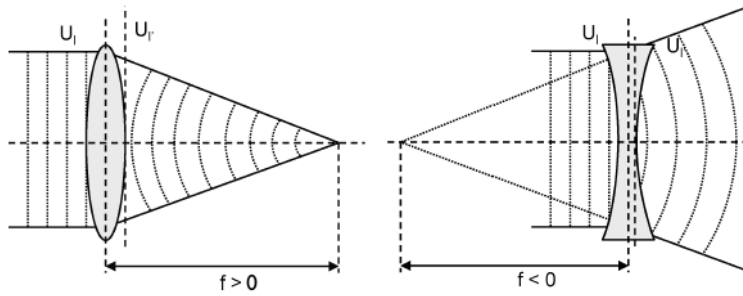


**Figure 2.5:** The action of a thin lens depends on the sign of the focal distance [11].

### 2.3.2 Time-lens action

From the above equation 2.7, the lens-operation can be described by the phase modulation  $e^{\frac{ik}{2f}(x^2+y^2)}$ . It is now time to look for a similar factor describing the time-lens action. We look for a quadratic phase modulation of the incoming field in time. We must be clear though: the time-parameter we consider is the traveling-wave coordinate  $\tau$  as defined by (2.4). Additionally this quadratic phase modulation is equivalent to a linear chirp in the spectrum of a pulse. In accordance with reference [7] we propose:

$$H(\tau) = e^{\frac{i\omega_0}{2f_T}\tau^2} = e^{i\phi(\tau)} \quad (2.8)$$

in which  $f_T$  is the focal time and  $\omega_0$  is the optical carrier frequency of the outgoing wave. Therefore any configuration that imparts a quadratic phase modulation in time to a pulse is

suited to play the role of time-lens. This can be achieved by using an electro-optic modulator or by all-optical mixing whereby an optical pump imposes its quadratic phase to the signal via a nonlinear process. In the following sections a description is given for the characteristic parameters of the time-lens. Just as a normal lens has a specific focal distance, numerical aperture and f-number, a time-lens has a focal time, temporal aperture and f-number.

### 2.3.3 Focal time

The focal time  $f_T$  is a measure of the chirp rate imposed by the lens. The chirp rate  $K$  is the time-derivative of the instantaneous frequency  $\omega_i$ :  $K = d\omega_i/d\tau$ . The instantaneous frequency  $\omega_i$  is defined by:

$$\omega_i = \omega_0 + \frac{d\phi}{d\tau} \quad (2.9)$$

To show the dependence of  $f_T$  on  $K$ , we write down a Taylor series for a general phase function around  $\tau = \tau_0$ :

$$\phi(\tau) = \phi_0(\tau) + (\tau - \tau_0) \frac{d\phi}{d\tau} + \frac{(\tau - \tau_0)^2}{2!} \frac{d^2\phi}{d\tau^2} + \dots \quad (2.10)$$

After putting  $\tau_0 = 0$  (which is possible because we can choose our time origin) and comparing equation (2.10) with equation (2.8), we can identify:

$$\frac{d^2\phi}{d\tau^2} = \frac{\omega_0}{f_T} \quad (2.11)$$

We can thus relate the focal time with the chirp rate via:

$$f_T = \frac{\omega_0}{d\omega_i/d\tau} = \frac{\omega_0}{K} \quad (2.12)$$

We can interpret this result easily. It states that when the chirp rate is high we have a short focal time and thus strong lens action and vice versa. Closely related to the focal time is the focal length  $\xi_f$ . This focal length is "the propagation distance to remove the phase modulation of the lens" [10]. The focal length combined with the  $\beta_2$  dispersion parameter of the specific medium in which the pulse travels gives the focal group delay dispersion (focal GDD) which is related to the chirp of the lens:

$$D_f = \xi_f \cdot \beta_2 = -\frac{1}{d\omega_i/d\tau} = -\frac{1}{K} \quad (2.13)$$

### 2.3.4 Temporal aperture:

The numerical aperture of a lens defines the region where the parabolic phase is applied to the incoming field. Analogously the time aperture defines a time-window through which the parabolic phase is applied. If the incoming pulse is longer than the aperture time, only a part

of the pulse will undergo lens action. If the rest of the pulse doesn't see a quadratic phase modulation, this results in limited resolution and aberrations. Figure 2.6 illustrates this:

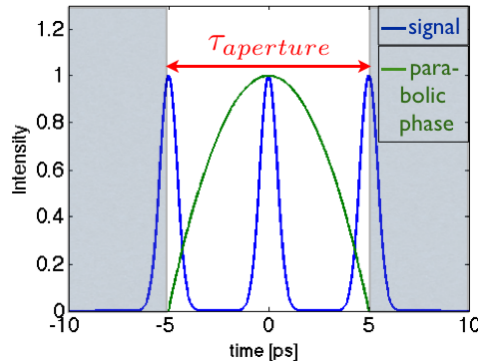


**Figure 2.6:** The time aperture defines the time-window through which the parabolic phase is applied.

### 2.3.5 f-number

For a thin lens the definition is  $f^\# = f/D$  in which  $D$  is the lens diameter and  $f$  is the focal distance. A low  $f$ -number corresponds to high resolution. Interesting insight concerning resolution is gained when we consider another form for the  $f$ -number [12]:

$$f^\# = \frac{k_0}{\Delta k}. \quad (2.14)$$

The above expression means that the  $f$ -number is inversely proportional to the (spatial frequency) bandwidth introduced by the thin lens. Now we turn to the temporal case. We define a temporal aperture  $\Delta\tau$  and use the following definition for the  $f$ -number, completely analogous to  $f^\# = f/D$

$$f_T^\# = \frac{f_T}{\Delta\tau}. \quad (2.15)$$

Similar to the above expression 2.14 one then obtains for the time-lens that [12]:

$$f_T^\# = \frac{\omega_0}{\Delta\omega} \quad (2.16)$$

This is an important relation and we will get back to it in a later paragraph about resolution 2.5.1. Essentially it means that the thin lens imparts a (temporal) frequency bandwidth to the incoming pulse and the broader the imparted bandwidth, the better the resolution.

## 2.4 Imaging systems

Now that we have derived the time-domain analogs to diffraction and lenses, we are able to build the time-domain analog of imaging systems as we know them. The classical imaging

system consists of diffraction through air followed by a lens after which again diffraction occurs. The temporal setup will look like this: dispersive element – time-lens – dispersive element. An imaging system can work in two regimes. Either the imaging condition is fulfilled and magnification (stretch) of the incoming pulse results, or we get the Fourier transform regime in which the output pulse is the Fourier transform of the incoming pulse. In this section we go into detail of the imaging condition and how the Fourier transform can be established.

	time	frequency	
input dispersion	$G1(z, \tau) = \frac{1}{\sqrt{4\pi ia}} \cdot e^{i\frac{\tau^2}{4a}}$	$G1(z, \Omega) = e^{-ia\Omega^2}$	$a = \frac{z}{2}\beta_{21}$
output dispersion	$G2(z, \tau) = \frac{1}{\sqrt{4\pi ib}} \cdot e^{i\frac{\tau^2}{4b}}$	$G2(z, \Omega) = e^{-ib\Omega^2}$	$b = \frac{z}{2}\beta_{22}$
time-lens	$H(\tau) = e^{i\frac{\tau^2}{4c}}$	$H(\Omega) = \sqrt{4\pi ic} \cdot e^{-ic\Omega^2}$	$c = \frac{f_T}{2\omega_0}$

**Figure 2.7:** Transfer-functions for dispersion and time-lens action in the time and frequency domain.

The way to tackle this problem is to work with the transfer-functions for the different parts of the imaging system. The time and frequency domain functions corresponding to dispersion and time-lens action are given in the figure 2.7 [7]. The parameter  $\Omega$  is the base-band frequency,  $\beta_{21}$  and  $\beta_{22}$  are the second-order dispersion parameters of the first and second dispersive element respectively.

### 2.4.1 Magnification regime

The setup for a temporal imaging system working in the magnification regime is the following:

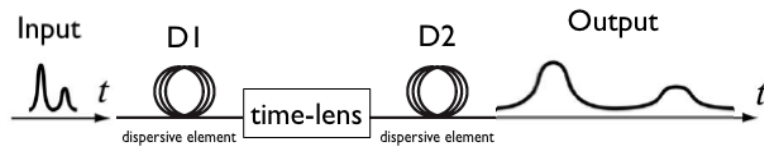


**Figure 2.8:** Set-up temporal imaging system working as a magnifier.

As mathematically shown in the appendix A.3, the basic result of the magnification regime

is:

$$A(L_2, \tau) = \frac{1}{2\pi\sqrt{M}} e^{i\frac{\omega_0 \tau^2}{2M f_T}} A(0, \tau/M) \quad (2.17)$$

This equation states that, except from a phase factor, the output signal is a scaled replica of the input signal. The main step in the derivation of equation 2.17 leads to the temporal imaging condition:

$$\frac{1}{D1} + \frac{1}{D2} = -\frac{\omega_0}{f_T} \quad (2.18)$$

The parameters D1 and D2 represent the total dispersion which the signal sees after passing through the first and second dispersive element respectively. This expression is completely similar to the well-known thin lens-law (with  $d_i$  the image distance and  $d_o$  the object distance):

$$\frac{1}{d_o} + \frac{1}{d_i} = \frac{1}{f} \quad (2.19)$$

The magnification factor M is

$$M = -\frac{D2}{D1}. \quad (2.20)$$

Again the similarity to the spatial case  $M = -d_i/d_o$  is striking. Using a temporal imaging system working in the magnification regime allows us to stretch a signal in time and as such we can measure it using existing oscilloscopes with a much higher resolution. Magnifications as high as  $M = 600$  are reported [13], illustrating the great success of this regime.

After showing the magnification regime we proceed to the Fourier transform regime, which will be the focus of the rest of this thesis.

## 2.4.2 Fourier transform regime

The diffraction phenomenon has an interesting property in that it can enable a spatial Fourier transform. When an input field with finite transverse dimensions diffracts during a long travel period, the far field appears to be the spatial Fourier transform of the original field. This is called Fraunhofer diffraction. When the input field first passes through a thin lens and then diffracts, the lens results in the far field being 'brought closer', more exactly it is brought to the focal plane of the lens, so that the wave doesn't have to diffract over a very long distance before it becomes its spatial Fourier transform. In the spirit of space-time duality we know that a similar temporal regime must exist via dispersion whereby the incoming pulse evolves to its spectrum, so that a (temporal) Fourier transform is performed. This is shown in figure 2.9. Analogous to the spatial case, the dispersion has to be very large before the Fourier transform is established so a time-lens is used to bring the Fourier transform closer.

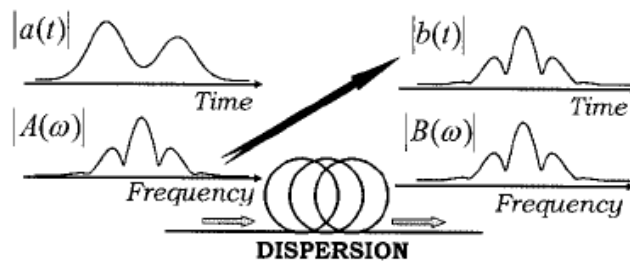


**Figure 2.9:** Fourier transform regime [14].

There are two reciprocal ways to use the Fourier transform property. Either we send a pulse through a time-lens followed by a dispersive element and measure the time-domain distribution of the pulse in the back focal plane of the lens in which we obtain the spectrum of the incoming pulse. Or we send the pulse through a dispersive element followed by the time-lens and measure the spectrum domain distribution of the pulse in the back-focal plane of the lens and obtain the time-intensity shape of the pulse. Both regimes are shown in figure 2.10. The former is called the frequency-to-time regime and the latter regime will be exploited in the experiments of this thesis work and is called the time-to-frequency regime.

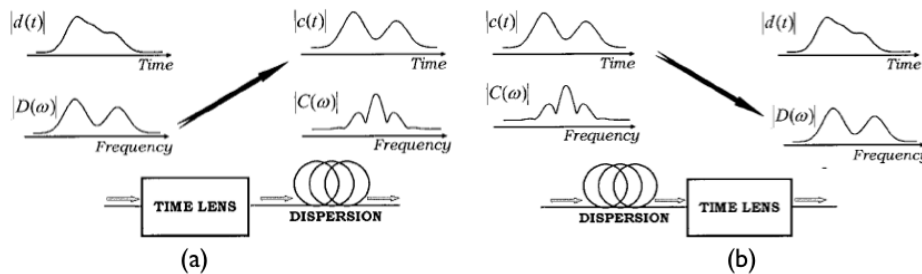


**Figure 2.10:** **a.** Frequency-to-time regime and **b.** Time-to-frequency regime [14].

Like the magnification regime it offers a way to use existing instruments to offer a much higher resolution. In this case an optical spectrum analyzer (OSA) will be used to show the time-domain intensity shape of the pulse under test.

An extensive mathematical derivation is now done for the case whereby the parametric process of four-wave-mixing (FWM) acts as a time-lens. This derivation is needed to explain the origin of two important relations, namely the Fourier transform condition and the time-to-frequency conversion factor, which determine the performance of a time-lens based Fourier transform system. These relations will be used intensively in the design and optimisation chapter of this



thesis. In order to understand the time-lens action in the following derivation we also explain the FWM process.

### Mathematical derivation of a time-lens implemented via four-wave-mixing:

The setup is similar to the temporal magnifying imaging system. An input dispersion is followed by a time-lens, then the signal passes through the output dispersion. An OSA then measures the spectrum of the output signal. The OSA measurement gives no phase-information of the spectrum. Therefore the second dispersion isn't really needed for our purpose because it will only change the phase of the spectrum, leaving the OSA result unaffected. The setup is schematically shown in figure 2.11.

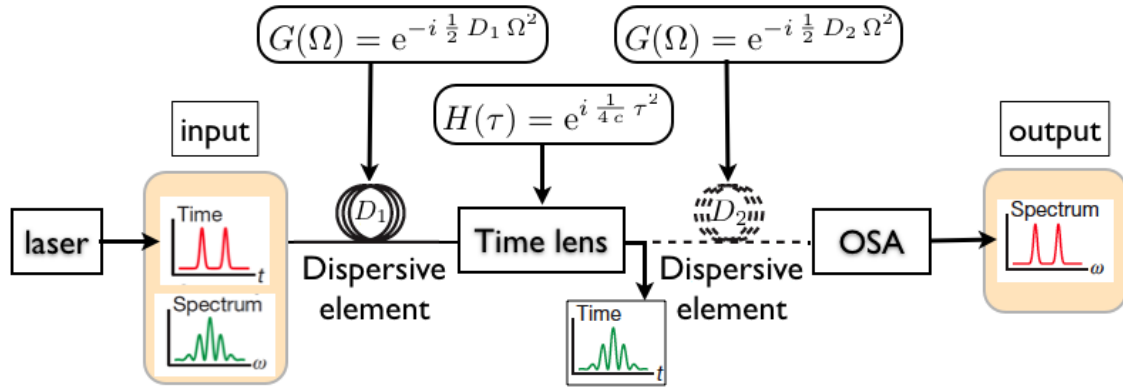


**Figure 2.11:** Setup temporal imaging system working as a time-to-frequency converter.

We now start the mathematical derivation:

#### First dispersion step:

The signal propagates through a dispersive element and its evolution can be described by the transfer function for second order dispersion:  $G(\omega) = e^{-ia\Omega^2}$  in which  $a = \frac{1}{2} L_1 \beta_2 = \frac{1}{2} D_1$ .

We can thus calculate the spectrum after the first dispersive element:

$$A(L_1, \Omega) = A(0, \Omega) e^{-1/2 i D_1 \Omega^2}. \quad (2.21)$$

Remember that this is the solution of the parabolic equation for narrow-band dispersion 2.2.2.

We now take the conjugate of the above formula and do the transformation  $\Omega \mapsto -\Omega$

$$\bar{A}(L_1, -\Omega) = \bar{A}(0, -\Omega) e^{1/2 i D_1 \Omega^2}. \quad (2.22)$$

This expression 2.22 will be used in later steps.

### Lens action:

After the dispersive element the signal travels through the time-lens. The transfer function for time-lens action is  $H(\tau) = e^{\frac{1/4i\tau^2}{c}}$  in which  $c = 1/2 \frac{f_t}{\omega_0}$ . This means that the pulse envelope  $A_l$  after the lens can be written as:

$$A_l(z + \epsilon, \tau) = A(z, \tau) H(\tau). \quad (2.23)$$

Because the time-lens action is obtained via FWM, the transfer function  $H(\tau)$  operates on the conjugate  $\bar{A}$  of the pulse  $A(z, \tau)$  just before the time-lens. So we have to adjust equation 2.23 to:

$$A_l(z + \epsilon, \tau) = \bar{A}(z, \tau) H(\tau). \quad (2.24)$$

To make this clear we briefly discuss the FWM process:

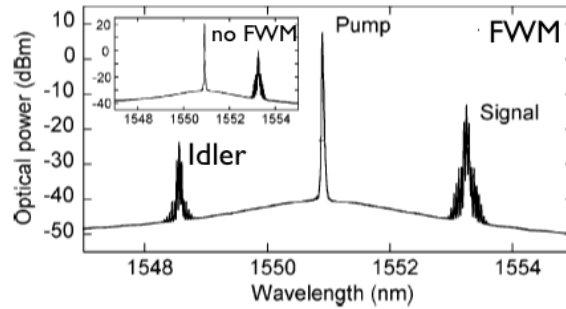


**Figure 2.12:** An idler is generated during FWM of the pump and signal pulse[15].

In general, parametric processes can easily be understood in quantum mechanical terms when we consider that the pump and signal photons interact according to the law of energy and impulse conservation. For four-wave-mixing two pump photons interact with one signal photon, creating an idler photon. The law of energy states that  $2 \cdot \hbar\omega_p - \hbar\omega_s = \hbar\omega_i$ . The result is that the idler is at frequency  $\omega_i = 2 \cdot \omega_p - \omega_s$ . The law of conservation of impulse demands:  $2 \cdot k_p - k_s = k_i$  or  $\Delta k = 2 \cdot k_p - k_s - k_i = 0$  which is basically a phase matching condition. We now turn to the classical electro-magnetic point of view (nonlinear Schrödinger equation) and write down the equation for the evolution of the idler in the FWM process [16]:

$$\frac{dA_i}{dz} = -i\gamma \left\{ A_i P_i + 2 A_i (P_p + P_s) + A_p^2 \bar{A}_s e^{i\Delta k z} \right\} \quad (2.25)$$

The origin of this equation lies in the NLS equation. The index i stands for idler, p for pump and s for signal. The function  $A = A(z, \tau)$  is the slowly varying envelope of the electric field and  $P_n$  is the power of the waves such that  $P_n = |A_n|^2$ . Also the coefficient of nonlinearity  $\gamma$  is

present in this equation and implies that a highly nonlinear material is needed for (efficient) FWM. When there is phase matching between the three waves  $\Delta k \approx 0$ . If this condition is not obeyed the idler growth is insufficient. The pump gives energy to the signal which gets amplified and part of the pump's energy goes to the idler generation. In figure 2.12 the generated idler is shown.

According to equation 2.25 the idler growth is proportional to the complex conjugate of the signal times the square of the pump envelope. We assume the ideal case where the pump has a constant amplitude and a quadratic phase and this way we can identify:  $A_p^2 = H(\tau)$ . **The pump wave has ideally no influence other than to impose its quadratic phase.** Hence we have shown that the transfer function operates on the conjugate of the signal in the case of FWM.

Other parametric processes like second harmonic generation (SHG) work on the signal itself [10]. The basic result stays the same though. We can still relate the spectrum of the idler with the intensity of the incoming pulse, the Fourier transform condition to achieve this just gets a change in sign. Concerning the conjugate operation, the following property of the Fourier transform comes to hand:  $a(t) = \bar{g}(t) \mapsto A(\omega) = \bar{G}(-\omega)$ .

We now proceed with the calculation. Multiplication in the time domain gives a convolution in the spectral domain, so to calculate the spectrum after the lens we take the convolution of the spectrum of  $\bar{A}(z, \tau)$  before the lens with  $H(\Omega)$ . The Fourier transform of the transfer function  $H(\tau)$  is

$$H(\Omega) = \sqrt{4\pi i c} e^{-ic\Omega^2}. \quad (2.26)$$

Writing down the convolution operation gives

$$A_l(z + \epsilon, \Omega) = \sqrt{4\pi i c} \int_{-\infty}^{\infty} \bar{A}(L_1, -\Omega') e^{-ic(\Omega - \Omega')^2} d\Omega'. \quad (2.27)$$

With the use of equation 2.22 and the expansion of the exponential we get:

$$A_l(z + \epsilon, \Omega) = \sqrt{4\pi i c} e^{-ic\Omega^2} \int_{-\infty}^{\infty} \bar{A}(0, -\Omega') e^{1/2 i D_1 \Omega'^2} e^{-ic\Omega'^2} e^{i 2c\Omega\Omega'} d\Omega'. \quad (2.28)$$

It is now clear that if the two factors in  $\Omega'^2$  cancel out we get the inverse Fourier transform of the initial spectrum when we identify the time parameter  $\tau = 2c\Omega$ . This gives the condition:

$$D_1 = 2c \quad (2.29)$$

We can easily interpret this condition: the input dispersion should be compensated for by the phase-modulation imparted by the time-lens. As a result after the time-lens we get:

$$\boxed{A_l(z + \epsilon, \Omega) = \sqrt{2\pi D_1} e^{i\pi/4} e^{-ic\Omega^2} \bar{A}(0, \tau)} \quad (2.30)$$

This is the basic result of time-to-frequency conversion. The spectrum after the lens is proportional to the input pulse apart from a phase factor.

### Second dispersion step:

The idler field after the lens is  $E_i(z, \omega) = A_l(z + \epsilon, \Omega) e^{-i\beta_0 z}$  and we have now two choices: either we send the signal after the lens directly to an optical spectrum analyzer (OSA) which measures

$$|E_i(z, \omega)|^2 = 2\pi D_1 |A(0, \tau)|^2, \quad (2.31)$$

or we can first send the signal  $A_l$  through a second dispersive element with transfer function  $G(\Omega) = e^{-1/2iD_2\Omega^2}$  with  $D_2 = L_2\beta_2$  to cancel the phase factor  $e^{-ic\Omega^2}$ ,

$$A_{out}(z, \Omega) = \sqrt{2\pi D_1} e^{i\pi/4} e^{-ic\Omega^2} e^{-1/2iD_2\Omega^2} \bar{A}(0, \tau), \quad (2.32)$$

which reduces to

$$A_{out}(z, \Omega) = \sqrt{2\pi D_1} e^{i\pi/4} A(0, \tau) \quad (2.33)$$

for

$$D_2 = -2c = -D_1. \quad (2.34)$$

Sending the signal  $A_{out}$  to an OSA results in the same formula as (2.31). This makes clear why the second dispersion step is not needed in the time-to-frequency setup.

### Discussion of the time-to-frequency regime:

Having done the analytical derivation it is important to understand the consequences of the taken steps. We go into detail of the two obtained relations  $D_1 = 2c$  and  $t = 2c\Omega$ , which are the above mentioned relations which determine the performance of the setup.

According to the basic relation  $D_1 = 2c$ , **the main condition to end up in the Fourier regime is that the obtained chirp of the pulse following propagation through the input dispersive element is cancelled in the time-lens.** This relates the lens-parameters with the dispersion parameters via  $D = \beta_2 L = 2c = \frac{f_r}{\omega_0} = \frac{1}{K}$ . The equation

$$\boxed{D = \frac{1}{K}} \quad (2.35)$$

is called the **Fourier transform condition.**

We can also state this relation in terms of the focal GDD from section 2.3.3:  $D = -D_f$ . Therefore the dispersion the signal pulse goes through, must be the opposite of the focal

GDD. This is similar to spatial Fourier imaging condition whereby the paraxial wave has to travel the focal distance, after passing through the lens, before we get the Fourier transform. The minus sign arises because the time-lens acts on the conjugate of the signal if the lens action is established via four-wave-mixing.

The second important derived relation  $\tau = 2c\Omega$  defines the **time-to-frequency conversion factor**. The time-to-frequency conversion factor is crucial to calculating the duration of the pulse via the spectrum analyzer readings. The conversion factor is stated below in terms of the system parameters ( $\Delta\omega = \Delta\Omega$ ):

$$\tau = \beta_2 L (\omega - \omega_0) \quad (2.36)$$

Rewriting this equation in terms of the spectral bandwidth of the idler in wavelengths gives:

$$\tau = \left(\frac{\lambda_s}{\lambda_i}\right)^2 D L \Delta\lambda_i \quad (2.37)$$

or we can put it in function of the lens-parameters:

$$\tau = \frac{(\omega - \omega_0) f_T}{\omega_0}. \quad (2.38)$$

The possibilities of the Fourier transform regime are numerous, ranging from signal regeneration [17] to the above explained signal measurements [1] and to distortion-free transmission [18] etc.

## 2.5 Performance of temporal imaging systems

### 2.5.1 Resolution

This section contains a more intuitive reasoning about resolution as the exact derivation would take us too long. The exact way to derive the resolution of an imaging system is by considering the impulse response of the system and applying a criterion/definition for resolution, e.g. Rayleigh criterion [19]. In the appendix A.2 the interested reader can find the derivation of the impulse response.

For our reasoning we first have to introduce some insights from Fourier optics. In Fourier optics, proof is offered for the fact that a field can be decomposed as a linear superposition of plane waves. Every plane wave has its own direction which is determined by its spatial frequency. If we have a field propagating along the z-axis, then for every plane wave, its spatial frequency determines the angle between the k-vector of the plane wave and the z-axis. The higher the spatial frequency, the steeper the angle. A paraxial wave has a narrow-band of spatial frequencies, implying that it is composed of waves which all have a direction close

to the z-axis, leading to a field which is confined along the z-axis. A lens basically changes the spatial frequency of every plane wave which is captured by its aperture. In doing so it redirects these plane waves and the stronger the lens, the bigger the change in spatial frequency it can impose. The fine details about this Fourier decomposition and spatial frequency theory can be found in [19].

We now state the easy rule of thumb about (temporal and spatial) resolution: the smaller the f-number the better the resolution. To show this, we turn to the spatial frequency point of view. We can see that the larger the aperture of the lens is, the broader the range of spatial frequencies is that will be captured by the lens and redirected by it. Hence at the image plane more information is available to reconstruct the image because more spatial frequencies are present. This leads to better resolution for larger aperture lenses. Equivalently we can state that the larger the spatial bandwidth of the lens is, the higher the resolution. Equation 2.14 for the (spatial) f-number supports the above explanation.

For a time-lens same reasoning holds and when the time-lens imposes a large (spectral) bandwidth to the incoming pulse, high resolution results. This is also clear in the expression of the f-number 2.16 which we repeat here:

$$f_T^\# = \frac{\omega_0}{\Delta\omega}.$$

The interpretation we should give to the temporal resolution of a temporal imaging system is the following: if the resolution is determined to be  $\tau_{res}$  then the output of the system for every pulse with an initial width  $\tau_s < \tau_{res}$ , will be the same as for a pulse with an initial width  $\tau_s = \tau_{res}$ .

## 2.5.2 Aberrations

The key to high performance imaging systems is to have pure second-order dispersive elements combined with a time-lens which induces a pure parabolic phase. If this condition is not satisfied the combination dispersion-time-lens will not create an exact Fourier transform. In the article “aberrations in temporal imaging” [20] an extensive framework is given to understand the effects of higher-order dispersion and phase modulation. We won’t go into detail but give a flavour of the (visual) power of their approach. They invoke the concept of time rays on which aberrations have a distinct effect. Each ray represents a spectral component  $\Omega$  and their slope in a space-time diagram depends on this baseband frequency  $\Omega$  and the dispersion parameters of the medium in which the pulse travels. If the medium only exhibits second-order dispersion the slope is simply  $\Omega$ . On the other hand if higher-dispersion effects play a role, the slope  $S$  is

$$S = \Omega \left[ 1 + \frac{\Omega}{2!} \frac{\beta_3}{\beta_2} + \dots + \frac{\Omega^{n-2}}{(n-1)!} \frac{\beta(n)}{\beta_2} \right].$$

So we have a slope which depends on the relative values of  $\beta_i/\beta_2$  with  $i > 2$ . In a space-time diagram in figure 2.13 we can now see how deviation from the ideal  $\Omega$  slope gives aberrations:

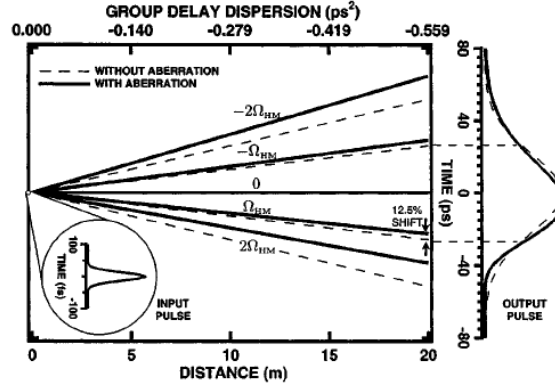


**Figure 2.13:** Space-time diagram showing aberrations due to higher order dispersion [20].

As for a time-lens which induces higher order phase modulation, the aberrations arise from the fact that the focal GDD becomes time-dependent. This is because the imparted frequency chirp becomes time-dependent. All portions of the pulse experience a slightly different chirp rate which results in aberrations because the imaging condition or Fourier transform condition can no longer be obeyed for the total pulse.

## 2.6 Conclusion

In this chapter we studied the theory of temporal imaging. To understand temporal imaging one should constantly draw analogies between a classical thin lens imaging system and a temporal imaging system. The key building blocks in a temporal imaging set-up are dispersive elements and a time-lens. The dispersive elements take over the role of diffraction through air and the time-lens is analogous to the thin lens. Essentially a dispersive element imparts a quadratic phase modulation on the base-band frequency parameter and a time-lens imparts a quadratic phase modulation on the time-parameter. A temporal imaging system can work in two important regimes. The first regime is the magnifying regime whereby the signal is stretched out in time. The second regime is the Fraunhofer regime whereby the signal is Fourier transformed, so that the output pulse yields the spectrum. **The focus of this thesis work is on the time-to-frequency Fraunhofer regime.** We retrieve the temporal waveshape of the input signal via the spectrum of the output signal which is measured with an OSA. Two important equations were derived which characterise an imaging system working in the time-to-frequency Fraunhofer regime. The first is the Fourier transform condition which states when exactly a Fourier transform of the input signal is achieved and the second

---

equation yields the time-to-frequency conversion factor. The next chapter shows how this temporal imaging system can be implemented to measure femtosecond pulses and compares it with other existing pulse measurement techniques.



## Chapter 3

# Literature review

### 3.1 Introduction

In the previous chapter we explained what constitutes a temporal imaging system. In this chapter we show how we can use a temporal imaging system to measure ultrashort pulses. We do this via a survey of three key experiments that perform a Fourier transform on the input signal such that measurement with an OSA yields the temporal shape of the input signal. The third of the key experiments triggered this thesis research hence we pay special attention to the reported problems with the specific set-up. In the context of this thesis work it is important to understand other existing pulse measurement techniques in order to compare the performance of our researched temporal imaging system over the alternatives. Therefore we discuss the most popular techniques to characterise ultrashort pulses.

### 3.2 Time-lens methods and experimental set-ups

To date there has been three different approaches to implementing the time-lens mechanism. In this section we discuss these three key experimental set-ups which operate in the Fourier transform regime. The three concepts include an electro-optic modulator, XPM and FWM with chirped pulses.

#### 3.2.1 Electro-optic modulator as time-lens

The first experiments in temporal imaging used an electro-optic modulator to impart a quadratic phase. It avoids the use of nonlinear phenomena and as such it can produce “*a reliable phase modulation independent of optical power*” [7]. The operation principle is fairly

simple: an electro-optic modulator is used to directly modulate the phase of the signal. An optical wave propagating through an electro-optic crystal driven with a sinusoidal voltage with angular frequency  $\omega_m$  acquires a phase shift:

$$\phi(z, \tau) = \Gamma_0 \cos(\omega_m \tau). \quad (3.1)$$

The factor  $\Gamma_0 = \pi \frac{V}{V_\pi}$  is the peak phase deviation and is defined in terms of the half-wave switching voltage  $V_\pi$ . The half-wave switching voltage<sup>1</sup> is the voltage that must be applied across the electro-optic crystal in order to induce a phase shift of  $\pi$ .

As lens action implies parabolic phase modulation, we need to isolate the quadratic part of the sinusoidal modulation. Those quadratic parts are located under the extrema of the sinusoid. In these regions the phase shift can be written as:

$$\phi(z, \tau) = \Gamma_0 \left[ 1 - \frac{(\omega_m \tau)^2}{2} \right]. \quad (3.2)$$

It is clear that the electro-optic (EO) modulator has a time aperture  $\tau_a$  which defines the time window during which the higher order terms of the series expansion of  $\cos(\omega_m \tau)$  are negligible and the modulation is quadratic so that the phase shift has the form of equation 3.2. If the pulse after the dispersive element, which precedes the time-lens, is longer than this time aperture only the central part undergoes ideal lens action. The outer regions of the pulse have a sinusoidal modulation and introduce aberrations in the system. Figure 3.1 makes this visually clear:

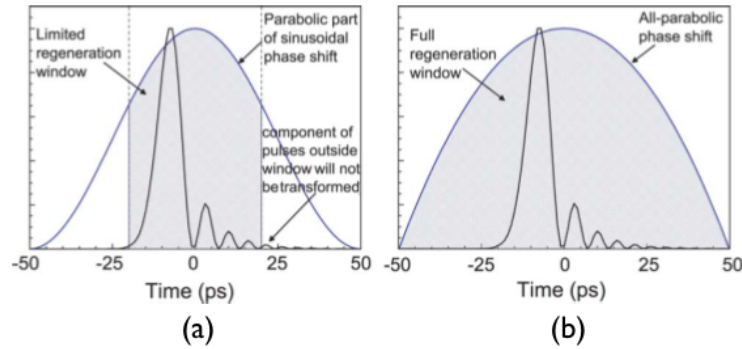


**Figure 3.1:** **a.** Sinusoidal phase modulation **b.** Parabolic phase modulation. [17]

It can be shown [7] that a realistic measure of this time aperture is related to the modulating frequency  $\omega_m$  via:

$$\tau_a \approx \frac{1}{\omega_m}. \quad (3.3)$$

<sup>1</sup>It is generally desirable for the half-wave switching voltage to be less than about 10 volts such that solid state driver amplifiers can be utilized to create the electric field across the single crystal substrate[21].

The chirp rate of the EO modulator time-lens is by definition  $\frac{d\phi^2}{dt^2} = \Gamma_0 \omega_m^2$ , which leads to a focal time of  $f_T = \frac{\omega_0}{\Gamma_0 \omega_m^2}$ . Because we also have an expression for the time aperture from equation 3.3, we know the f-number:

$$f^\# = \frac{f_T}{\tau_a} = \frac{\omega_0}{\Gamma_0 \omega_m}. \quad (3.4)$$

Whereby via identification with equation 2.16 we retrieve the bandwidth imposed by the lens:  $\Delta\omega = \Gamma_0 \omega_m$ . It is immediately clear that if we want a small  $f^\#$  and thus high resolution for a fixed  $\omega_m$ , we have to increase  $\Gamma_0$  which effectively means a large applied voltage so that the applied maximum phase shift increases. This also shows the deficiency of the proposed time-lens. The maximum possible phase shift is  $10\pi$  [1] due to the limit in possible applied voltage and so the modulator frequency  $\omega_m$  has to increase drastically if we wish to improve the resolution.

We now focus on the results of the experiment presented in the article: “Time-to-frequency converter for measuring picosecond optical pulses” [2]. The time-lens is a  $LiNbO_3$  electro-optic phase modulator which has a  $\Gamma_0 = 51$  rad and  $\omega_m = 2\pi \times 5.2$  GHz. We calculate the time-to-frequency conversion factor via formula 2.38 from chapter 2 :

$$\Delta t = \frac{f_T}{\omega_0} \Delta\omega = \frac{1}{\Gamma_0 \omega_m^2} \frac{c 2\pi}{\lambda_0} \Delta\lambda, \quad (3.5)$$

in which  $c$  is the speed of light. The numerical value of the time-to-frequency conversion factor is 30.3 ps/nm. The time aperture is 31 ps and the theoretical resolution ( $= 2.7/(\Gamma_0 \omega_m)$ [22]) is 1.7 ps. The measured pulse width is a spectrum analyzer limited 0.08 nm and as a result the measured resolution is 3 ps ( $\simeq 30.3 \times 0.08$  ps). The set-up and results of this experiment are shown in figure 3.2

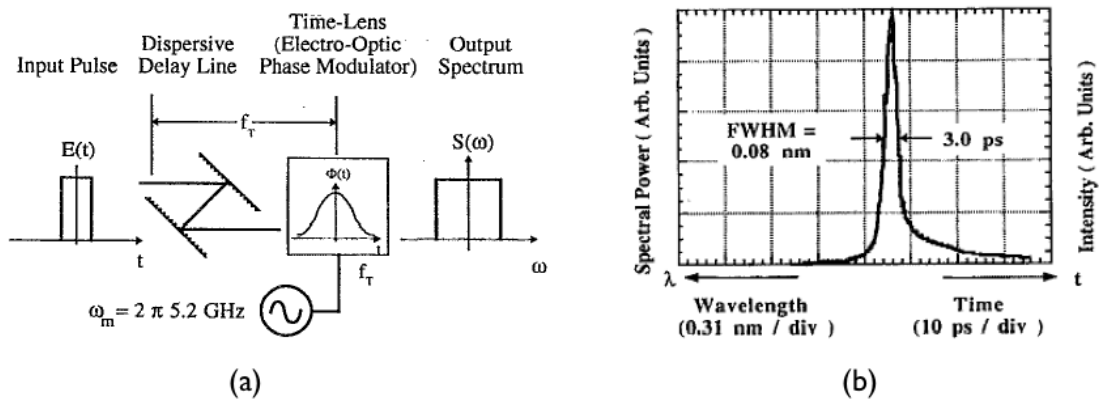


**Figure 3.2:** a. Experimental set-up using a EO modulator as time-lens b. Measurement result showing a resolution of 3 ps [2].

### 3.2.2 XPM with parabolic pulses as time-lens

The second key experiment implementing the time-lens function is described in the paper ‘Linear-distortion compensation using XPM with parabolic pulses’ [23]. The technique used here involves the use of cross-phase modulation (XPM) in a nonlinear fiber. The XPM principle is the following: an intense pump pulse modulates the refractive index  $\tilde{n}$  of a nonlinear material and a copropagating signal wave sees this varying refractive index so its phase is modulated accordingly ( $\phi = \tilde{n} k_0 L$ ). This is a consequence of the optical Kerr effect [9]:

$$\tilde{n}(\omega, |E|^2) = n(\omega) + n_2 |E|^2 \quad (3.6)$$

in which  $|E|^2$  is the optical intensity inside the fiber and  $n_2$  is the nonlinear-index coefficient. In the case of parabolic pulses the change in the index  $\tilde{n}$  is parabolic which imposes a quadratic phase modulation and thus establishes time-lens action. The chirp rate of the time-lens is adjusted by a variation in the power of the parabolic pump pulses. Or as stated in the paper: “*The XPM induces a chirp on the target pulse which is proportional to the gradient of the parabolic pulse intensity profile*”.

The aim of this paper is to remove (time domain) distortions due to second order dispersion from a signal. The set-up works in the frequency-to-time regime whereby the spectrum of the incoming pulse is transferred to the time-domain output pulse. We know from chapter 2 that we then must satisfy the condition that the parabolic phase caused by the lens is compensated for by the following dispersive element:

$$K = -\frac{1}{\beta_2 L}.$$

When the time-lens is preceded by a dispersive element, this doesn’t change its frequency-to-time property as the spectrum before the lens is not altered by dispersion.

When we work with signals which have the same shape in time and frequency domain, such as Gaussian or Sech pulses, we can imagine to completely reconstruct the incoming pulse when we obey a new condition such that the frequency-to-time conversion factor scales the output pulse to have the same FWHM width as the incoming (undistorted) pulse. For a Gaussian pulse  $u(0, t) = A \exp(-\frac{t^2}{T_0^2})$  this reconstruction-condition is derived in [18] and is simply:

$$K = \frac{1}{T_0^2}.$$

The experimental set-up (see figure 3.3) is the following: A parabolic pump pulse of 10 ps at a center wavelength of 1542 nm is generated using pulse shaping in an super-structured fiber Bragg grating (SSFBG) [24]. The signal pulse is 3 ps long at 1556 nm. An optical delay line ensures that the signal and pump pulses temporally overlap before they are sent into 200 m highly nonlinear fiber (HNLF) with zero dispersion wavelength (ZDW) at 1550 nm and

$\gamma = 20 \frac{1}{W km}$ . Highly nonlinear fiber is used because it has a high  $n_2 (\sim \gamma)$  so that a variation in  $|E|^2$  is clearly reflected in the refractive index  $\tilde{n}$ . The quasi-symmetrical position of the signal and pump wavelength towards the ZDW allows minimized walk-off<sup>2</sup> in the HNLF. After propagation in the HNLF the signal is filtered out via a 3 nm bandpass filter centered at 1556 nm and then it is sent through 150 m of SMF which acts as the dispersive element.

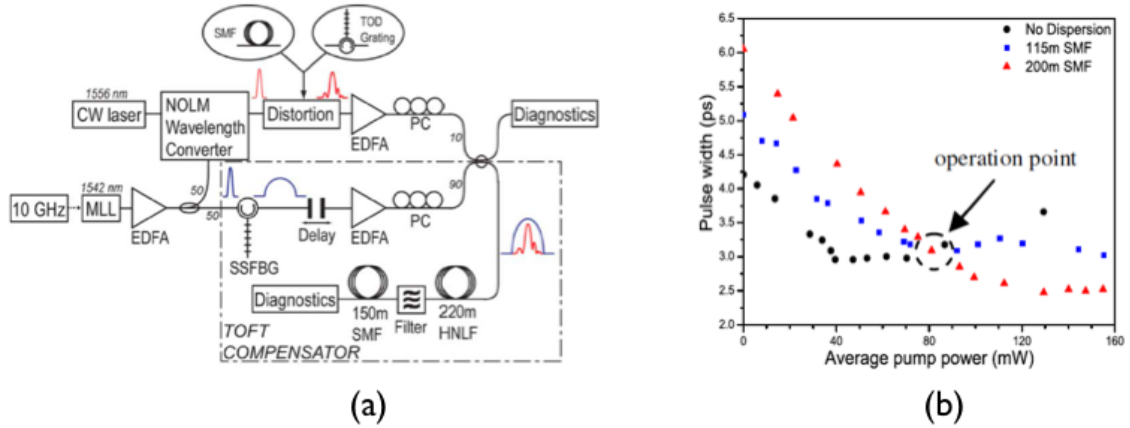


**Figure 3.3:** **a.** Experimental set-up using XPM as the time-lens mechanism **b.** Determination of the operation point for the average pump power so to obey the Fourier transform and reconstruction condition[23].

An important part of the work is to find the correct pump power to achieve the desired chirp rate  $K$  so that both the Fourier transform and reconstruction condition are achieved. This is done by varying the pump power and measuring the output pulse width for various input dispersions. The pump power which offers an output pulse width independent of the preceding input dispersion indicates the correct operation point, which is 90 mW of average pump power for this set-up. This method is displayed in figure 3.3.

The results are presented in figure 3.4 where the output pulse has the same width irrespective of the input dispersion (no dispersion, 100m SMF, 200m SMF) before the time-lens. The distortions due to dispersion of the incoming pulse are indeed completely removed and the authors succeeded in their experiments. The values associated to each pulse profile in the figure refer to the FWHM of the autocorrelation traces rather than the FWHM of the intensity profiles.

<sup>2</sup> Walk-off means that the two pulses experience diminishing temporal overlap with increasing traveled distance because they see a different group velocity in the fiber.

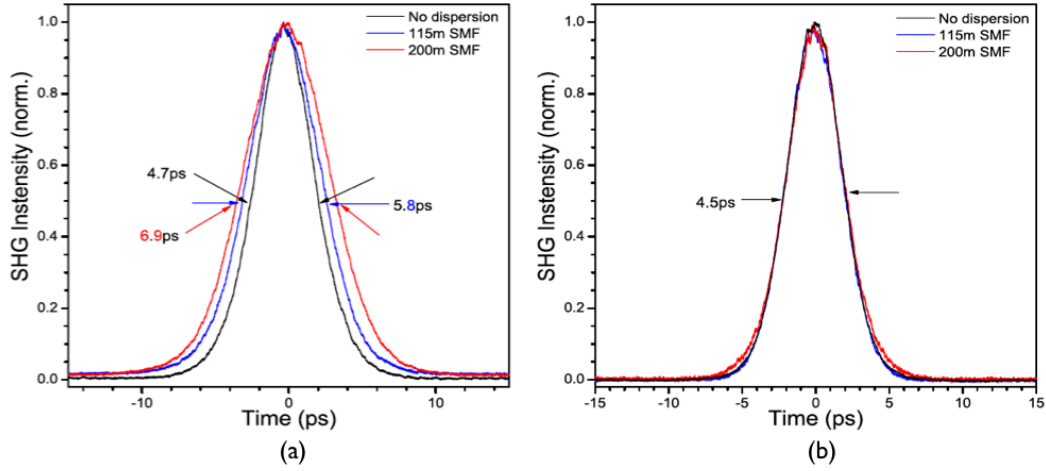


**Figure 3.4:** **a.** Input signal pulse width after varying input dispersion **b.** Signal pulse width after total set-up, showing complete compensation of the distortions caused by the input dispersion[23].

To conclude this section we remark that using XPM as a time-lens is an attractive method and that the pump pulse has the desired parabolic shape as shown in the paper. The main drawback is the practical implications of making a parabolic pulse with different temporal widths. For every width you have to make a new SSFBG. The width of the parabolic pulse is important because it reflects which signal pulses can be transformed. If the signal pulse is broader than the parabolic pump pulse before entering the HNLF, only part undergoes lens action.

### 3.2.3 FWM with chirped pulses as time-lens

The third and final key experiment we discuss is very important as it triggered this research as explained in the introduction. It is a fundamental breakthrough in temporal imaging which allows direct measurement of the intensity of a sub-picosecond signal over a record length of 100 ps combined with a resolution of 220 fs. The paper in which the results are presented is: ‘Silicon-chip-based ultrafast optical oscilloscope’ [1]. It is a follow-up of another important article which demonstrates the time-lens capabilities of four-wave-mixing in a silicon-chip [25]. The set-up works in the time-to-frequency regime whereby the intensity profile of the input is transferred to the spectral domain via the dispersion - time-lens set-up. It is one of the many experiments based on parametric processes as a time-lens. In the parametric process a chirped pump impresses its parabolic phase onto the signal during interaction in a nonlinear medium, hence lens action is obtained. In the set-up four-wave-mixing (FWM) is used because it offers two important advantages over other wave-mixing processes. Firstly FWM is a

process which happens in every material because it originates in the third-order susceptibility  $\chi^3$  which all materials possess<sup>3</sup>. Secondly, the generated idler wavelength is relatively close to the pump and signal wavelength so if wanted we can have all three signals in the same telecommunications-band (S,C or L).

The set-up of the reference paper [1] is shown in figure 3.5.

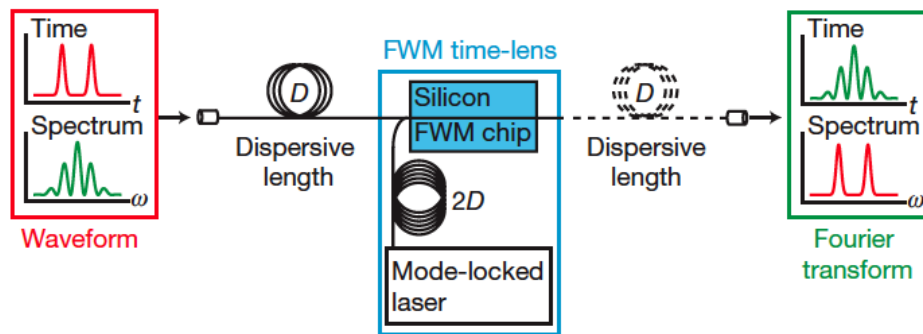


**Figure 3.5:** Silicon-chip-based optical oscilloscope using FWM as the time-lens mechanism[1].

The authors chirped the pump pulse in a simple way so that it could obey the Fourier transform condition 2.35:  $D_s = \beta_{2s} L_s = \frac{1}{K}$  with  $K$  the chirp rate of the time-lens,  $\beta_{2s}$  the group-velocity dispersion (GVD) parameter and  $L_s$  the length of the dispersive fiber through which the signal is sent. In summary: **if you want a FWM time-lens with a focal group delay dispersion (focal GDD) with value  $D$ , then you need a pump pulse which sees twice that dispersion  $D$ .** The evolution of the phase of the pump and signal when  $D_p = 2D_s$  is shown in figure 3.6.

<sup>3</sup>The second-order susceptibility  $\chi^2$  responsible for e.g. sum-frequency-generation vanishes for isotropic materials

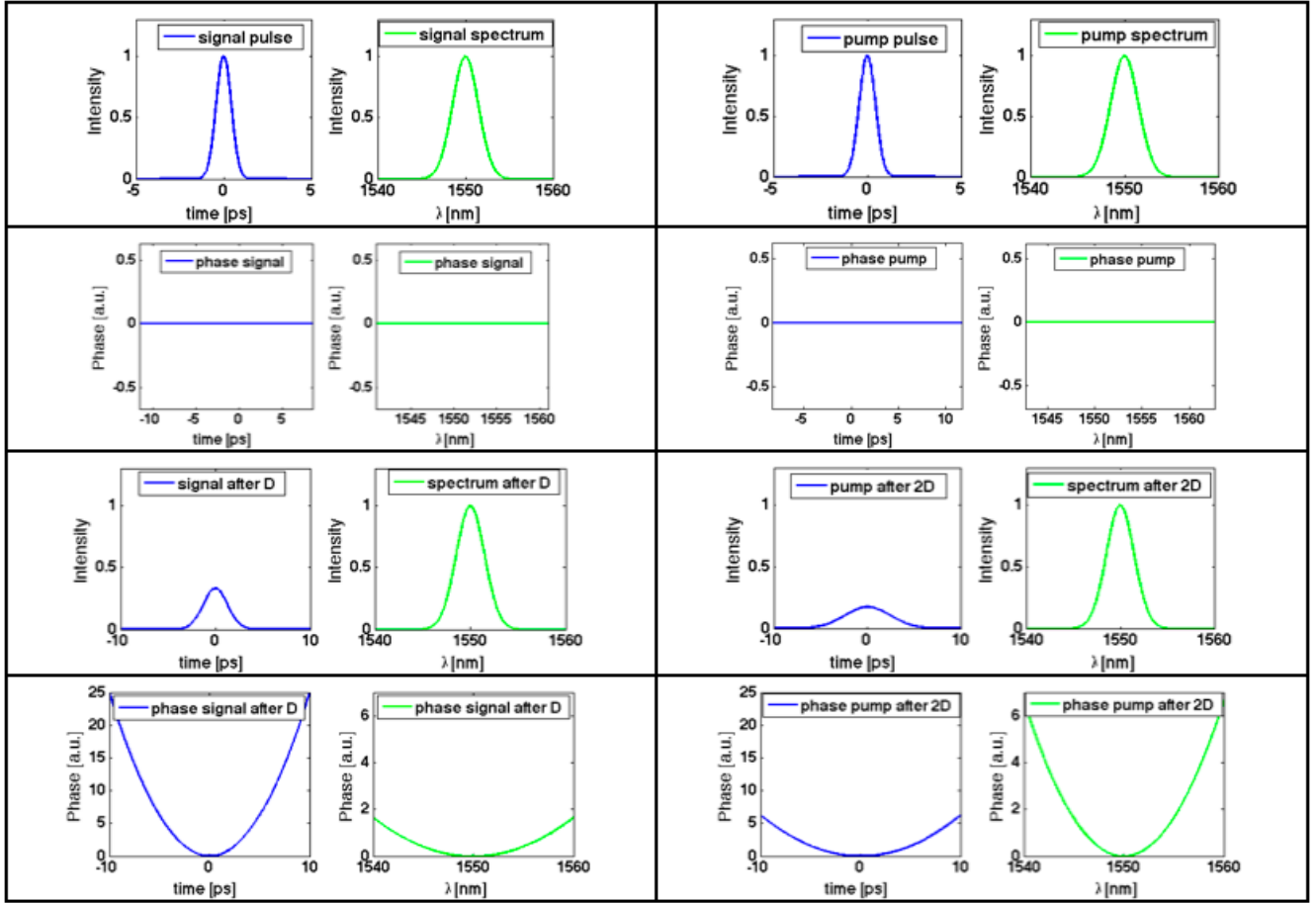


**Figure 3.6:** Evolution of the signal (left column) and pump (right column) in time and frequency domain before (upper 2 rows) and after (lower 2 rows) their respective dispersive elements.

To explain this, we have to remember section 2.4.2, where we derived that the squared envelope function of the pump establishes the lens action. This leads to the requirement that:

$$\exp(i 2 \phi_{pump}) = \exp(i \frac{K}{2} \tau^2) \quad (3.7)$$

in which the right-hand side is the transfer function of a time-lens. If we send the pump through a dispersive fiber with  $\beta_{2p}$  and length  $L_p$  and put  $D_p = \beta_2 L_p$ , the pump wave obtains a phase of the form  $\phi_{pump} = \frac{\tau^2}{2D_p}$ . Via identification with equation 3.7 we obtain:

$$\frac{1}{D_p} = \frac{K}{2} = \frac{1}{2D_s} \quad (3.8)$$

We can thus conclude that to satisfy Fourier transform regime condition, the pump should be subject to twice as much dispersion as the signal. This relation  $D_p = 2D_s$  is clearly indicated in figure 3.5 where the pump pulse from a mode-locked laser passes through a total dispersion



of 2D and the signal undergoes a dispersion of only D.

If we choose the  $\beta_2$  parameter of both dispersive fibers to be the same  $\beta_{2s} = \beta_{2p}$ , this equation implies that the pump pulse should travel through a fiber which has twice the length of the fiber through which the signal passes:  $L_p = 2 L_s$ . The latter choice is used in the experiment. They use the same type of fiber for both the pump and signal but the pump passes through 100 m while the signal passes through 50 m of the fiber.

The time-to-frequency conversion factor is given by 2.36:

$$\Delta\tau = \beta_2 L \Delta\omega.$$

The factor  $\Delta\omega$  is the spectral bandwidth of the idler  $\Delta\omega_i$  which is measured with an optical spectrum analyzer (OSA). When we assume a very narrowband spectrum for the signal it is solely determined by the spectral bandwidth of the pump pulse. This is because for the FWM process the following equation holds:  $\Delta\omega_i = 2 \Delta\omega_p - \Delta\omega_s \approx 2 \Delta\omega_p$  in which we assumed a negligible spectral width of the signal. We can thus rewrite the conversion factor as:

$$\Delta\tau = \beta_2 L \Delta\omega_i \approx 2 \beta_2 L \Delta\omega_p = \Delta\tau_{rec}. \quad (3.9)$$

The last equality shows that this relation also gives the maximum duration of a signal which can be recorded. The reason behind this is that in general a signal has a spectral bandwidth and thus  $\Delta\omega_i$  can only decrease. For the experimental set-up in the article the numerical values give a conversion factor  $\frac{\Delta\tau}{\Delta\lambda} = 5.2 \frac{ps}{nm}$  which implies a very long record length  $\tau_{rec}$  of 150 ps ( $\approx 5.2 \frac{ps}{nm} \times 2 \times 15nm$ ) for a pump bandwidth of 15 nm.

The following important parameter of the temporal imaging system is the obtained resolution. As stated in the article: “*The temporal resolution of the oscilloscope is predicted by considering the transfer of a temporal delta function through the instruments system. This impulse response is precisely the temporal resolution of the instrument.*” [1]. This leads to the following expression for the resolution if all components are perfect:

$$\tau_{resolution} = \frac{\tau_{pump}}{\sqrt{2}} \quad (3.10)$$

where  $\tau_{pump}$  is the initial pump pulse width. This pulse width is inversely proportional to its spectral width  $\Delta\omega_p$  of the pump pulse, so once again we obtain the relation that the resolution is better for a larger bandwidth imposed by the time-lens. The predicted resolution for the set-up is 200 fs for the used 280 fs pump pulse. A small remark though: the relation in equation 3.10 is based on the assumption of an infinite FWM conversion bandwidth which is of course impossible to obtain, so it is merely a guideline rather than an exact expression.

We now turn to the published experimental results. In figure 5.3.1 the record length and

resolution of the system is determined. The record length is retrieved by inserting a (Gaussian) signal pulse with a width of 342 fs and varying its temporal position. As the result shows, the authors could scan the pulse over a record length of 100 ps. To obtain the resolution the following equation is used [1]:

$$\tau_{measured}^2 = \tau_{actual}^2 + \tau_{resolution}^2$$

which for the experiment results in:

$$(407 fs)^2 = (342 fs)^2 + (220 fs)^2$$

so the temporal resolution is determined to be 220 fs. This is very close to the (theoretical) resolution of 200 fs, which is solely limited by the initial pump pulse width.

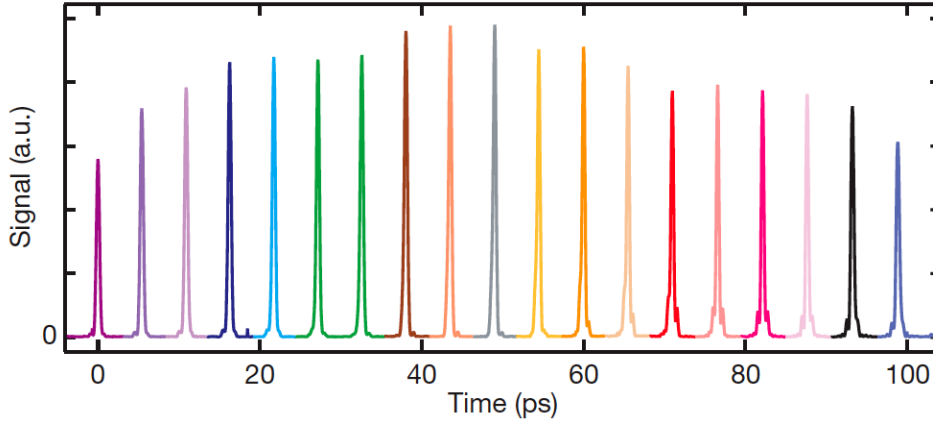


**Figure 3.7:** Characterization of the record length and resolution of the optical oscilloscope by scanning a 342 fs Gaussian input signal through the record length[1].

The single-shot capability of the temporal imaging system is also demonstrated, hereto the OSA is replaced by a single-shot spectrometer (infrared camera). Three single-shot optical waveforms composed of two pulses with temporal separations of 86 ps, 27 ps and nearly temporally overlapping are measured and presented in figure 5.3.4. The measurements are compared with a multiple-shot cross-correlator[26]. The measurement shows interference fringes (red) with a period of 3 ps which are caused by the overlapping of the two pulses. The resolution in this set-up is limited by the used infrared camera, using a better (commercially) available camera can utilize the full record-length-to-resolution ratio (150 ps / 220 fs) of the optical oscilloscope.

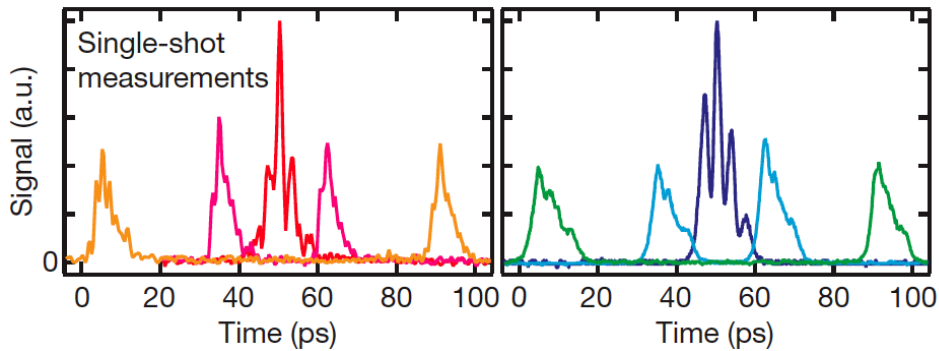


**Figure 3.8:** Single-shot measurement of the optical oscilloscope compared with the multiple-shot cross-correlator [1].

In the article several practical constraints are mentioned. First of all: third order dispersion (TOD) in the dispersive fibers leads to aberrations. A pump signal distorted by TOD doesn't impose the desired perfect quadratic phase. Secondly the FWM conversion bandwidth has an influence on both the record length and resolution. Finally the spectrometer performance is ultimately the limiting factor for the temporal resolution. In the following chapter these issues are tackled and expanded to gain insight of the different system parameters.

### 3.3 Alternative pulse measurement schemes

To understand the value of the measurement technique which is explored throughout this thesis work, it is necessary to compare it with other existing pulse measurement methods. This section highlights three of the most popular characterization techniques that are utilised for ultrashort pulse measurements.

The first method, autocorrelation, gives an indication of the measured pulse width and shape, while the second, frequency resolved optical gating (FROG), gives amplitude and phase information hence allowing a complete characterisation of the pulse. The third method, optical sampling, is an intensity measurement technique and allows us to use the already existing slow-detectors to measure femtosecond pulses. In principle one would like to avoid the need for nonlinear effects as a measurement tool because this generally puts restrictions on the power which is to be used. But as will be clear after this section, nonlinear processes offer an easy way to extract information from a pulse. There are few measurement techniques that allow us to simultaneously retrieve the optical waveform and its phase for ultrashort laser pulses. Both of them are necessary if one wants to fully characterise an optical pulse. Also the optical time-lens oscilloscope doesn't allow us to get both the amplitude and phase of the signal. Its main advantage is its femtosecond accuracy and the fact that it is a direct single-shot measurement, and thus rapidly updateable.

### 3.3.1 Autocorrelation

In an intensity autocorrelator one splits up the pulse that has to be measured in two equal pulses. These replicas are variably delayed with respect to each other in such a way that the pulses scan through each other, it is thus self-referenced. The resulting beam is then focussed onto a nonlinear crystal where second harmonic generation (SHG) takes place. In the case of temporal overlap in the crystal a second harmonic beam will be generated. This beam is proportional to the intensity of the incoming field, which in this case results in:  $I = (E(t) + E(t - \tau))^2$ . This intensity has the crossproduct  $E(t) E(t - \tau)$  which is very valuable because when a slow detector measures this crossproduct one obtains the autocorrelation intensity of the signal. Mathematically this becomes [27]:

$$R(\tau) \propto \int_{-\infty}^{\infty} |E(t) E(t - \tau)|^2 dt = \int_{-\infty}^{\infty} I(t) I(t - \tau) dt \quad (3.11)$$

in which  $R(\tau)$  is the detected signal. In figure 3.9 the working principle is shown.

In the autocorrelator this crossproduct is filtered out spatially and detected by a photodetector. Some important remarks are to be made though: first of all, the direction of the pulse can't be retrieved by this method as  $R(\tau) = R(-\tau)$ . Secondly for every different type of pulse there is a different conversion factor to calculate the duration of the signal pulse. For example, if the incoming pulse is Gaussian then the duration of the measured signal (also Gaussian) has to be divided by 1.41. This can lead to misleading results as the input pulse shape is often not known in advance. Furthermore as pointed out in certain literature [28], complex pulses can show the same quasi-Gaussian autocorrelation trace although they are quite different. In short the autocorrelator is relatively easy to understand and use, but awareness of its ambiguity is necessary.

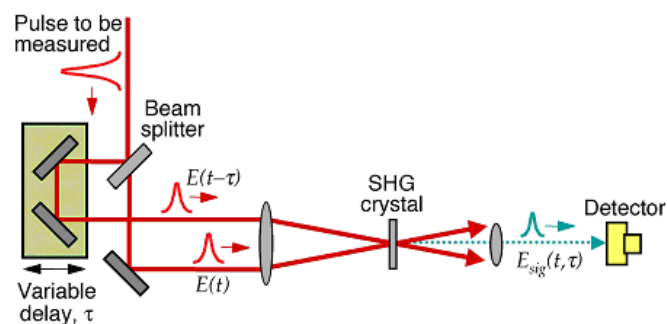


**Figure 3.9:** Working principle of an autocorrelator [29].

### 3.3.2 FROG

The acronym FROG stands for Frequency Resolved Optical Gating. It is classified as a spectrographic pulse characterisation technique. The output of a FROG-measurement is a spectrogram that shows how the spectral density of a signal varies with time. Examples of a spectrogram are shown in figure 3.10. It shows how the spectrogram of a Gaussian pulse varies according to its frequency chirp, hence showing that the measurement is sensitive to phase information.

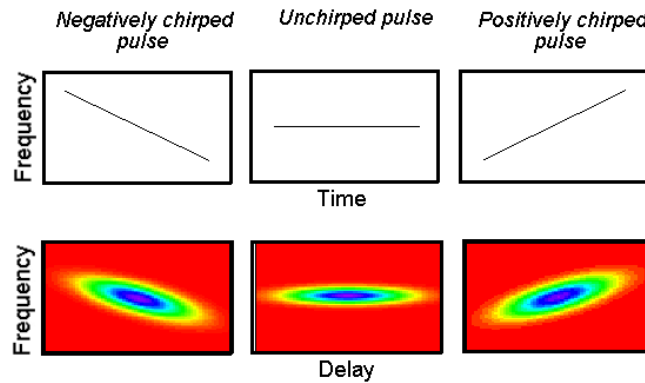


**Figure 3.10:** The spectrogram trace of a Gaussian pulse varies according to its frequency chirp [30].

Its working principle is very similar to that of an autocorrelator, the main change is at the detector side. Instead of measuring the signal temporal intensity  $I$  vs. delay, FROG involves measuring the signal spectral intensity  $S$  vs. delay. The spectrogram trace is given by [27]:

$$S(\tau, \omega) = \left| \int E(t) G(t - \tau) e^{i\omega t} dt \right|^2 \quad (3.12)$$

In which  $E(t)$  is the pulse, and  $G(t)$  is the gating function. The product  $E(t) * G(t - \tau)$  is called the signal field  $E_{sig}(t, \tau)$ . It is possible to show that  $E(t)$  can be obtained from the signal field  $E_{sig}(t, \tau)$  when there is a functional relationship between  $E(t)$  and  $G(t)$  [31], [32]. Therefore one extracts  $E_{sig}(t, \tau)$  from the measured trace  $S(\tau, \omega)$  which is a so-called 2D phase-retrieval problem.

Depending on the FROG implementation, certain ambiguities exist which need to be considered. In particular for the widely used SHG FROG [33], similar to the autocorrelator, there is a temporal ambiguity, and in addition there exists an ambiguity in the direction of the phase. [[34], [31]].

The resolution of a FROG measurement is very high as one can even measure 4.5 fs pulses [35]. An important disadvantage is the fact that FROG measurements cannot be used to

measure a pulse train with a small amplitude modulation as it will average over the height of the pulses.

### 3.3.3 Optical sampling

A very interesting method to perform a waveshape measurement is optical sampling. As our fastest electronic devices are too slow to measure ultrashort pulses due to the relatively long sample durations [36], one has to find a way to decrease the sample duration. By sampling with femtosecond (optical) pulses, the necessary accuracy can be obtained. The basic principle is as follows: the signal is combined with a low-repetition rate sampling pulse in a nonlinear medium creating an idler when temporal overlap occurs. For each sample we have an idler pulse with an energy proportional to the power of the signal at the position of temporal overlap with the sampling pulse. These idler pulses can be measured by a photodetector whereafter the temporal profile of the signal intensity can be displayed on an electrical oscilloscope. The sample pulse duration is a measure for the resolution. The operation principle is visualised in figure 3.11.

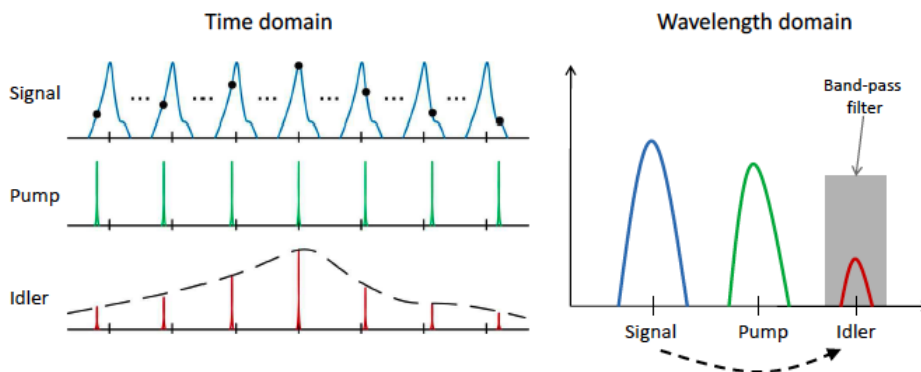


**Figure 3.11:** Principle of sampling an optical signal by four-wave mixing with a pump pulse train of low repetition frequency [37].

Recent research [37] uses FWM on a chalcogenide chip as the idler generating effect. The advantage is that this chip offers a very broad conversion bandwidth for FWM which is necessary because to measure short pulse widths, which have a corresponding broad spectral width, the center wavelengths of the pump and signal are required to be spaced far apart so that no spectral overlap occurs between the signal and pump spectrum.

Optical sampling cannot be used for measuring non-repetitive pulses because it depends on averaging over a great number of similar pulses, yielding the shape of that pulse. Hence, like the FROG limitation, it doesn't allow us to do single-shot measurements of an amplitude

modulated pulse train.

### 3.4 Conclusion

In this chapter we gave an overview of the three main experimental set-ups that can be used to implement a time-lens for ultrashort measurement of (sub-) picosecond pulses. Clear reasons are given why FWM is preferred over the EO modulator and XPM implementation. Basically an EO modulator cannot provide subpicosecond resolution and the XPM implementation is not flexible nor tunable enough, as for every type of signal an optimal pump pulse should be created via a new design of a fiber bragg grating.

Many other pulse characterisation techniques exist and we described the most popular of which include autocorrelation, FROG and optical sampling. Although our time-lens implementation doesn't allow us to measure the phase of the pulse, it does have the potential to measure complicated pulse shapes exactly over a long record time. Furthermore it can achieve single-shot measurements of amplitude modulated pulse trains which offers a great advantage over FROG and optical sampling.

In the next chapter we focus on the FWM time-lens implementation and investigate if we can optimize the FWM time-lens set-up of the third key experiment [1].

## Chapter 4

# Design guidelines and optimisation of the FWM time-lens set-up

### 4.1 Introduction

As outlined in chapter 3, we have chosen to implement the time-lens method which uses FWM to perform a Fourier transform on the signal. This FWM time-lens method is preferred because it can accurately measure femtosecond pulses while the EO-modulator only offers sub-picosecond resolution. Additionally it is also a more tuneable method than the XPM time-lens (which also offers femtosecond resolution). The essential operation of a FWM time-lens is to impart the parabolic phase of a linear chirped pump pulse on the dispersed signal via four-wave-mixing in a nonlinear medium. This chapter explores the different aspects of the FWM set-up which is demonstrated in figure 4.1.

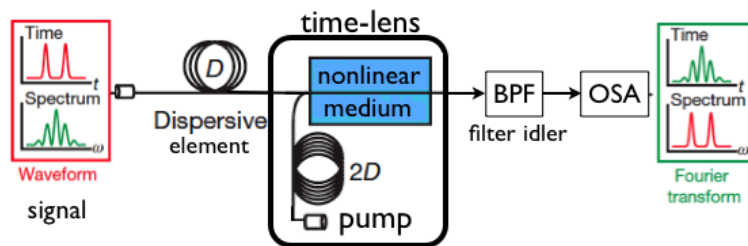


**Figure 4.1:** Temporal imaging via the FWM time-lens set-up which is investigated in this thesis work.

The FWM set-up consists of the two basic building blocks of a temporal imaging system, namely a dispersive element and a time-lens. The authors of reference [1] demonstrated a time-lens on chip using dispersion compensating fiber (DCF) as dispersive element and FWM



on a silicon chip as the time-lens. We investigate their set-up via simulations in Matlab®. The simulations are based on the nonlinear Schrödinger equation which we solve via the split-step Fourier method which is explained in the first section. The results of the simulations will show why we opt in this thesis to use a reconfigurable pulse shaper as the dispersive element instead of a fiber and FWM on a chalcogenide chip as the lensing element.

The first series of simulations explores the influence of the use of a fiber as the dispersive element via simulations assuming an ideal time-lens. This is also a proof-of-concept of the Fourier transform regime of the temporal imaging system, hence we can verify the results from chapter 2. Furthermore the simulations are used to determine how much dispersion is needed and when third order dispersion (TOD) aberrations come into play. The second series of simulations studies the influence of the FWM time-lens assuming a perfect dispersive element which doesn't show TOD.

The next part of the chapter constitutes a detailed survey of all influencing parameters of the FWM time-lens set-up which leads to a design strategy. The design strategy is focused on the measurement of Gaussian signals as this can serve as a general guideline for more complex signals. We will also show that the FWM time-lens set-up can be used to measure a pulse train with varying amplitude, showing its advantage over spectrographic pulse measurement techniques like FROG and optical sampling, neither of which are capable of measuring this type of pulse train.

To finish the chapter we clearly state the advantages of using a pulse shaper as the dispersive element and how we can implement the FWM time-lens set-up using the pulse shaper. Essentially the use of a pulse shaper will strongly reduce TOD aberrations and allows us to create a reconfigurable set-up where the performance can be adjusted according to the signal it has to characterize.

Small remark for the reader: there will be four types of fiber used in the simulations, namely SMF, DCF, HNLF and chalcogenide waveguide. Their characteristic parameters are given in the appendix A.4 and are not changed throughout the simulations unless stated otherwise.

## 4.2 Split-step Fourier method

The split-step Fourier method [9] is a popular way to solve the pulse propagation in nonlinear dispersive media. Its starting point is the nonlinear Schrödinger equation:

$$\frac{\partial A}{\partial z} = -\frac{i}{2}\beta_2 \frac{\partial^2 A}{\partial \tau^2} + \frac{1}{6}\beta_3 \frac{\partial^3 A}{\partial \tau^3} + \frac{i}{24}\beta_4 \frac{\partial^4 A}{\partial \tau^4} - \frac{\alpha}{2}A + i\gamma|A|^2 A - \frac{\gamma}{\omega_0} \frac{\partial}{\partial \tau} (|A|^2 A) - i\gamma T_R A \frac{\partial}{\partial \tau} (|A|^2). \quad (4.1)$$

We now rewrite this equation via the operators  $\hat{N}$  which describes the nonlinear effects and  $\hat{D}$  which incorporates dispersion:

$$\frac{\partial A}{\partial z} = (\hat{D} + \hat{N})A \quad (4.2)$$

with

$$\hat{D} = -\frac{i\beta_2}{2} \frac{\partial^2}{\partial T^2} + \frac{\beta_3}{6} \frac{\partial^3}{\partial T^3} - \frac{\alpha}{2} \quad (4.3)$$

and

$$\hat{N} = i\gamma (|A|^2 + \frac{i}{\omega_i} \frac{1}{A} \frac{\partial}{\partial T} (|A|^2 A) - T_R \frac{\partial |A|^2}{\partial T}). \quad (4.4)$$

The main assumption of the method is that the dispersion and nonlinear operator act independently over a small distance  $h$ . This way for every step with distance  $h$  we first solve the equation for  $\hat{D} = 0$ , followed by solving for  $\hat{N} = 0$ . We can thus write:

$$A(z + h, T) = \exp(h\hat{D}) \exp(h\hat{N}) A(z, T). \quad (4.5)$$

Instead of solving the equation in the time-domain we turn to the frequency domain. We thus replace the differential operator  $\frac{\partial}{\partial T}$  by  $i\omega$  and the exponential operator action is then described via the Fourier transform  $F_T$ :

$$\exp(h\hat{D}) B(z, T) = F_T^{-1} \exp(hD(i\omega)) F_T B(z, T). \quad (4.6)$$

These equations can easily be implemented in Matlab<sup>®</sup>. A few iterations are needed for acceptable accuracy so that if for example we want to simulate the propagation of a pulse over a length of 1 m we iterate 10 times with  $h = 0.1$  m. The number of iterations depends on the value of the dispersion parameters and the length of the pulse.

The method can be made more symmetrical which improves the accuracy. Instead of one dispersion step and one nonlinear step for every distance  $h$ , we then have the nonlinear step surrounded on either side with a dispersion step. This is called the symmetrized split-step Fourier method and it is used in the written Matlab<sup>®</sup> code.

### 4.3 Ideal time-lens

The aim of this section is to understand what the influence is of the fiber as dispersive element, so we assume an ideal time-lens which imparts a perfect parabolic phase. We simulate the following set-up: *dispersive fiber* - *ideal time - lens* - *OSA*.

#### 4.3.1 Proof-of-concept

The first simulation shows how a super-Gaussian input pulse is reproduced in the spectral domain. We choose a super-Gaussian pulse as it has a clear square-like shape, hence aberrations are easily recognized. The input pulse has a  $\tau_{FWHM}$  of 500 fs ( $t_0 = \tau_{FWHM}/1.665$ ) and is of the fifth order ( $m=5$ ):

$$A(z, \tau) = \exp(-1/2 (\frac{\tau}{t_0})^m)$$

We simulate a 50 m long fiber and compare between SMF (standard Single Mode Fiber) and DCF (Dispersion Compensated Fiber) with and without incorporating third-order dispersion (TOD). The results are shown in figures 4.2 and 4.3 . The green curve represents the spectrum of the idler and the blue curve is the incoming signal. We normalize both curves and we apply the time-to-frequency conversion factor ( $t = \Delta\omega/K$ ) to scale the (baseband) frequency axis to the time axis. As expected the spectrum of the idler is the same as the intensity profile of the incoming super-Gaussian in the time domain when we ignore TOD and this for both SMF and DCF. This is shown in figures 4.2.a and 4.3.a.

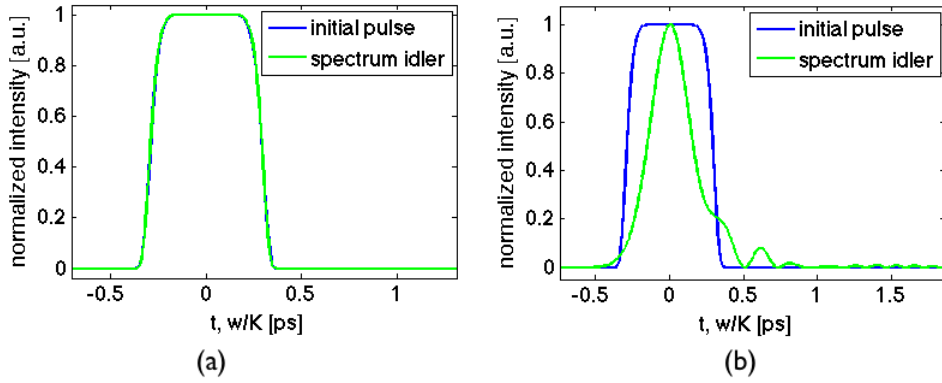


**Figure 4.2:** **a.** Frequency-to-time converted idler spectrum (green) reflecting the input pulse (blue) via the ideal time-lens set-up with 50 m SMF without TOD and **b.** with 50 m SMF with TOD.

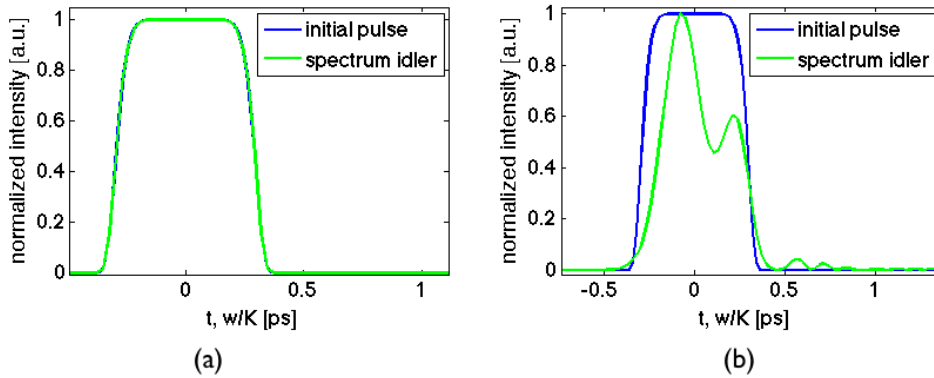


**Figure 4.3:** **a.** Frequency-to-time converted idler spectrum (green) reflecting the input pulse (blue) via the ideal time-lens set-up with 50 m DCF without TOD and **b.** with 50 m DCF with TOD.

As can be clearly seen, the inclusion of TOD effects results in an asymmetric idler spectrum and the introduction of a long oscillating tail. This is the expected behaviour of TOD[9].

We notice a distinct difference between SMF and DCF fiber as shown in figures 4.2.b and 4.3.b. The aberrations in the case of SMF are larger, because the dispersion slope is smaller in DCF. This is also the reason why the authors of reference [1] chose DCF as the dispersive fiber instead of SMF as they work with sub-500 femtosecond signals.

The distance after which the aberrations come into play is strongly dependent on the type of input pulse. For a 500 fs super-Gaussian with  $m=5$  after only 1 m of DCF we can already observe aberrations, while for a Gaussian ( $m=1$ ) with same duration, the first TOD-effects need 100 m of DCF to develop as shown in figure 4.4[a.]. This is a consequence of the fact that the steeper the edges of a pulse (more spectral bandwidth), the stronger the dispersion affects the pulse. Via the same reasoning we understand that also shorter pulses suffer more from TOD. A Gaussian pulse of 250 fs already shows TOD-aberrations after 40 m of DCF. This is shown in figure 4.4[b.].

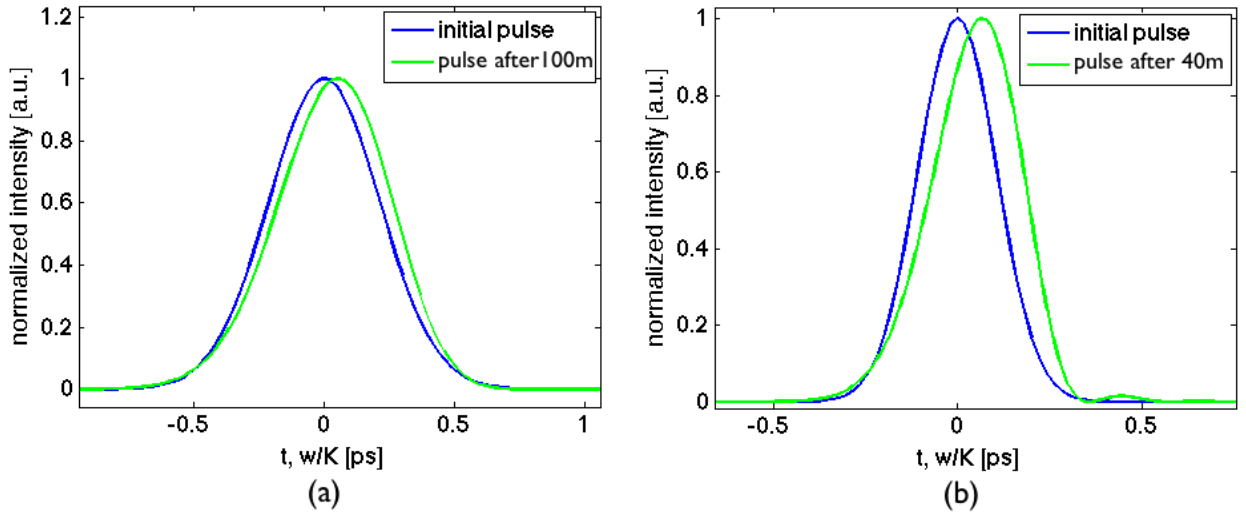


**Figure 4.4:** a. Evolution of a 500 fs Gaussian (blue) after 100 m DCF (green) b. Evolution of a 250 fs Gaussian (blue) after 40 m DCF (green).

This observation shows the first trade-off with a fiber as the dispersive element: if we want to measure a very short input pulse or a pulse with steep edges, the length of the dispersive fiber has to decrease because of TOD, which leads to a smaller record length via:

$$\tau_{rec} = \beta_2 L \cdot 2 \Delta\omega_p.$$

Figure 4.5 shows a rough estimate for the length  $L$  for which third-order aberrations start to play an important role as a source of aberrations in the ideal time-lens set-up for Gaussian pulses. If one wants to design a compact set-up, so to have a short length  $L$ , it is no longer

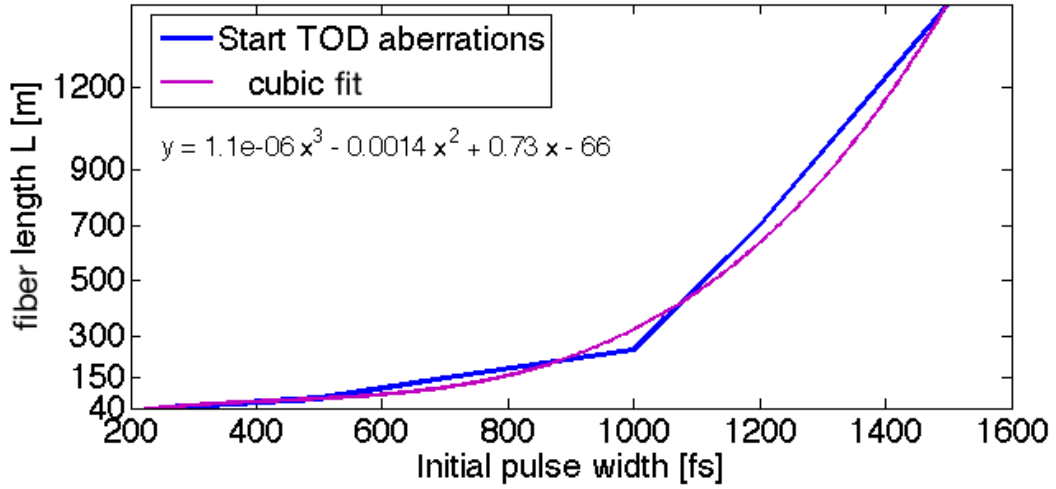


**Figure 4.5:** Dispersive fiber length (DCF) after which TOD aberrations come into play as a function of the initial pulse width for Gaussian pulses.

TOD which is an issue but merely the total amount of dispersion  $D_T$  needed to make the set-up work. We can define a minimum amount of dispersion via the dispersion length  $L_D = \frac{t_0^2}{\beta_2}$  [9] which is the length after which the pulse is significantly distorted by dispersion:

$$D_{min} = L_D D = t_0^2 \frac{2\pi c}{\lambda} \quad (4.7)$$

If  $D_T < D_{min}$  the pulse isn't affected by dispersion and hence it is as if there is no dispersive element in the set-up. Another issue is the idler bandwidth which grows inversely proportional to  $D_T$ . Consider the time-to-frequency conversion factor 2.37

$$\Delta\tau = \left(\frac{\lambda_s}{\lambda_i}\right)^2 D L \Delta\lambda_i = \left(\frac{\lambda_s}{\lambda_i}\right)^2 D_T \Delta\lambda_i,$$

in which  $D_T$  is the total dispersion. The idler bandwidth  $\Delta\lambda_i$  is thus:

$$\Delta\lambda_i = \frac{\Delta\tau}{\left(\frac{\lambda_s}{\lambda_i}\right)^2 D_T}.$$

The broadening of spectrum of the idler is inverse proportionally to total amount of dispersion  $D_T$ . Imposing a small dispersion implies the need for an OSA which is capable of measuring large spectral bandwidth. But more importantly, if we consider a wave-mixing process as the time-lens action then the generated idler should have a very broad spectrum which implies a broad spectrum for the pump (conservation of energy) and consequently an ultrashort pump which will immediately degrade because of TOD. So this shows the limits for the use of small dispersion values.

### 4.3.2 Sensitivity to the Fourier transform condition

In this section we simulate a set-up in which the Fourier transform condition is not exactly obeyed. As shown in figure 4.6[a] the idler spectrum of a 1 ps super-Gaussian ( $m=5$ ) pulse immediately shows serious aberrations. For a 1 ps Sech pulse the aberrations are less serious as demonstrated in 4.6[b].

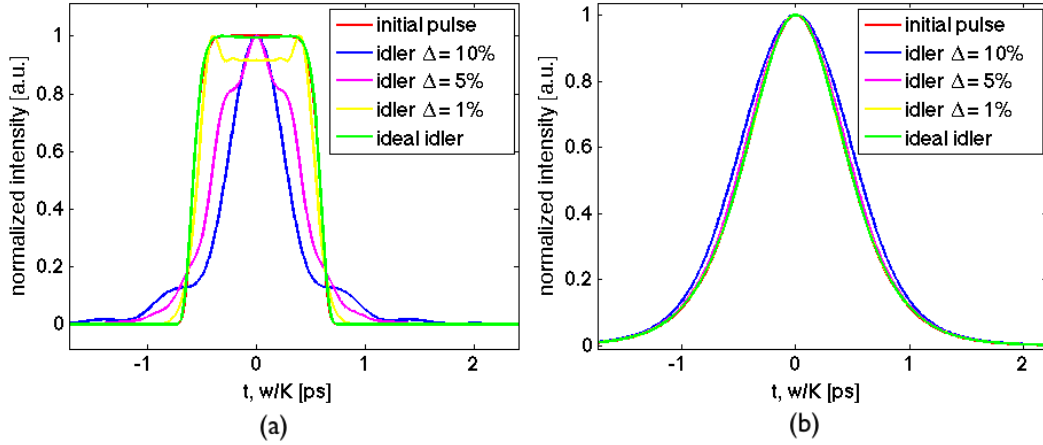


**Figure 4.6:** Impact of deviating 1%, 5%, 10% from the Fourier transform condition on the frequency-to-time converted idler spectrum for a **a.** super-Gaussian pulse and **b.** Sech pulse.

Just like for TOD aberrations, short and broad bandwidth pulses are affected the most.

## 4.4 FWM time-lens via NLS

In this section we discuss the consequences of the use of four-wave-mixing as a time-lens. The pump pulse's chirp is one delicate factor but especially the interaction between the pump and signal pulse in the spectral domain needs to be studied. Therefore we no longer assume an ideal time-lens (purely quadratic phase modulation) but implement it as the interplay of the pump and signal pulses which is described by the nonlinear Schrödinger equation.

### 4.4.1 Proof-of-concept

The first simulation is a proof-of-concept that FWM can indeed be used as a time-lens mechanism.

We simulate a 342 fs sech input pulse and a 280 fs Gaussian initial pump pulse. We send the input pulse through 50 m of DCF fiber and the pump pulse through 100 m of the same type

of DCF fiber. Furthermore we choose  $\beta_2(\lambda_s) = \beta_2(\lambda_p)$ . This makes sure that we obey the condition  $D_p = 2 D_s = 2 D$  which was derived in 3.2.3. We put  $\beta_3$  to zero so that if we notice aberrations, it is purely because of the used time-lens mechanism. We then send both pulses simultaneously through a chalcogenide waveguide where the FWM takes place. As the pump pulse and signal pulse have a different center wavelength,  $\lambda_{signal} = 1515$  nm and  $\lambda_{pump} = 1585$  nm and travel through a different length of DCF, they will not temporally overlap at the chalcogenide chip waveguide, breaking a necessary condition for FWM. Therefore we send the signals in their respective DCF fibers with the appropriate time delay to establish temporal overlap. This is made clear in figure 6.1 where the blue curves show the initial signal pulse and the signal after traveling 50 m through the DCF (thick). The green curves show the initial pump pulse and the pump<sup>2</sup> pulse after traveling 100 m in DCF (thick). After their travel through the dispersive fiber the pump and signal temporally overlap.

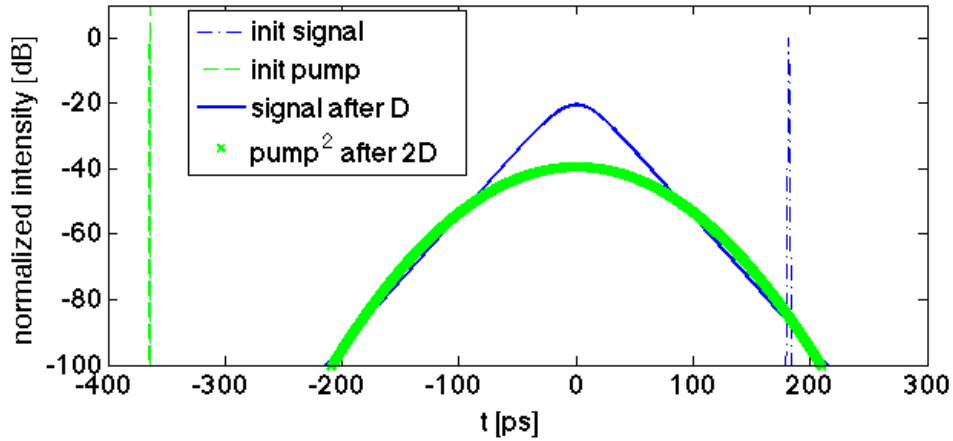


**Figure 4.7:** Evolution of the input and pump pulse after dispersion D and 2D respectively.

The next figure 4.8 shows the spectrum of the total field (signal + pump + idler) after the FWM-process in the chalcogenide chip. The pump ( $\lambda_p = 1585$  nm) and signal ( $\lambda_s = 1515$  nm) wavelength are far apart so that the idler doesn't spectrally overlap with the pump spectrum. The idler is at 1662.5 nm so it is not visible in this picture which zooms in on the pump and signal spectrum.

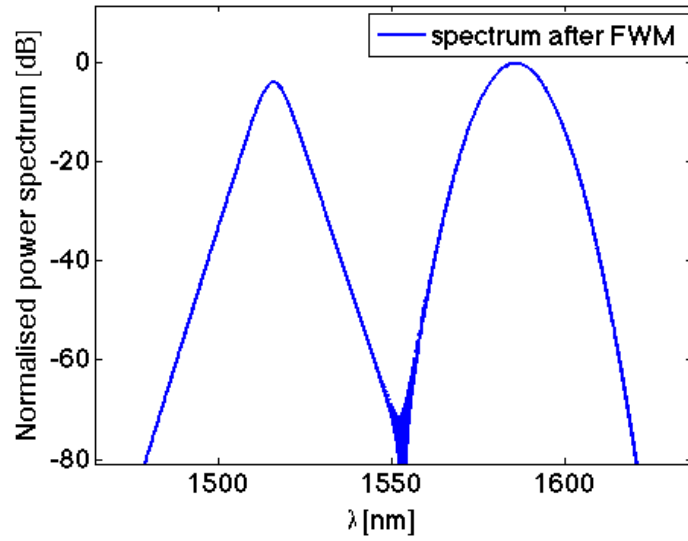


Figure 4.8: Spectrum signal and pump after the FWM process.

The key figure though is figure 4.9 which proves that the spectrum of the idler reflects the intensity profile of the incoming sech pulse.

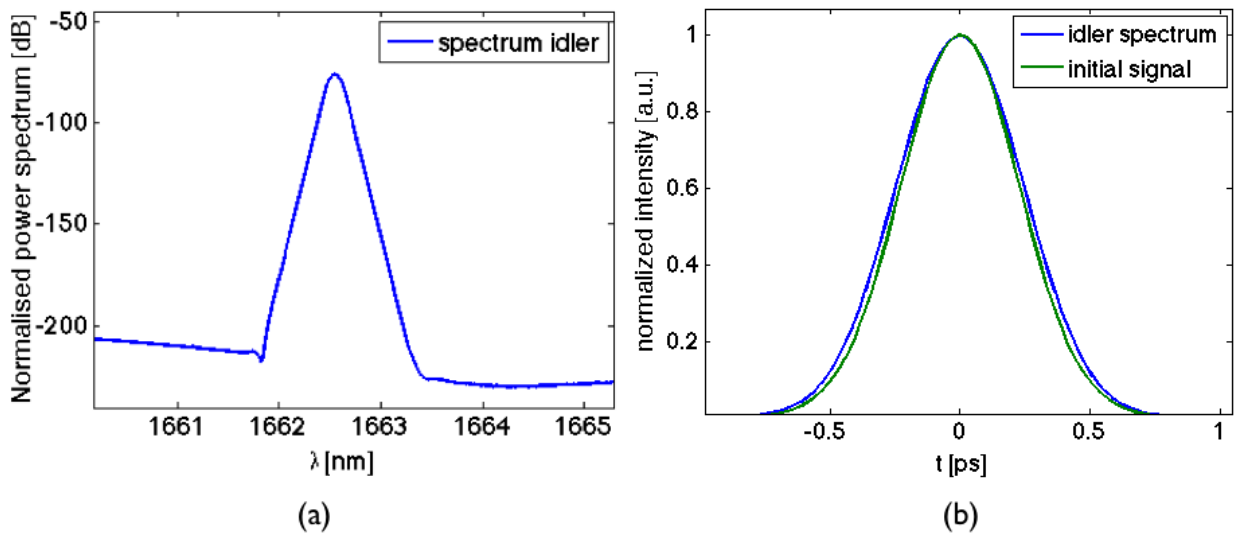


Figure 4.9: **a.** Normalized spectrum idler and **b.** Frequency-to-time converted spectrum idler, both reflecting the Sech shape.

We determine the FWHM spectral bandwidth of the idler to be 0.12 nm and with the time-to-frequency conversion factor equation 2.37 in terms of  $\Delta\lambda$  and the dispersion  $D$  of the DCF fiber we get:



$$\Delta\tau_{meas} = \left(\frac{\lambda_s}{\lambda_i}\right)^2 D L \Delta\lambda = 0.8387 \frac{ps}{nmkm} 0.050km 0.12nm = 0.433 \text{ ps}$$

The ideal resolution is  $\tau_{pump}/\sqrt{2} = 280 \text{ fs}/\sqrt{2} = 200 \text{ fs}$ . Given this resolution we calculate the actual pulse width from  $\tau_{meas}$ :  $\tau_{act} = \sqrt{\tau_{meas}^2 - \tau_{res}^2} = 0.384 \text{ ps}$  [1], which is close to the simulated signal length of 0.342 ps, indicating that the concept works. There is a discrepancy of only 42 fs while the used time step in the simulation was 30 fs.

It is important to realize that the dispersion parameter  $\beta_2$  is wavelength dependent hence the choice  $\beta_2(\lambda_s) = \beta_2(\lambda_p)$  is in general not possible. Recall that it is the total dispersion of the pump which has to be twice the total dispersion of the signal. As the pump and signal are at different wavelengths, their  $\beta_2$  differs and thus sending the pump through twice the length of the dispersive element of the signal is in principle not enough.

## 4.5 Design guidelines

In this section we want to give a framework to fit in the influence of the different parameters. We first repeat the two basic equations which are a measure for the performance of our system:

$$\tau_{rec} = 2 \beta_2 L \Delta\omega_p$$

$$\tau_{res} = \frac{\tau_p}{\sqrt{2}}$$

Just by looking at the equations we know that if we have a very short pump pulse (small  $\tau_p$  and large  $\Delta\omega_p$ ) we increase the record length and achieve better resolution. The parameter  $\beta_2$  is relatively fixed for us because it depends on the type of dispersive element used. Generally this is DCF, as it minimizes the third-order-dispersion aberrations. So at first glance it comes down to maximizing the length parameter L and spectral bandwidth of the pump. But an increase in L can lead to TOD issues if the signal pulse is short as shown in 4.3.1. Also increasing  $\Delta\omega_p$  means that in the dispersive path of the pump TOD comes into play which leads to non-ideal lens action. There are two issues though which make it more complicated than this. The first issue is temporal overlap during the FWM process, which is, except from a synchronization issue, also dependent on the relative duration of the pump and signal pulse. The temporal overlap is essential because otherwise only part of the signal will undergo lens action. The second issue is spectral overlap which is unwanted because we need to filter out the idler after the FWM. Spectral broadening due to SPM<sup>1</sup> in the HNLF can cause this overlap so it also restricts the (peak) powers we'll use.

<sup>1</sup>SPM is the acronym for self-phase-modulation, a nonlinear effect originating in the optical Kerr effect. SPM causes the pulse intensity to modulate the refractive index. Hence the pulse changes its own phase, resulting in a distorted signal spectrum.

We will now study in more detail the following design issues:

- optimal length dispersive elements
- influence of spectral overlap between signal and pump pulse
- influence of temporal overlap between signal and pump pulse
- walk-off in HNLFF

After these individual discussions we shall be ready to implement a design strategy.

### 4.5.1 Length dispersive element

If we assume a Gaussian pulse the criteria for third-order dispersion to become significant is [9]:

$$t_0 \left| \frac{\beta_2}{\beta_3} \right| \leq 1$$

For the used DCF fiber and converting to  $t_{FWHM}$  we get the condition:

$$t_{FWHM} \leq 4.5 \text{ fs.}$$

This criteria states that if we send in a 4.5 fs (Gaussian) pulse we will immediately get distortions. In our set-up TOD will not dominate from the beginning as long as we work with longer signals, but its influence is large enough to distort a  $>4.5$  fs pulse when the distance travelled by that pulse is long enough.

The way to choose the length  $L$  of the dispersive element is via a simulation of the ideal-lens set-up as shown in section 4.3 with the desired signal. As long as there are serious deviations from the expected performance the length must decrease. Once the length is determined for the signal a similar simulation must be done for the pump pulse which travels over approximately two times the length if  $\beta_2(\lambda_{signal}) \approx \beta_2(\lambda_{pump})$ . If the pump pulse also suffers from TOD, again a decrease in length must follow. As the length through which the signal travels will decrease accordingly, we are guaranteed to have no aberrations on the (parabolic) phase of the signal and on the phase of the pump.

Having a length shorter than the length after which TOD comes into play, is a fundamental constraint for the choice of the length  $L$ .

### 4.5.2 Temporal overlap

To have FWM the two pulses must temporally overlap. The less they overlap the less idler will be generated. We recall that for FWM we have

$$A_i(t) \propto A_p^2(t) A_s^*(t) \quad (4.8)$$

with  $A_p$  the envelope of the pump pulse and  $A_s$  the signal envelope. So it is actually the temporal overlap of  $A_p^2$  and  $A_s^*$  which matters. As the pump pulse should impart its parabolic phase over the total signal in order to have no aberrations, the pump pulse squared should be longer than the signal pulse before the nonlinear medium where the FWM takes place. Also in order to overlap they will have to be sent into their dispersive elements with a relative delay because both pulses will generally have a different group velocity and thus arrive at the nonlinear medium at a different point in time. Furthermore, one wants to have a pump which is flat over the most significant part of the signal as the pump should only impose a quadratic phase and its amplitude should not influence the idler. In short these are the three main issues for temporal overlap which we'll now consequently discuss in more detail:

- $\tau_{pump}^2 \geq \tau_{signal}$  at nonlinear medium
- synchronizing the two pulses at the beginning of nonlinear medium
- flat amplitude pump over  $\tau_{signal}$

If we assume a Gaussian pump and a Gaussian signal it is relatively easy to find an optimal initial pump and signal duration independent of the dispersion  $D$ . To obey the Fourier transform condition, the pump experiences twice the amount of dispersion as the signal so if we take the initial duration of both signals to be the same, the signal fits under the pump. However, because of the third issue it is advantageous to choose the pump shorter than the signal pulse, because it will have broadened more and thus the pump is flat over a longer period of time. In the next figure 4.10 we visually represent the different optimum  $\tau_{pump}$  and  $\tau_{signal}$  combinations. The blue region gives all possible combinations that assure temporal overlap. The green region is a forbidden region where the pump is initially too long compared with the initial signal length. The intersection line is described as:  $\tau_{signal} = \frac{\tau_{pump}}{\sqrt{2}}$  and is equivalent with  $\tau_{pump}^2 / \tau_{signal} = 1$  just before the FWM process. The intersection line equation strongly reminds of the expression for the resolution of the set-up as given by [1] namely  $\tau_{resolution} = \frac{\tau_{pump}}{\sqrt{2}}$ . Indeed if we are in the green region only an (initial) signal part as large as  $\frac{\tau_{pump}}{\sqrt{2}}$  will undergo lens action and thus the smallest resolvable feature has that length  $\frac{\tau_{pump}}{\sqrt{2}}$ . Figure 4.10 is independent of the applied dispersions  $D$  and  $2D$  and thus in this specific case of a Gaussian signal and pump, it is possible to choose  $L$  via the procedure as described in the previous section.

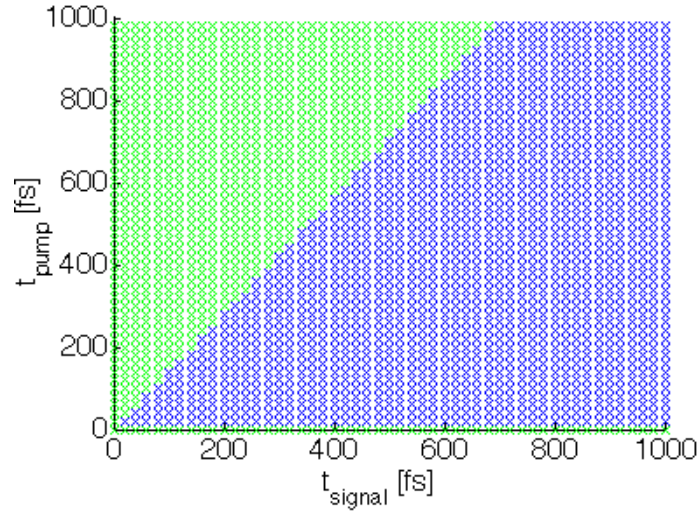


**Figure 4.10:** Blue region shows the valid choice of initial  $\tau_{pump}$  and  $\tau_{signal}$  so that the pump and signal temporally overlap after a dispersion of respectively  $2D$  and  $D$ .

If we no longer assume unchirped Gaussian pulses but consider pulses with an initial non-zero phase, the situation turns much more complicated. Basically we want to know exactly how much our signal pulse broadens after a dispersion  $D$  so that we can determine the width of the pump so that  $\tau_{pump}^2 \geq \tau_{signal}$  at the beginning of the FWM. But this broadening depends strongly on the initial phase or chirp of the signal which we, in principle, don't know in advance. One of the consequences of this uncertainty is that the choice of the length can be of high importance as alluded to in the previous section. We can easily show this by considering a simple example of a chirped Gaussian signal pulse (with  $\tau_{FWHM} = 1.665 t_0$ ) described via its chirp parameter  $C$ :

$$A_{signal}(t) = e^{\frac{1+iC}{2} \left(\frac{t}{t_0}\right)^2}. \quad (4.9)$$

Depending on the travelled length  $L$  and the sign of the chirp parameter the pulse is compressed or broadened faster than an unchirped Gaussian. This different behaviour on  $L$  and  $C$  is shown in figure 4.11. If we have an anomalous dispersive fiber ( $\beta_2 < 0$ ) and a negative  $C$  or vice versa a positive  $C$  in a normal dispersive fiber ( $\beta_2 > 0$ ), a pulse which traveled a distance smaller than the dispersive length  $L_D = \frac{t_0^2}{|\beta_2|}$  becomes shorter[9].

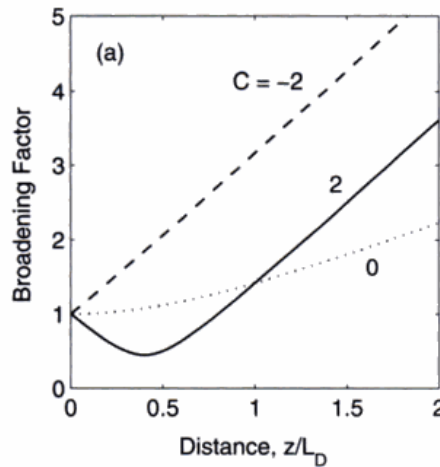


**Figure 4.11:** Broadening with distance in an anomalous dispersive fiber for different signs of  $C$  [9].

On the other hand a Gaussian pump (which should be transform-limited as the pump should only impart a parabolic phase !) broadens much slowly than the chirped pulse for  $L > L_D$ . So to obey the  $\tau_{pump}^2 \geq \tau_{signal}$  condition we can no longer choose a pump pulse which has approximately the initial duration of the signal pulse, because it won't be broad enough after  $2L$  to entangle the signal.

We now turn to the second item in the 'issue' list namely synchronization of the signal and pump pulse at the FWM process. We can follow a relatively easy guideline by observing solely the center wavelengths of the signal  $\lambda_{signal}$  and pump pulse  $\lambda_{pump}$ . We can calculate the walk-off caused in the dispersive elements and use this value as the delay we should impose. Fine-tuning the synchronization can consequently be done by considering the strength of the idler in function of an incremental delay. The choice of the center wavelengths is important to avoid spectral overlap, as will be clear later on.

The final item concerns the flatness of the pump relative to the signal envelope. A very important observation is that the flatness of the pump makes the record length dependent on the type of signal pulse. An example helps understanding this. Consider a super-Gaussian signal which has a flat peak and a sech signal which has a sharp peak. The slope of the super-Gaussian signal in the most important part of the pulse is almost zero while the slope of the sech signal on both sides of the center is very steep. The amplitude of the product  $A_i(t) \propto A_p^2(t) A_s^*(t)$  is ideally proportional  $A_s^*$  as the pump then only imparts a parabolic phase. So a change in  $A_s^*$  must dominate over the change in  $A_p^2$  during the length of the signal. For the sech signal this is easily accomplished because the pump must vary greatly over a short time span if it is to dominate the steep slope of the sech pulse. In contrast a small variation of the pump over the flat top of the super-Gaussian signal makes that the

pump shape dominates over the signal shape.

A correct definition of the record length should be: ‘the maximum duration of the input signal that is truthfully represented via the spectrum of the idler’. So if the influence of the (temporal) pump shape compared with the signal is too large, the idler doesn’t reflect the signal and consequently the record length is limited by this. The standard formula for the record length  $\tau_{rec} = 2 \beta_2 L \Delta\omega_p$  doesn’t include this sense of good reproduction, as it doesn’t take into account the curvature of the pump amplitude. The following figures 4.12 and 4.13 illustrate the influence of the pump curvature for a super-Gaussian signal:

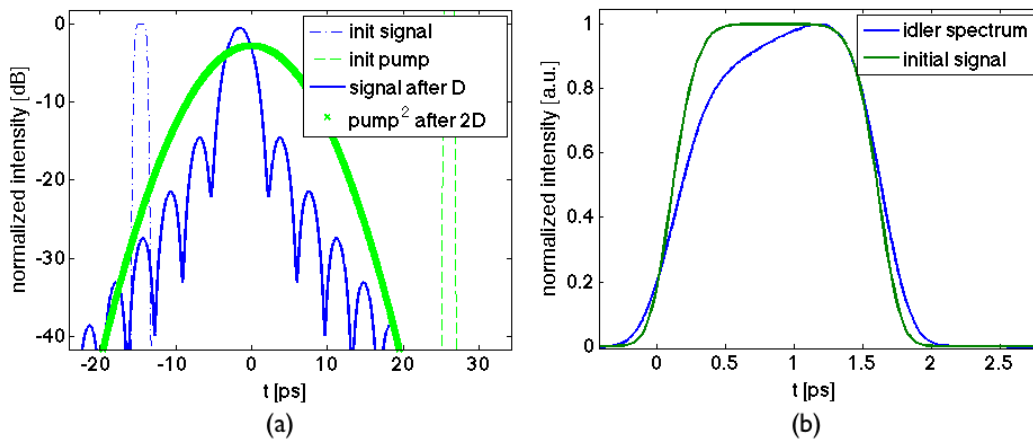


**Figure 4.12:** **a.** 1.5 ps super-Gaussian ( $m=2$ ) signal (blue) and 400 fs Gaussian pump squared (green) after dispersion of respectively D and 2D in DCF **b.** Idler shape is affected by the slope of the (squared) pump pulse.

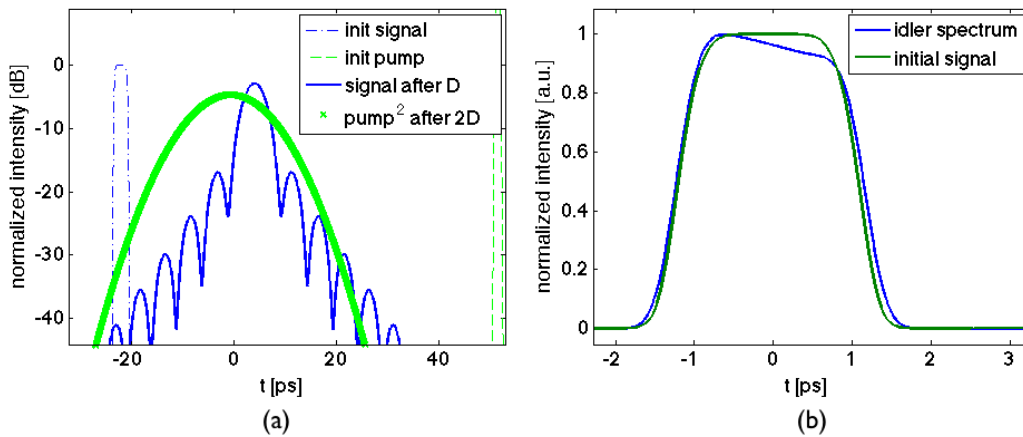


**Figure 4.13:** **a.** 2.2 ps super-Gaussian ( $m=2$ ) signal (blue) and 600 fs Gaussian pump squared (green) after dispersion of respectively D and 2D in DCF **b.** Idler shape is affected by the slope of the (squared) pump pulse.

In figure 4.12 the signal (blue) experiences a positive slope of the pump pulse (green) hence the idler reflects this positive slope. Vice versa as shown in figure 4.13 the idler shows a negative slope because the signal experiences a negative slope of the pump.

In figure 4.13 the deviation is larger as we chose a relatively shorter signal compared to the pump hence the pump slope effect is stronger. Small remark: the center wavelength of the idler shifts according to the relative temporal position of the pump compared to the signal. This shows how we can ‘scan’ through the record length.

As showed in the above paragraph the required flatness of the pump depends on the signal one wants to measure. For Gaussian pulses we have an analytical formula for the broadening therefore we could make the following figure 4.14 which shows how the degree of flatness, represented by  $\frac{\tau_p^2}{\tau_s}$ , varies with the initial fraction  $F$  defined via  $\tau_{p0} = F \tau_{s0}$ . It clearly shows that the initial pump width  $\tau_{p0}$  must be at most half of the initial signal width  $\tau_{s0}$  before the pump can be considered flat. For this choice the pump<sup>2</sup> width before FWM is 3 times larger than the signal width. This figure is independent of the length  $L$  or  $\tau_{s0}$ .

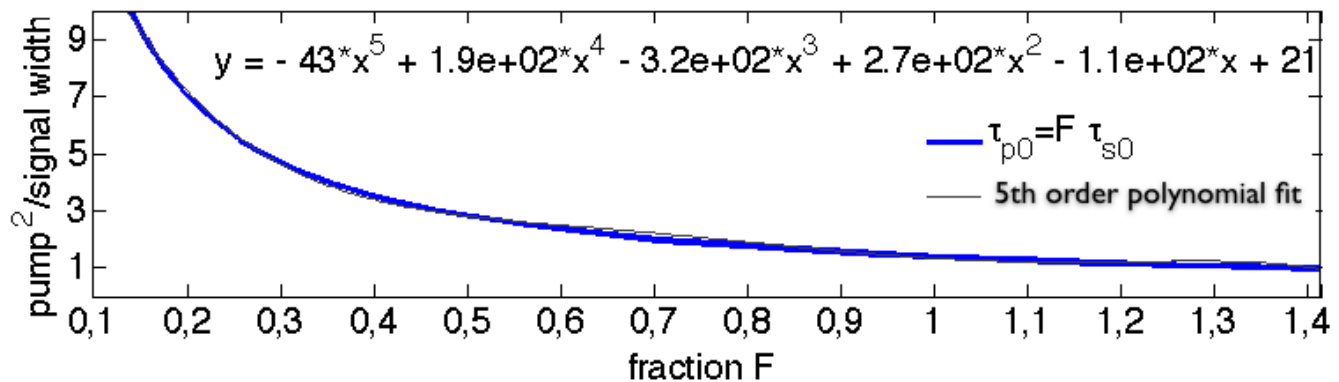


**Figure 4.14:** Degree of flatness of the pump in function of the fraction  $F = \frac{\tau_{p0}}{\tau_{s0}}$  for Gaussian pulses.

### 4.5.3 Spectral overlap

The time-lens oscilloscope principle can only work if we can extract the spectrum of the idler. In the case of spectral overlap between the pump and signal, the spectrum of the idler cannot be separated from the spectrum of the pump. So as we don't have a complete idler spectrum we don't know how the input signal looks like. This shows the critical importance of avoiding spectral overlap. If we send the input signal to an OSA, we know its center wavelength and bandwidth. Therefore we can choose the center wavelength of the pump so that the spectrum of the pump has no overlap with the signal. An extra restriction holds though as the conversion bandwidth of the FWM process is not infinite. If the pump-signal separation is too large the idler will end up too far away from the signal and pump, which makes phase

matching between the three waves harder to satisfy due to group velocity walk-off. As a result the idler generation dies out. The conversion bandwidth is dependent on the medium where the FWM takes place and on the pump power<sup>2</sup>.

Unfortunately this reasoning is not enough because even when the signal and pump are well separated the idler can still be on top of the pump spectrum. The exact conditions for this to occur is interesting for further investigation. But instead of deriving complicated (analytical) expressions we can determine the center wavelength and maximal bandwidth of the pump, which avoids spectral overlap, via a simple procedure. Our starting point is the following figure 4.15:

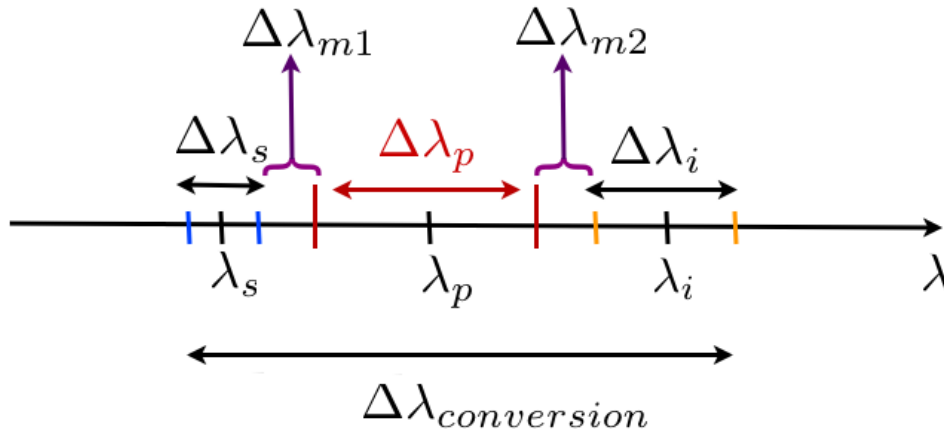


**Figure 4.15:** Spectral separation signal, pump and idler.

from which we derive:

$$\Delta\lambda_{conversion} = \left(\lambda_i + \frac{\Delta\lambda_i}{2}\right) - \left(\lambda_s - \frac{\Delta\lambda_s}{2}\right). \quad (4.10)$$

This equation 4.10 determines  $\lambda_i$  because  $\lambda_s, \Delta\lambda_s, \Delta\lambda_i, \Delta\lambda_{conversion}$  are in principle known. The next step is to calculate  $\lambda_p$  via:

$$\lambda_p = \frac{2\lambda_s\lambda_i}{\lambda_s + \lambda_i}. \quad (4.11)$$

Now we can invoke two conditions for the maximal possible  $\Delta\lambda_p$  so that the pump spectrum doesn't overlap with the signal and idler spectrum respectively:

$$\left(\lambda_p - \frac{\Delta\lambda_p}{2}\right) > \left(\lambda_s + \frac{\Delta\lambda_s}{2} + \Delta\lambda_{m1}\right) \quad (4.12)$$

$$\left(\lambda_i - \frac{\Delta\lambda_i}{2}\right) > \left(\lambda_p + \frac{\Delta\lambda_p}{2} + \Delta\lambda_{m2}\right) \quad (4.13)$$

<sup>2</sup>phase matching condition:  $\Delta k = k_s + k_i - 2k_p + 2\gamma P_p$  with  $P_p$  the pump power [38]



The terms  $\Delta\lambda_{m1}$  and  $\Delta\lambda_{m2}$  are two spectral margins and can be chosen according to own preferences. The most strict of conditions 4.12 & 4.13 applies. The following figure 4.16 shows the most stringent condition for each combination of  $(\Delta\lambda_s, \Delta\lambda_i)$  when  $\Delta\lambda_{conversion} = 150\text{nm}$ ,  $\lambda_s = 1530\text{nm}$  and  $\Delta\lambda_{m1} = \Delta\lambda_{m2} = 5\text{nm}$ . The forbidden region (yellow) results in a negative  $\Delta\lambda_p$ .

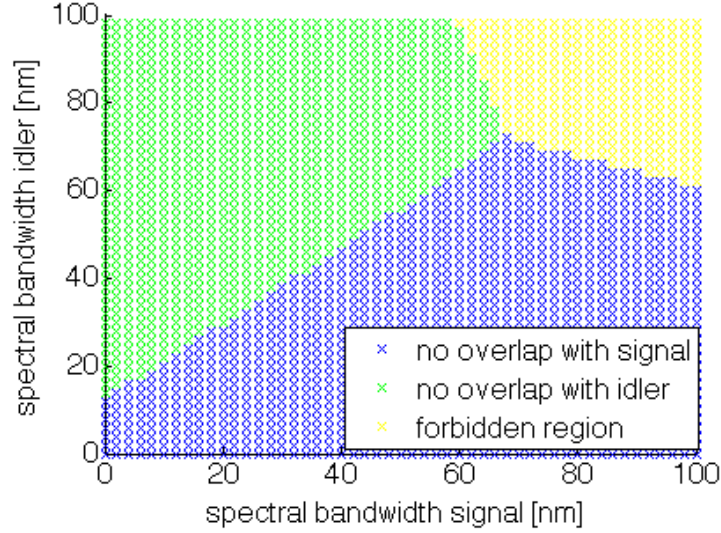


**Figure 4.16:** Most stringent no-spectral-overlap condition for each combination of  $(\Delta\lambda_s, \Delta\lambda_i)$  when  $\Delta\lambda_{conversion} = 150\text{nm}$ ,  $\lambda_s = 1530\text{nm}$  and  $\Delta\lambda_{m1} = \Delta\lambda_{m2} = 5\text{nm}$ .

Every point in the blue and green regions of figure 4.16 is associated with a maximum  $\Delta\lambda_p$  so that no spectral overlap is present. If we assume transform limited Gaussian pulses we can also derive a minimum  $\Delta\lambda_p$  from the needed temporal overlap condition:

$$\Delta\tau_{p0} \leq \sqrt{2} \Delta\tau_{s0} \Rightarrow \frac{\lambda_s^2}{\Delta\lambda_s} \leq \frac{\lambda_p^2}{\Delta\lambda_p}. \quad (4.14)$$

Hence we know the minimum and maximum  $\Delta\lambda_p$  for the time-lens oscilloscope to perform acceptable.

The nonlinear effect of self-phase-modulation (SPM) which results in spectral broadening can cause spectral overlap of the signal and pump during the FWM process, which is unwanted. Luckily one can avoid SPM by working with lower peak powers for signal and pump.

Again a small remark: even if there is no spectral overlap between the idler and pump, considering the 3dB bandwidth of the pump, the idler spectrum can still be on top of the low power parts of the pump spectrum. Therefore the idler spectrum can still be amplitude modulated by this effect.

#### 4.5.4 Walk-off in HNLF

As explained above, temporal overlap of the signal and pump pulse in the four-wave-mixing process is required otherwise no lens action takes place. Because the signal and pump are at different wavelengths in order not to spectrally overlap, we know that dispersion will cause them to walk-off from each other. The result is smaller temporal overlap and hence inefficient idler generation. In other words the FWM conversion bandwidth is limited in HNLF. We can use the following equation to calculate the walk-off [39]:

$$\Delta t = \frac{\Delta\lambda (2D - S\Delta\lambda)L}{2} \quad (4.15)$$

In which  $D (= \frac{2\pi c}{\lambda_p^2} \beta_2)$  is the dispersion at  $\lambda_p$  and  $S$  is the dispersion slope in the HNLF. The length of the fiber is  $L$ . The separation between the center wavelength of the pump and signal is  $\Delta\lambda = \lambda_p - \lambda_s$ . The left-hand side  $\Delta t$  gives the delay between the center wavelengths after travelling a distance  $L$ . The dispersion at  $\lambda_s$  is related to  $S$  via  $D = S(\lambda_p - \text{ZDW})$  with ZDW the zero dispersion wavelength of the HNLF. A symmetrical position of  $\lambda_s$  and  $\lambda_p$  around ZDW makes that the group velocities of the signal and pulse are matched so that there is no walk-off:  $\Delta t = 0$ . For a 30 m long HNLF with a ZDW = 1550 nm the following figure 4.17 shows the walk-off in function of  $\Delta\lambda$ , for different positions of  $\lambda_p$  towards the ZDW.

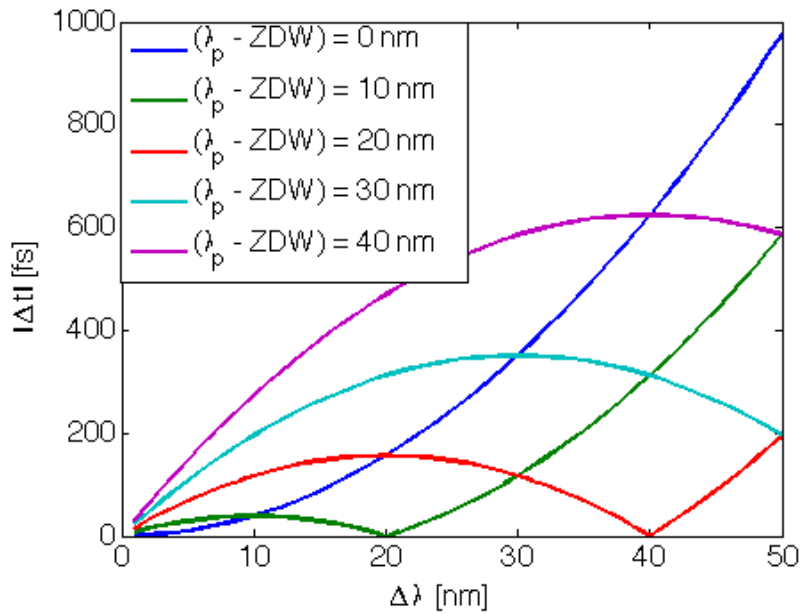


**Figure 4.17:** Walkoff as a function of the center wavelength separation  $\Delta\lambda$  of the pump and signal for 30 m of HNLF.

The sign of the delay is not important that is why we plot  $|\Delta t|$ . Except from generating walk-off between the signal and the pump, the nonlinear medium can also distort the signal

and pump individually because of the long fiber distance. This is obviously unwanted. Walk-off is no issue in the short dispersion engineered chips, like the chalcogenide chip [[38],[40]]. These are designed specifically to combine maximal temporal overlap with a maximal conversion bandwidth. The choice between the use of a dispersion engineered chip over HNLF as the nonlinear medium in which the time-lens action takes place, is generally based on the following:

- Advantages of dispersion engineered chip over HNLF
  - Signals do not distort during propagation
  - Very large conversion bandwidth (up to 500 nm [38])
  - High conversion efficiency
  - Compact
- Disadvantages of dispersion engineered chip
  - Large insertion losses
  - Fragile component
  - High cost

Essentially the dispersion engineered chip is far superior when it comes down to the measurement of ultrashort complicated signals. In this case both the signal and pump have a broad spectral bandwidth, hence the no-spectral overlap condition dictates a large difference  $\lambda_s - \lambda_p$ . Only a very large conversion bandwidth can then provide the required FWM.

## 4.6 Design strategy for a Gaussian signal

In this section we combine all insights gained thus far to design a FWM time-lens set-up, using dispersive fiber, for the measurement of Gaussian signals. It can serve as a guideline for any type of input pulse. We follow an iterative procedure so to optimize all parameters. The order of magnitude of the duration of the input signal  $\tau_s$  must be known in advance. The structure of the design approach is shown in figure 4.18. In general the key figures of merit are the record length  $\tau_{rec}$  and the resolution  $\tau_{res}$ . From the resolution requirement we can immediately derive the minimum spectral bandwidth of the (Gaussian) pump  $\Delta\omega_p$ :

$$\tau_{res} = \frac{\tau_{p0}}{\sqrt{2}} = \frac{0.44 \times 2\pi}{\sqrt{2} \Delta\omega_p}. \quad (4.16)$$

The resolution also shows the shortest signal with width  $\tau_{s0}$ , which can be accurately reproduced:

$$\tau_{s0} \leq \tau_{res}. \quad (4.17)$$

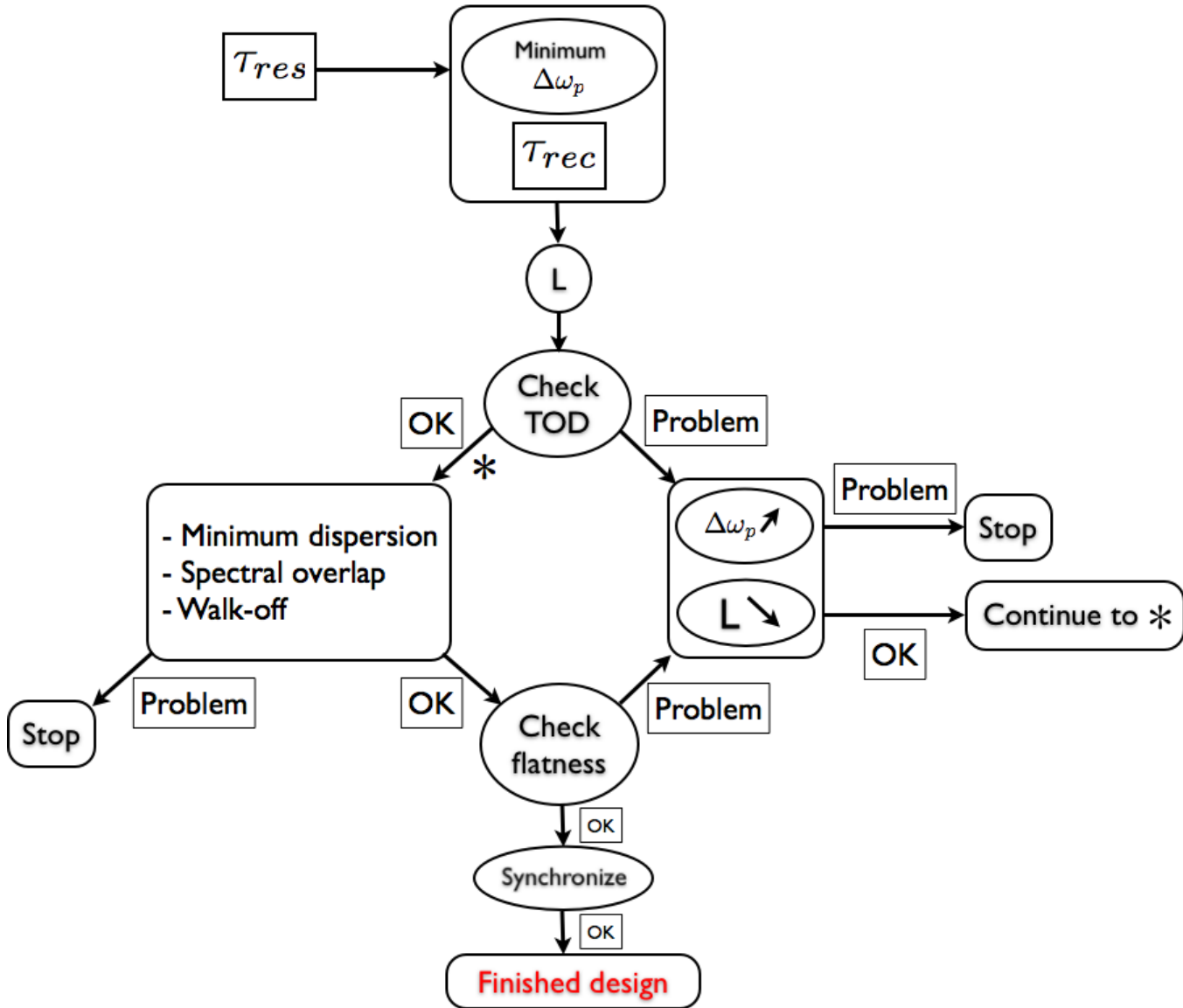


Figure 4.18: Design strategy for Gaussian signal and pump.

Given the minimum  $\Delta\omega_p$  we can calculate the needed length for the required record length:

$$L = \frac{\tau_{rec}}{\beta_2 \Delta\omega_p} \quad (4.18)$$

The  $\beta_2$  in the record length expression holds for the signal wavelength. The easy design rule  $L_p = 2 L_s$  which is advantageous from a practical point of view, can be used if the difference  $\lambda_p - \lambda_s$  is smaller than 40 nm, assuming a constant dispersion parameter  $D = \frac{-2\pi c}{\lambda^2} \beta_2(\lambda)$ . This is the solution of the equation  $\beta_2(\lambda_s) = 0.95 \beta_2(\lambda_p)$ , so if the difference  $\lambda_p - \lambda_s = 40$  nm there is a deviation of 5% from the  $D_p = 2 D_s$  condition.

At this point we can do a simple simulation to check if our pump is distorted by TOD after a dispersion of  $D_p = 2 D_s$ . If this is the case we must lower the length  $L$  while increasing the pump bandwidth in order to still achieve the requested  $\tau_{rec}$ . But sometimes it will be impossible to avoid the TOD aberrations and so the requested combination of  $\tau_{rec}$  and  $\tau_{res}$  can simply not be achieved. If no TOD aberrations are present proceed to considering the spectral overlap.

If the FWM happens in HNLF we have to consider walk-off effects when determining  $\lambda_p$ . The use of the chalcogenide chip avoids this extra complication as long as its conversion bandwidth is sufficiently broad (order of 100 nm). For the most general design strategy we will assume FWM in HNLF. The starting point is the choice of the signal wavelength  $\lambda_s$ . Preferably the difference  $ZDW_{HNLF} - \lambda_s$  is not too large so that a quasi-symmetrical position of  $\lambda_p$  and  $\lambda_s$  towards the  $ZDW_{HNLF}$  can be chosen. This gives us the possibility an opportunity to decrease walk-off. With the chosen value of  $\lambda_s$  we determine the minimum dispersion  $D_{s,min} = (\frac{\tau_s}{1.665})^2 \frac{2\pi c}{\lambda_s}$ . If the product  $\beta_2 L < D_{s,min}$ , the signal is not affected by dispersion and the set-up will not work properly. If variation of  $\lambda_s$  doesn't allow to satisfy  $\beta_2 L > D_{s,min}$  the given combination of  $\tau_{rec}$  and  $\tau_{res}$  cannot be achieved.

After choosing the signal wavelength, the center wavelength of the pump can be determined via the walk-off constraints as shown in figure 4.17 in combination with the no-spectral overlap condition for the calculated  $\Delta\omega_p$  as shown in figure 4.16. Of course these figures depend on the parameters of the used HNLF, so taking these into account, similar plots should be made while designing the time-lens oscilloscope.

As a design rule we state that if the signal under test has a FWHM width  $\tau_s$  then the walk-off should be less than a fraction  $f$  of  $\tau_s$ :  $|\tau_{walkoff}| < f \tau_s$ . The value of this fraction depends on the temporal overlap between the pump and signal. If the signal shifts through the pump and part of the signal falls outside the pump, then this part is not Fourier transformed. Secondly

if the signal shifts to a region where the pump is not flat then, as previously described, the amplitude modulation of the pump distorts the signal. This effect depends on the type of signal. As we work with Gaussian signals a good, but relatively strict starting value for the fraction  $f$  is  $\frac{1}{2}$ . This value allows the top of the signal pulse to overlap with the half maximum point of the pump<sup>2</sup> pulse, hence giving a reasonably strong idler signal. If we fail to avoid spectral overlap between the pump and the signal and/or idler, the system will have minor performance.

The next step is to consider the flatness of the pump as shown in figure 4.14. If we are not satisfied we stay in the design loop. We run through this loop several times to find the optimal combination of  $\Delta\omega_p$  and  $L$ . If we cannot increase  $\Delta\omega_p$  any more and still remain with a non-flat pump, we will have to settle with this non-ideal pump shape. This again limits the performance of the time-lens oscilloscope. For each loop the above mentioned fraction  $f$  changes. It becomes less strict as the width of the pump<sup>2</sup> increases and thus the signal can walk-through the pump<sup>2</sup> over a longer distance without losing temporal overlap. It now comes down to choosing a fraction  $f$  which allows the signal to stay under the flat part of the pump<sup>2</sup>.

After going through the final design loop, the following design parameters are known:  $L$ ,  $\lambda_p$ ,  $\Delta\lambda_p$ . With this information we can calculate the delay between the signal and pump after their respective dispersive elements. Then this delay is added to the pump or signal so to synchronise them at the begin of the FWM process. We now have finished designing the set-up.

## 4.7 Implementation for bit patterns

For telecommunication networks with increasing bit-rates and shorter bit-lengths it is important to monitor the data channels for quality control. We show that the FWM time-lens oscilloscope can be used for this purpose. The time-lens oscilloscope may be implemented in two different configurations. In the first one, a signal train with multiple bits is covered by one large pump pulse. We call this the ‘multiple-bit shot’ configuration, see figure 4.19[a]. The second configuration which is shown in figure 4.19[b] is called ‘single-bit shot’ meaning that every bit has its own pump pulse. As an illustration, we explore how to design the multiple-bit shot configuration assuming a Gaussian ( $m=1, C=0$ ) signal and pump shape.

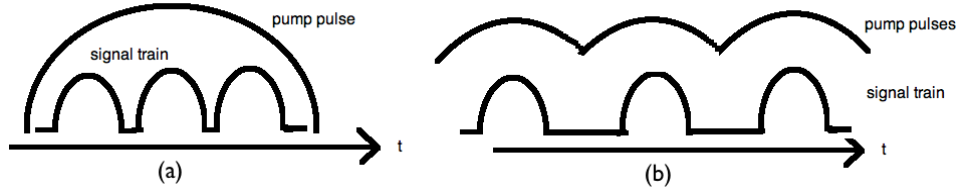


**Figure 4.19:** a. Multiple-bit shot configuration b. Single-bit shot configuration.

### 4.7.1 Multiple-bit shot

We do a numerical design for the monitoring of a 80 Gb/s data rate channel at 1550 nm. The time slot  $dt$  for each bit is 12.5 ps. The data pulses themselves are shorter and with a duty cycle of 33% we get that the initial FWHM pulse width  $\tau_0$  equals 4.2 ps. There are two main design conditions. The first one demands that the dispersed pump pulse should be broader than the dispersed pulse train. The second condition concerns the minimum resolution. The time oscilloscope should have a resolution which is much smaller than  $\tau_0$  which puts an upper limit on the initial pump width  $\tau_{p0}$ :

$$\tau_{res} = \frac{\tau_{p0}}{\sqrt{2}} \ll \tau_0. \quad (4.19)$$

We choose the resolution to be 420 fs which is a tenth of the initial bit width  $\tau_0$ . This leads to a initial pump width  $\tau_{p0}$  of  $420 \times \sqrt{2} = 593.96$  fs. The pump is a transform-limited Gaussian pulse so its spectral bandwidth  $\Delta\omega_p$  equals:  $0.44/\tau_{p0} \times 2\pi$ . Once the pump is known we must determine how broad it becomes after a certain distance  $L_p$  before TOD aberrations come into play. Once this distance  $L$  is determined, we calculate how many bits we can actually measure with this pump. For the 594 fs pump, the first heavily distorting TOD effects (e.g. oscillations) come into play after about 1600 m. Therefore we can choose  $L=L_p/2=800$  m. For Gaussian pulses the broadening after a distance  $L$  due to group velocity dispersion (GVD) and TOD can be determined via [9]:

$$\frac{\tau_{broadened}}{\tau_0} = \left[ 1 + \left( \frac{1.665^2 \beta_2 L}{\tau_0^2} \right)^2 + \frac{1}{2} \left( \frac{1.665^3 \sqrt{2} \beta_3 L}{2 \tau_0^3} \right)^2 \right]^{1/2}. \quad (4.20)$$

The pump is broadened to a FWHM of 828 ps after 1600 m of DCF. An individual signal pulse broadens up to 59 ps after 800 m. Therefore in principle we can measure 15 bits.

The flatness of the pump plays an important role, as it modulates the amplitude of the idler spectrum. This reduces the number of bits which will be accurately reproduced. As a proof-of-concept, we did a simulation of a pump which covers 8 bits in one shot of 472 ps. The result is shown in figure 4.20 the idler reflects the 8 Gaussian bits clearly, but the width of the generated idler is 4 ps too small. Further investigation is needed to increase this value. For

this simulation we didn't have to take into walk-off effects as we were using the chalcogenide chip. The pump was clearly flat enough as amplitude modulation of the idler is negligible.

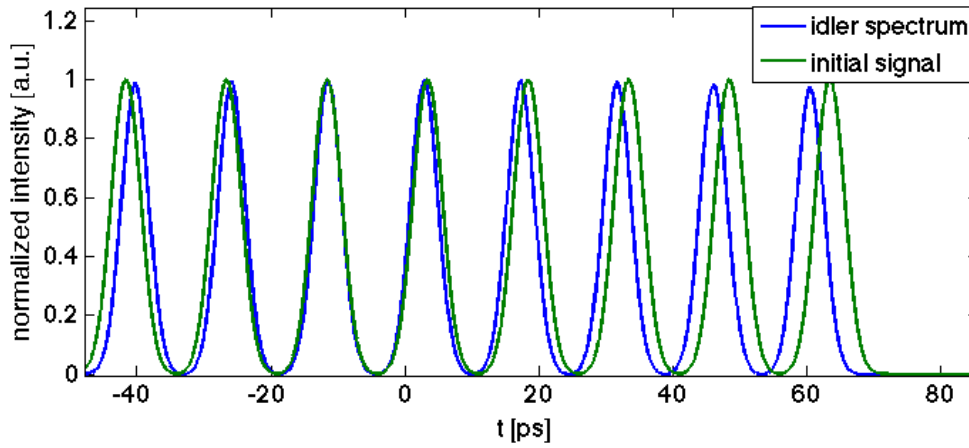


**Figure 4.20:** Frequency-to-time converted idler spectrum reflecting the 8-bit pulse train of a 80 Gb/s channel.

To show the advantage of the time-lens oscilloscope over the alternatives like FROG and optical sampling 3.3, we implement a variation in the amplitude of the 8-bit pulse train and leave all other simulation parameters unchanged. The result is shown in figure 4.21. Except from the unwanted difference in width, the idler spectrum resembles the input pulse perfectly.

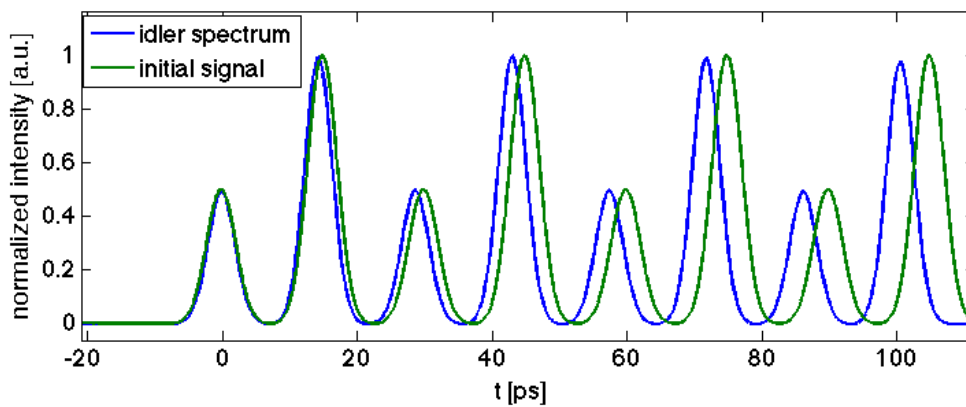


**Figure 4.21:** Frequency-to-time converted idler spectrum reflecting the amplitude modulated 8-bit pulse train of a 80 Gb/s channel.



## 4.8 Optimization of the FWM set-up with use Waveshaper® equipment

In this section we make clear why and how we can optimize the previous discussed FWM time-lens set-up. The main problem with the proposed FWM time-lens implementation is the use of dispersive fiber as the dispersive element. Optical fiber inherently exhibits third order dispersion which causes aberrations. Furthermore, we have seen in section 4.3.2 how important the Fourier transform condition is in terms of aberrations. We again repeat the Fourier transform condition:

$$D_p = 2 D_s \text{ or } \beta_2(\lambda_p) L_p = 2 \beta_2(\lambda_s) L_s$$

It means that for every different combination of  $\lambda_p$  and  $\lambda_s$  one should change  $L_p$  and  $L_s$  if one wants to exactly obey the Fourier transform condition, which is obviously unpractical. When the pump and signal pulses become shorter their broad spectrum necessitates a broad spreading of  $\lambda_p$  and  $\lambda_s$ . Therefore  $\beta_2(\lambda_p)$  will considerably differ of  $\beta_2(\lambda_s)$  even for DCF. Using dispersive fiber thus makes it difficult to obey the Fourier transform condition, hence new aberrations on top of the TOD aberrations are generated.

As a solution to these two issues we propose a new dispersive element, namely the Waveshaper®. The Waveshaper® is a reconfigurable pulse shaper that can shape a pulse in amplitude and phase. It is especially the phase shaping ability which we will exploit in the rest of this thesis work. The proposed set-up is shown in figure 4.22. The silicon chip is replaced by a chalcogenide chip which has the same functionalities but better overall performance.

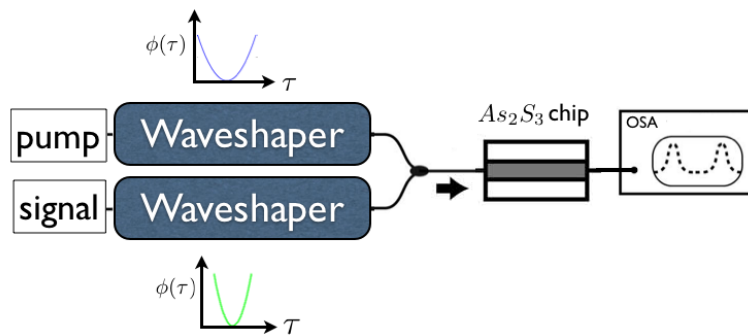


**Figure 4.22:** Waveshaper® set-up for optimal performance of the time-lens oscilloscope.

Second order dispersion manifests itself as a linear frequency chirp or in other words in generating a parabolic phase. So if the Waveshaper® imposes a parabolic phase onto the signal we get the equivalent of purely second order dispersion. The Waveshaper® is programmable

hence we can choose the slope of the imposed parabolic phase which is a measure for the total amount of dispersion  $D_T$  [ps/nm] which is added to the signal. So this solution completely removes the source TOD aberrations!

Moreover if we use the Waveshaper<sup>®</sup> to add  $D_s$  to the signal and  $2 D_s$  to the pump pulse, we can exactly obey the Fourier transform condition, removing the second source of aberrations. It is clear that it is a convenient and practical way to satisfy the Fourier transform condition.

The Waveshaper<sup>®</sup> equipment is limited though in the amount of dispersion  $D_T$  it can impose. As a result, we can still use the above described design strategy, but instead of having TOD constraints, we are restricted in  $D_T$ . This limitation in  $D_T$  leads to a fixed record length. In the next chapter we expand on this issue and give a complete description of the limitations of the device and how the optimal performance compares to the set-up which uses dispersive fiber as the dispersive element.

## 4.9 Conclusion

This chapter revealed the underlying complexity of the FWM time-lens set-up. We discussed all influencing parameters and developed a design strategy for the general case of Gaussian signal and pump pulses. The importance of a TOD-free dispersive element leads to our proposed set-up replacing the dispersive fiber with a reconfigurable pulse shaper. Furthermore the pulse shaper allows us to obey easily the Fourier transform condition, hence avoiding both TOD and 'non-ideal Fourier transform' aberrations. In the next chapter we design and simulate experiments for this new set-up.

## Chapter 5

# Design and simulation experiments with Waveshaper® set-up

### 5.1 Introduction

This chapter starts off with a review on the three basic components of the ideal time-lens set-up: the laser source, the Waveshaper® (or DWP) and the chalcogenide waveguide. In the experiments the time-lens is not implemented via FWM in the chalcogenide waveguide because for proof-of-principle experiments it is better to avoid the large insertion loss and polarization requirements of the chalcogenide waveguide. Therefore HNLF is the medium in which the time-lens action occurs in these experiments. Moreover we will show that the combination of the laser source and the Waveshaper® in the lab limits the available spectral bandwidth we can use for the signal and pump spectrum. In this case the pump & signal spectrum and the difference  $\lambda_s - \lambda_p$  are small, and the results in HNLF or chalcogenide chip turn out to be comparable. This is because the chip's main advantage, the large conversion bandwidth, is not exploited in this case. Hence this bandwidth limitation is a second reason to use HNLF for the experiments. This chapter shows the different steps in the design of the experiments. Moreover simulations of the different experimental set-ups are done so that we can compare with the experimental results in the following chapter. The final section of this chapter contains a discussion about the fundamental limitations of our time-lens set-up using the Waveshaper®.

### 5.2 Specific Equipment

For the experiments we use three quite specific components and therefore we give their main performance specifications and characteristics in this section before heading on to the exper-

imental set-up.

### 5.2.1 Erbium doped fiber laser

The laser which is used in the experiment was characterised by other researchers via FROG and OSA measurements. The spectrum of the laser covers a broad range from 1542 - 1583 nm as is shown in figure 5.1. The generated pulses are as short as 219 fs. The figure 5.1 also shows how the spectrum is affected by the Waveshapers® when no phase or amplitude shaping is applied. The change in spectrum shape is due to the nonlinear effects in the fiber in the Waveshapers®. Furthermore the Waveshapers® in the lab have an operation wavelength region from 1525 to 1572 nm. For the experiments we can thus only use the bandwidth region between 1542 and 1572 nm to shape the signals, which comes down to a total of 30 nm. The average power from the laser source is 11 dBm. After the first Waveshaper® the average power drops to 4.4 dBm and the second Waveshaper® reduces the average power to -4.6 dBm.

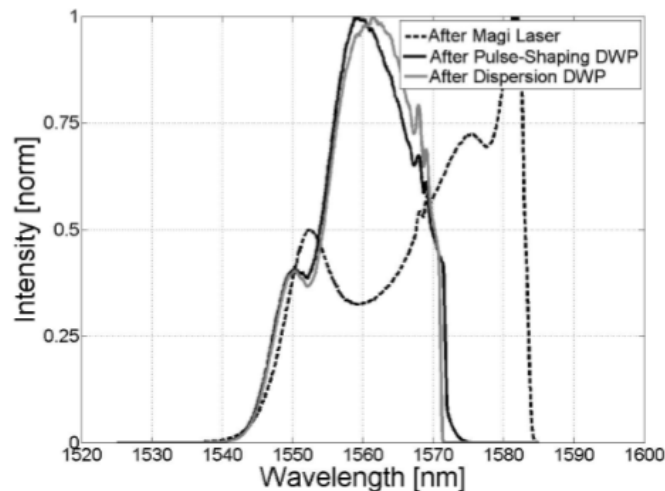


**Figure 5.1:** OSA Spectrum of the source Laser (Magi) directly following 1 m of SMF (dotted), then following the Waveshaper® used for pulse Shaping (black) and then following the Waveshaper® used for introducing dispersion (grey).

The information which is used to program the Waveshaper® is shown in figure 5.2. The initial phase and amplitude of the laser source must be known to do a correct shaping.

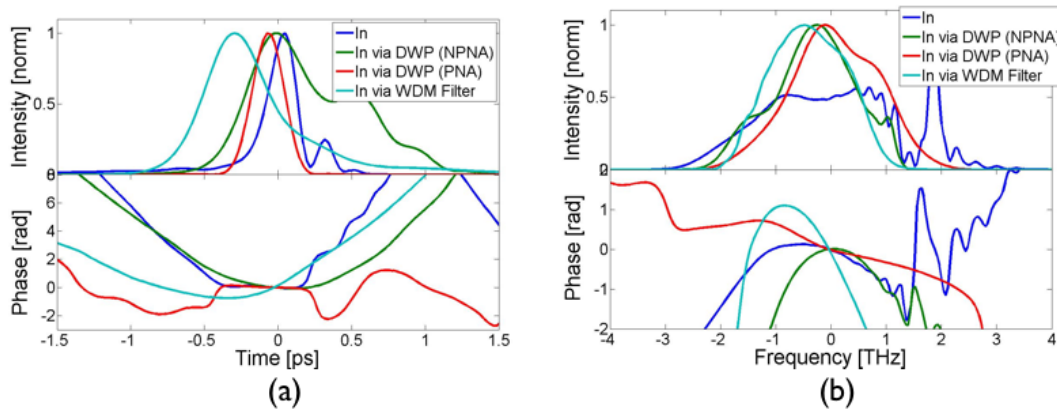


**Figure 5.2:** **a.** FROG measured temporal profiles of laser source directly, following the DWP without any phase or attenuation settings, following the DWP with phase compensation, and via a WDM filter **b.** FROG measured spectral profiles as outlined in (a).

### 5.2.2 Waveshaper<sup>®</sup>

The Waveshaper<sup>®</sup> is designed to function as a reconfigurable optical add/drop multiplexer (ROADM) but with extra features such as dispersion compensation or optical delay. It was developed in a cooperation between the company Finisar and the photonics department CUDOS at the university of Sydney. In figure 5.3 the interior of the device is shown.

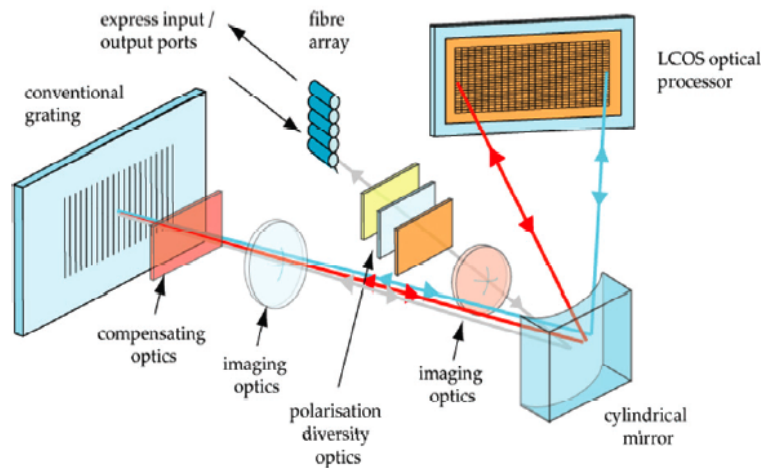


**Figure 5.3:** Waveshaper<sup>®</sup> set-up.

The most important component is the 2D liquid crystal on silicon (LCOS) array in which each pixel can change the phase of the incident light. By changing the phase pattern on the LCOS a pulse can be delayed, phase modulated, and amplitude modulated. The delay

is generated by sending the pulse to a different part of the grating so that in total its path length is increased before it leaves through one of the output ports. In more exact words as stated in [41]: “By sloping the phase front along the vertical axis, the signal is deflected to a desired output port, after the optical path is retraced upon reflection from the LCOS”. The grating sends the different frequencies to a different horizontal position and phase modulation is provided by varying the phase of the LCOS along this horizontal dimension. Pure second order dispersion is generated when a parabolic varying spectral phase is applied. It is this feature which makes the Waveshaper® ideal for the time-lens set-up. It is clear that the LCOS array is a phase-only modulator so amplitude modulation is obtained by “steering part of the light to dump locations within the device through advanced phase modulation of the phase front” [42].

Every pixel of the LCOS must be programmed in such a way that the pulse exhibits the correct phase and amplitude. This programming is based on the principle of fourier-domain pulse shaping which is schematically represented in figure 5.4:

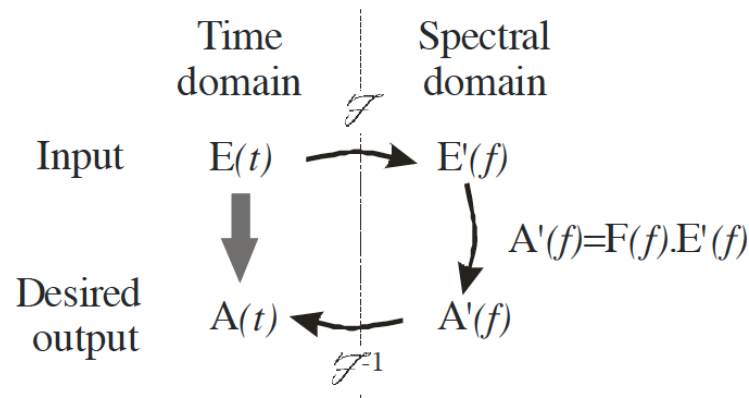


**Figure 5.4:** Schematic representation of fourier-domain pulse shaping [42].

The implementation has the following sequence:

First the fourier transform  $A'(f)$  of the desired temporal waveform is calculated. Secondly the fourier transform  $E(f)$  of the available input pulse is measured. A complex function  $F(f)$  can relate the two via:  $A'(f) = F(f) E(f)$ . This filter function is determined in phase and amplitude via  $F(f)=A'(f)/E(f)$ . In the final step the filter phase and amplitude get mapped into the corresponding voltage of the pixels on the LCOS.

The Waveshaper® in the lab holds the very important bandwidth-dispersion product:  $\Delta\lambda_{3dB} \times D = 40$  ps. It means that for a pulse with a spectral bandwidth of 1 nm a total dispersion  $D$  of  $\pm 40 \frac{ps}{nm}$  can be applied. A custom designed Waveshaper® can increase this bandwidth-

dispersion product up to 100 ps. A Waveshaper® has a limited range of wavelengths it can work with. The two Waveshapers® in the lab have an operation bandwidth in the C-band, going from 1525 to 1570 nm. Waveshapers® working in the L-band (1565 - 1625 nm) also exist.

### 5.2.3 Chalcogenide chip

The chalcogenide chip is a compact planar rib waveguide based on  $As_2S_3$  glass [40]. Figure 5.5 shows an example of a design:

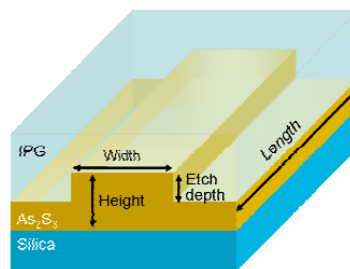


**Figure 5.5:** Structure of an  $As_2S_3$  ridge waveguide[38]

It is designed for optical signal processing making use of the ultrafast nonlinear phenomena originating from the third order susceptibility  $\chi^3$ . The chip provides a very high nonlinearity over a short length in the order of a few centimeters, which enhances SPM, XPM and FWM. The dispersion in the chip can be varied via a change in the waveguide dimensions, thereby changing the waveguide dispersion[38]. The applications of this chip are ubiquitous [[43],[44],[45]]. The characteristics of the chip are comparable to the silicon waveguide chips[46] like the one used in the third key experiment from chapter 3. But whereas the silicon chip suffers from free carrier effects and two-photon absorption (TPA) which reduces e.g. the FWM conversion bandwidth,  $As_2S_3$  is not as severely limited by these effects. Also TOD is larger in the silicon chip [38]. Some of the consequences are a higher amplification of the signal in FWM processes (important for e.g. signal regeneration) and a larger conversion bandwidth which allows for colourless operation in the chalcogenide chip. For the time-lens oscilloscope implementation the large conversion bandwidth is a great advantage because it means that we can use shorter signal and pump pulses, which increases the resolution and overall performance as we can measure shorter pulses.

## 5.3 Experiment with FWM in HNLF

### 5.3.1 Design experiment 1

The first experiment is a proof-of-principle to show that the signal pulse is indeed reflected in the idler spectrum. Therefore we choose a simple signal shape, namely a 1 ps Sech pulse. Its spectral bandwidth is about 2.5 nm. Furthermore we are not interested in maximalizing the record length as we will not scan through the pump pulse. Hence the choice  $D = 16$  ps/(nm km) and  $L = 50$  m doesn't fully exploit the possibilities of the Waveshaper<sup>®</sup>. As said before the combination of the laser source and the Waveshaper<sup>®</sup> limits the total spectral bandwidth that we can use to 30 nm. Both the signal and pump spectrum have to be shaped from of this amount. The first experiment uses 30 m of HNLF as the nonlinear medium for FWM and its zero dispersion wavelength (ZDW) is 1551 nm. To minimize walk-off effects we put the pump and signal on different sides of the ZDW.

The pump is a 1 ps Gaussian with a spectral width of about 3.5 nm. As the pump is initially equally broad as the signal we are guaranteed that the pump<sup>2</sup> will cover the total signal before the four-wave-mixing process starts. We have basically two major conditions: firstly we want to avoid spectral overlap between the signal and pump and secondly we want to keep the walk-off to an acceptable level. The following figures 5.6 are a detailed guideline for walk-off effects in the used HNLF of 30 m. The horizontal axis shows the different signal-pump spacings  $\Delta\lambda = \lambda_s - \lambda_p$ . The signal wavelength can vary between the ZDW (1551 nm) and 1570 nm. For all these possible positions of  $\lambda_s$  towards the ZDW we generated a curve to show the corresponding walk-off.

We first choose the center wavelength  $\lambda_p$  such that it is to the left of the ZDW but close to it, as the spectrum of the laser source doesn't allow us to fit a lot more than the 3dB bandwidth of the pump between 1545 nm and 1551 nm. Secondly we choose the center wavelength  $\lambda_s$  at a position such that the pulses only start to spectrally overlap at the -30dB intensity point. This gives the following choice of center wavelengths:  $\lambda_p = 1549$  nm and  $\lambda_s = 1562$  nm. We now check if the walk-off is acceptable for this choice. In the left bottom figure in figure 5.6 is indicated that our choice gives a walk-off of 50 fs. The signal pulse broadens after 50 m to 3.4 ps and the pump pulse stretches to about 5.7 ps after 100 m. Hence this value of 50 fs is negligible and walk-off will not impose any problems in the experiment.

### 5.3.2 Simulation experiment 1

We simulated the experiment with the above stated design. The idler wavelength is

$$\lambda_i = \frac{\lambda_s \lambda_p}{2 \lambda_s - \lambda_p} = \frac{1562 \times 1549}{2 \times 1562 - 1549} = 1536 \text{ nm} \quad (5.1)$$

The simulations shows accordingly a sech-shaped pulse at this wavelength 5.7:



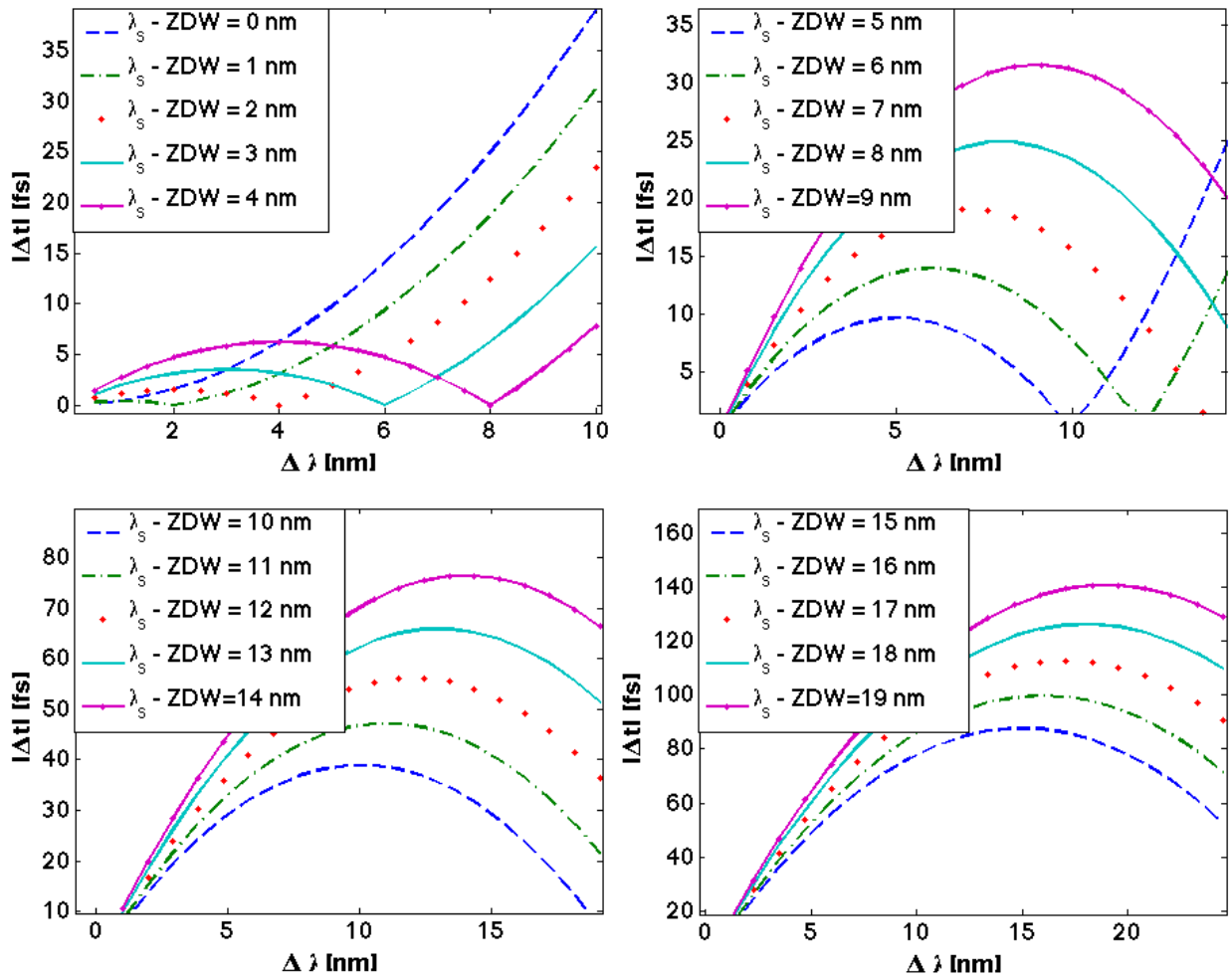


**Figure 5.6:** Walk-off for different  $\Delta \lambda = \lambda_s - \lambda_p$  and for different spacing of  $\lambda_s$  towards the zero dispersion wavelength at 1551 nm for 30 m of HNLF.

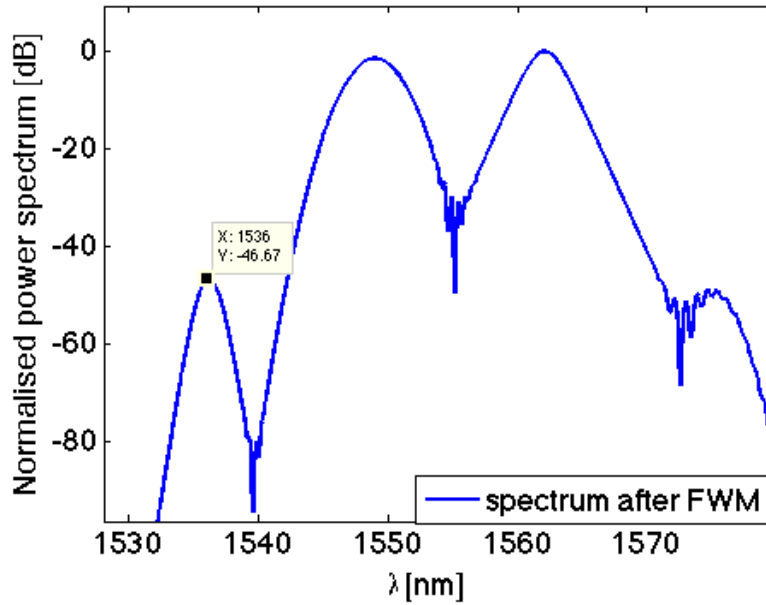


**Figure 5.7:** Spectrum after four-wave-mixing with signal at 1562 nm, pump pulse at 1549 nm and idler at 1536 nm.

The pump and signal spectrum start to interfere around -30dB which is in accordance with the proposed design. The resulting idler shape in linear scale is shown in figure 5.8

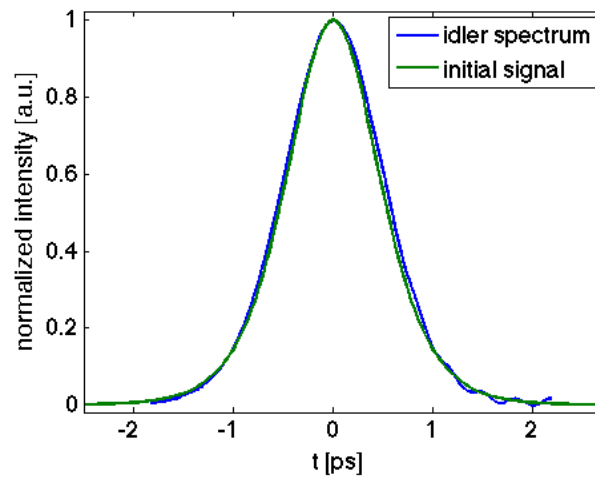


**Figure 5.8:** Simulated spectrum of the generated idler in the first experiment.

The FWHM spectral bandwidth of the idler is  $1537.057\text{nm} - 1535.505\text{nm} = 1.546\text{ nm}$  and with the time-to-frequency conversion factor formula in terms of  $\Delta\lambda$  and the dispersion  $D$  of

the DCF fiber we get:

$$\Delta t_{meas} = \left(\frac{\lambda_s}{\lambda_i}\right)^2 D L \Delta\lambda = 1.03 \times 16 \frac{ps}{nmkm} \times 0.050km \times 1.55nm = 1.27 \text{ ps}$$

The resolution is  $\tau_{pump}/\sqrt{2} = 1000 \text{ fs}/\sqrt{2} = 707.1fs$ , hence  $\tau_{act} = \sqrt{\tau_{meas}^2 - \tau_{res}^2} = 1.07 \text{ ps}$ , which is close to the simulated signal length of 1 ps. If we repeat the simulation with a shorter pump of 870 fs, which enhances the resolution. We place the pump and signal a bit further apart. We choose in this case:  $\lambda_s = 1564.5 \text{ nm}$  and  $\lambda_p = 1548 \text{ nm}$  so that  $\lambda_i = 1531.8 \text{ nm}$ . The simulations give the following results:

The FWHM spectral bandwidth of the idler is  $1532.87nm - 1531.39nm = 1.48 \text{ nm}$  and with the time-to-frequency conversion factor formula in terms of  $\Delta\lambda$  and the dispersion D of the DCF fiber we get:

$$\Delta t_{meas} = \left(\frac{\lambda_s}{\lambda_i}\right)^2 D L \Delta\lambda = 1.04 \times 16 \frac{ps}{nmkm} \times 0.050km \times 1.48nm = 1.23 \text{ ps}$$

So indeed the measured pulse width is closer to the simulated width of 1 ps. The resolution is  $\tau_{pump}/\sqrt{2} = 870 \text{ fs}/\sqrt{2} = 615.18fs$ , hence  $\tau_{act} = \sqrt{\tau_{meas}^2 - \tau_{res}^2} = 1.065 \text{ ps}$ , which is again close to the simulated signal length of 1 ps and slightly better than for previous parameters.

### 5.3.3 Design experiment 2

In the second experiment we want to transform a more complex signal. We choose an asymmetric shape described by:

$$A_{in} = \sqrt{P_0} \left[ e^{-(0.6t)^2} - 0.5 e^{-5(0.6t-0.06)^2} \right]. \quad (5.2)$$

Figure 5.9 shows the input signal and its associated spectrum.

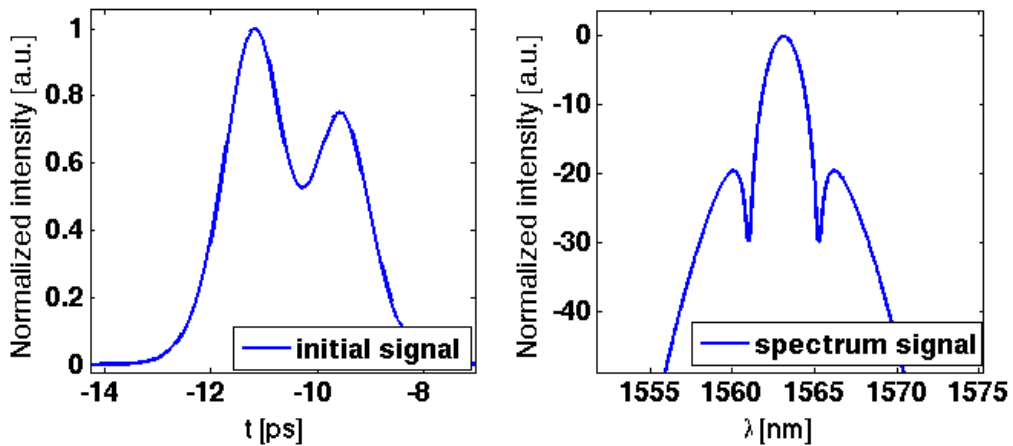


Figure 5.9: Input signal and spectrum for the second experiment.

Although the signal is relatively long, namely 4 ps, the spectrum is a wide 8 nm. Making the signal much shorter would cause us a shortage of bandwidth due to the afore-mentioned bandwidth constraints. As the signal needs a higher accuracy to be well represented by the idler, the pump pulse is a short 700 fs Gaussian pulse. The design strategy for the second experiment is closely related to the one of the previous experiment. We choose the pump wavelength  $\lambda_p$  to be 1548 nm. Because the pump is shorter its spectrum is broader (5 nm) and hence we should place  $\lambda_p$  a bit further to the left of ZDW compared to the previous experiment. The signal wavelength  $\lambda_s$  is determined via the same -30dB spectral intersection criterion. It results in  $\lambda_s = 1563$  nm. The walk-off for 30 m of HNLF is in this case 55 fs, which is negligible considering that the pump and signal are broadened to about 8 ps after their dispersive elements.

### 5.3.4 Simulation experiment 2

The idler wavelength is

$$\lambda_i = \frac{\lambda_s \lambda_p}{2 \lambda_s - \lambda_p} = \frac{1563 \times 1548}{2 \times 1563 - 1548} = 1533 \text{ nm} \quad (5.3)$$

The spectrum of the total field (pump + signal + idler) after the four-wave-mixing looks like figure 5.10

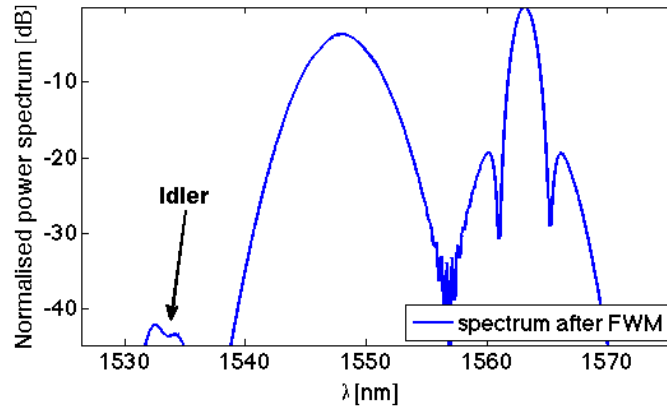


**Figure 5.10:** Spectrum after four-wave-mixing with signal at 1563 nm, pump pulse at 1548 nm and idler at 1533 nm.

The idler spectrum 5.11 doesn't reflect the incoming signal as well as in the previous experiment. The reason for this is the limited resolution. The resolution in this set-up is  $\tau_{pump}/\sqrt{2} = 700 \text{ fs}/\sqrt{2} = 495 \text{ fs}$ , while the dip in the signal shape is sharper than 500 fs. Therefore is the dip in the idler spectrum not as deep as in the initial signal shape.

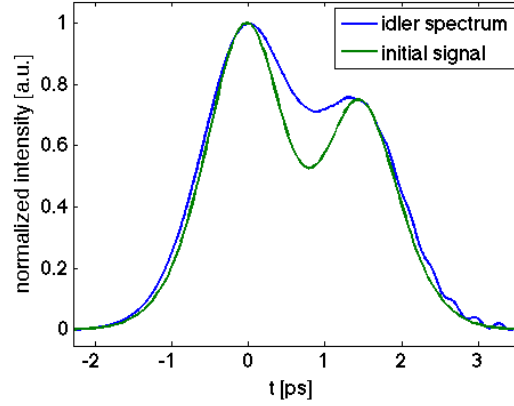


**Figure 5.11:** Simulated spectrum of the generated idler in the second experiment.

The relative height of the two peaks ( $=0.75$ ) is conserved during the transformation, which shows the success of the design and simulation.

## 5.4 Fundamental limitations of the Waveshaper<sup>®</sup> set-up

In this section we discuss the limitations to the performance of the Waveshaper<sup>®</sup> set-up. The first limitation comes from the fixed bandwidth-dispersion product  $\Delta\lambda_{3dB} \times D_T = 40\text{ps}$ . The pulse with the broadest spectral bandwidth (pump or signal) determines the maximum  $D_T$  for the given bandwidth-dispersion product. If we rewrite the expression for  $\tau_{rec}$  (which holds for  $\Delta\lambda_p > \Delta\lambda_s$ ) we can easily see that the bandwidth-dispersion product is equivalent to the record length:

$$\tau_{rec} = 2 D L \Delta\lambda_p = D_T \Delta\lambda_p = 40\text{ps} \quad (5.4)$$

As said before, a custom made Waveshaper<sup>®</sup> can increase the bandwidth-dispersion product up to maximally 100 ps, which gives  $\tau_{rec} = 100\text{ps}$ . The second limitation is the compactness of the set-up. The Waveshaper<sup>®</sup> devices are a lot bigger than two spools of optical fiber and definitely not integratable.

We now investigate what the highest possible resolution is for this set-up. Essentially it is the bandwidth of the Waveshaper<sup>®</sup> that determines the maximum resolution. Assume a transform-limited Gaussian signal at  $\lambda_s = 1550$  nm, shaped by a Waveshaper<sup>®</sup> with an operation region from 1525 nm to 1570 nm. A transform-limited Gaussian pump pulse is at  $\lambda_p = 1592.5$  nm and is shaped by a Waveshaper<sup>®</sup> with an operation region from 1570 nm to 1615 nm. The pump has a maximal bandwidth of  $\Delta\lambda_p = 45$  nm, which equals the operation region of the Waveshaper<sup>®</sup>. Hence its duration  $\tau_p$  is  $\frac{0.44 \lambda_p^2}{c \Delta\lambda_p} = 83$  fs. The shortest signal

possible has a duration equal to the highest resolution  $\tau_s = \tau_{res} = \frac{\tau_p}{\sqrt{2}} = 58.45\text{fs}$ , which leads to  $\Delta\lambda_s = 60.3\text{ nm}$ . This is too broad for a Waveshaper<sup>®</sup> to work with so we have to limit the signal to  $\Delta\lambda_s = 45\text{ nm}$ , ending up with a shortest signal of  $\frac{0.44\lambda_s^2}{c\Delta\lambda_s} = 78\text{ fs}$ . The associated minimum dispersion to make the set-up work is  $D_{s,min} = (t_s/1.665)^2 \frac{2\pi c}{\lambda_s^2} = 0.0017[\text{ps/nm}]$ . The bandwidth-dispersion product equals  $D_{s,min} \Delta\lambda_s = 0.329\text{ ps}$ , which is well below the limit of 100 ps. Increasing the dispersion  $D_s$  the signal sees, decreases the generated idler bandwidth.

The longest signal that can be measured with the highest resolution of 78 fs is different from the record length, as the record length doesn't take into account that the input signal must see a minimum dispersion  $D_{min} = (\frac{\tau_s}{1.665})^2 \frac{2\pi c}{\lambda_s^2}$  before the set-up works 4.3.1. We can easily calculate the longest signal duration. The maximum dispersion that can be imposed on the pump is  $D_{p,max} = \frac{100\text{ps}}{45\text{nm}} = 2.2\text{ [ps/nm]}$ . The signal sees half of this dispersion, hence  $D_s = 1.11\text{ [ps/nm]}$ . The signal dispersion must obey  $D_s \geq D_{min} = (\frac{\tau_s}{1.665})^2 \frac{2\pi c}{\lambda_s^2}$  from which we determine that  $\tau_s = 62.6\text{ ps}$  for a signal at 1550 nm.

## 5.5 Conclusion

In this chapter we discussed the key components in the experimental set-up. The available spectral bandwidth of the laser cannot be fully used as the wave-shaper has a limited operation region. Keeping this constraint in mind, we designed and simulated simulated two different set-ups in which the time-lens was implemented via FWM in HNLF. The pump and signal are shaped in amplitude and phase via the Waveshaper<sup>®</sup> equipment which constitutes a reconfigurable temporal imaging system with a very low amount of aberration compared to the FWM time-lens set-up from reference [1]. The positive simulation results indicate that the experiments will be successful. To end this chapter, we explored the fundamental limitations of our proposed set-up. The record length is limited to 100 ps when using a custom made Waveshaper<sup>®</sup> and the best achievable resolution is 78 fs. The longest signal, at the telecom wavelength of 1550 nm, that can be measured with this accuracy is 62.6 ps long. In the following chapter we present the results obtained from our designed experiments and compare them with the simulations from this chapter.

## Chapter 6

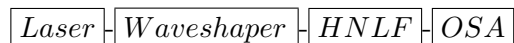
# Experimental results

### 6.1 Introduction

### 6.2 Experiment in HNLF

#### 6.2.1 Experiment I: 1ps Sech input pulse

The first experimental set-up is very simple and requires no optimization components such as polarizers or optical delay lines. The laser source is connected with a Waveshaper<sup>®</sup> which shapes the signal and pump pulse in amplitude and applies the correct phase (equivalent to purely second order dispersive element) after which the generated pump and signal pulse are coupled into 30 m of HNLF. The output of the HNLF is connected to an OSA. So the set-up looks as follows:



The signal and pump have a center wavelength of 1562 nm and 1549 nm respectively. During the experiment no amplifiers are used, instead both pulses are attenuated in the Waveshaper<sup>®</sup> before they are sent into the HNLF. The average power before they pulses are sent into the HNLF is -17.67 dB for the signal and -11.72 dB for the pump so to avoid other nonlinear effects like SPM which distort the idler signal. The Waveshaper<sup>®</sup> creates two 1 ps pulses, the signal has a Sech shape and the pump is a Gaussian. A FROG measurement shows the profiles of the signal and pump pulse before they are sent into the HNLF.

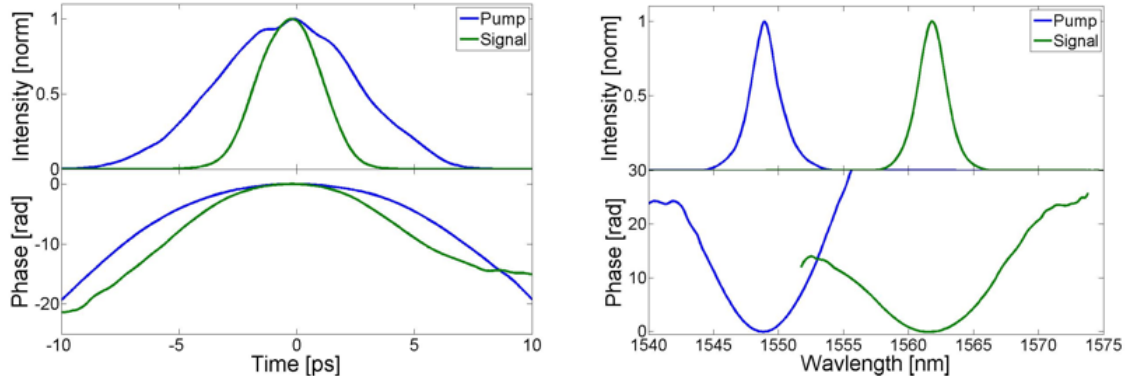


**Figure 6.1:** Pump and signal temporal and spectral profiles with a dispersion  $D$  of 16 ps/nm/km for  $L=50$  m (signal) and  $L=100$  m (pump).

The pump pulse is slightly distorted in the time domain around  $t=0$  ps, but has a quasi-perfect quadratic phase. The distortion is because an erbium doped fiber amplifier (EDFA) was used to measure the pump pulse as a FROG measurement requires high peak power. The EDFA doesn't work optimal for low repetition rate signals. The signal pulse has a good temporal shape but its phase deviates from a perfect parabola around  $t=7$  ps. This deviation is not important for us because the pulse amplitude is zero at this point. This being zero of the pulse is a source of numerical inaccuracies leading to the deviation in phase.

The figure 6.1 is used to calculate the slope of the phase curve around the center of the pulses, from which we retrieve that for the signal:

$$\frac{d\phi}{d\tau} = -4.6733 \tau - 1.2042 \Rightarrow S_s = -4.6733,$$

and for the pump:

$$\frac{d\phi}{d\tau} = -2.2143 \tau + 0.2294 \Rightarrow S_p = -2.2143.$$

Theoretically the slopes  $S_s$  and  $S_p$  are the following:  $S_s = \frac{1}{D_s}$  and  $S_p = \frac{1}{D_p}$  in which  $D_s$  and  $D_p$  is the total dispersion on the signal and pump respectively. The ratio of the slopes is thus

$$\frac{S_p}{S_s} = \frac{\frac{1}{D_p}}{\frac{1}{D_s}} = \frac{D_s}{2 D_p} = \frac{1}{2}. \quad (6.1)$$

For the created pulse and signal we get a ratio of

$$\frac{S_p}{S_s} = \frac{-2.2143}{-4.6733} = 0.4738 \approx 0.5.$$



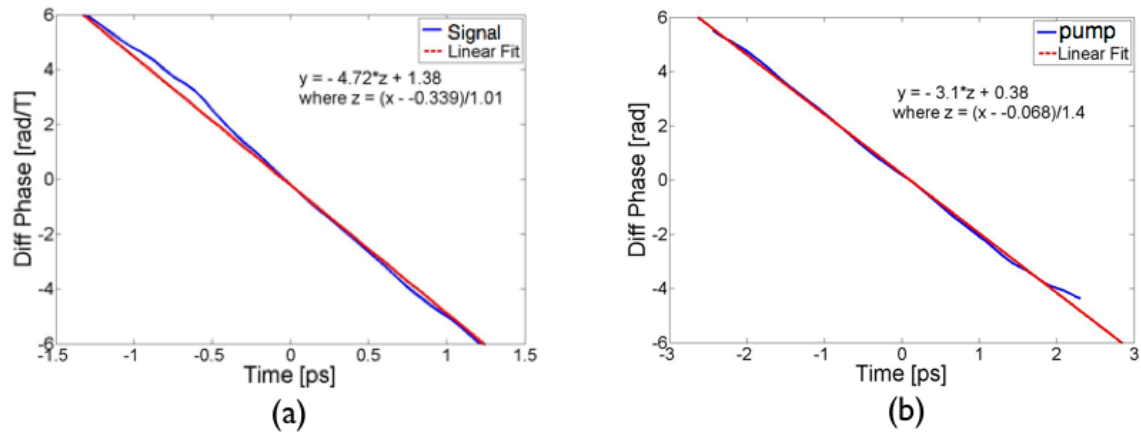


**Figure 6.2:** a. First derivative of the phase of the signal b. First derivative of the phase of the pump.

This proves that we obey the Fourier transform condition for the most important part of the pulses.

The experimental result is shown in figure 6.3:

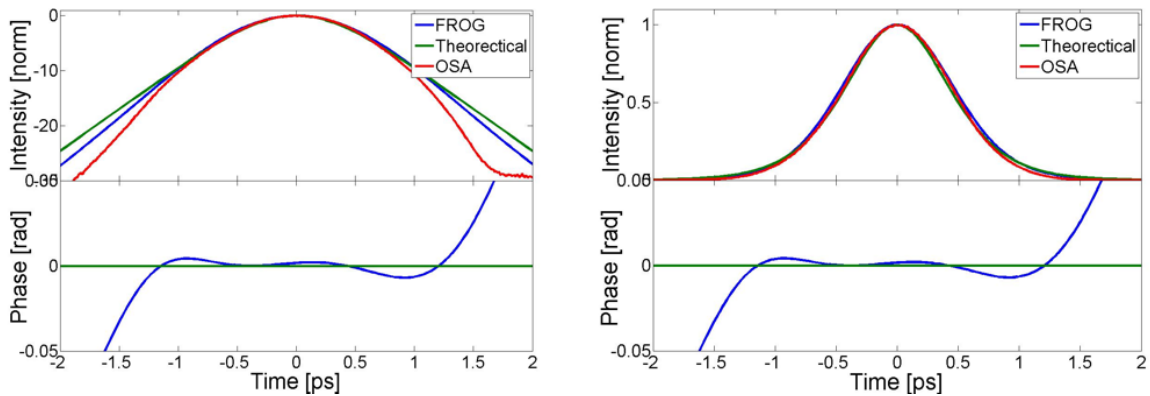
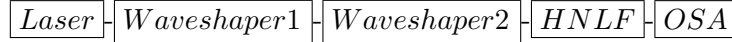


**Figure 6.3:** Comparison of the FROG and time lens oscilloscope measurement (OSA) of a 1 ps transform limited Sech pulse (theoretical).

As a first experiment this is very promising as we can clearly see how well the idler profile matches with the theoretical Sech pulse profile over a range of more than 10 dB and giving a similar performance as the FROG-measurement (blue curve). The fact that the phase is close to zero over the whole pulse indicates that the generated initial pump and signal pulses are transform limited. The experimental result is also in accordance with the simulation 5.3.1.

We perform a similar experiment by using the following set-up:



The pump is a 870 fs Gaussian at 1548 nm and the signal is a 1 ps Sech at 1564.5 nm. We thus shorten the pump to achieve a better resolution  $\tau_{res} = \frac{870fs}{\sqrt{2}} = 615.2$  fs. The first Waveshaper<sup>®</sup> shapes the signal and pump in amplitude and the second Waveshaper<sup>®</sup> imposes the correct phase. The new set-up allows us to measure the shape of the signal after the first Waveshaper<sup>®</sup> via a FROG measurement. This is the signal shape we should compare our idler spectrum with, as this is the signal which is the real input of our time-lens set-up. Spreading the shaping of the amplitude and phase over two Waveshapers<sup>®</sup> yields good results as shown in figure 6.4:

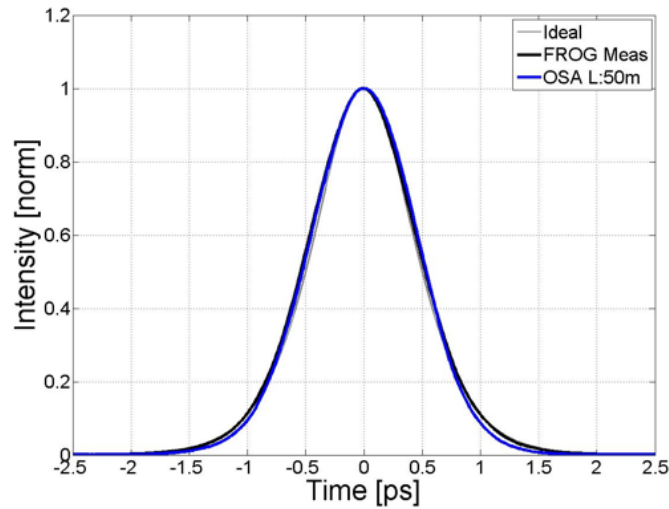


**Figure 6.4:** Result of experiment 1 in the new set-up: the idler (blue) is a perfect reproduction of the input signal which is represented by the FROG trace (black).

The experimental idler has a measured width of  $\tau_{meas}^2 = 122$  fs (measured with FROG), which is equivalent with an actual width of  $\tau_{act} = \sqrt{\tau_{meas}^2 - \tau_{res}^2} = 1.054$  ps. This results shows a very good correspondence between the simulation ( $\tau_{act} = 1.065ps$ ) and experiment.

## 6.2.2 Experiment II: Asymmetric pulse

The experiment as described in section 5.3.4 was unsuccessful as we didn't manage to shape the signal in amplitude as good as we wanted. We must stress though that in the ideal Waveshaper<sup>®</sup> set-up, the signal is not shaped in amplitude by a Waveshaper<sup>®</sup>. So the failure of this experiment doesn't mean that the experiment wouldn't work with this type of input pulse.

We took another approach to generate a similar signal by simulating the sum of two 0.5 ps

Gaussian pulses separated by 2 ps. The parameters are the following:  $\lambda_s = 1564.5\text{nm}$ ,  $\lambda_p = 1548\text{nm}$ ,  $D_{\text{signal}} = 0.15[\text{km}] \times 16[\frac{\text{ps}}{\text{km nm}}]$  and  $D_{\text{idler}} = 0.3[\text{km}] \times 16[\frac{\text{ps}}{\text{km nm}}]$ . The result is shown in figure 6.5.

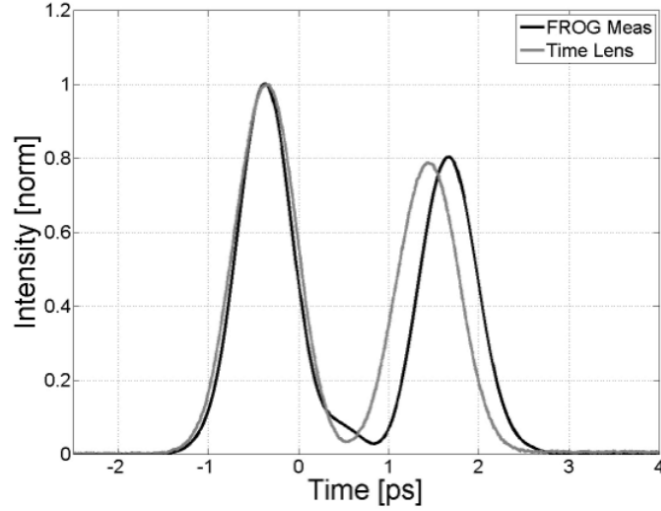


**Figure 6.5:** Generated input signal by the Waveshaper<sup>®</sup> (black) and resulting idler signal (light grey)

The simulation predicted the conservation of height and indeed the height information is conserved, which shows the success of the transformation. But, similar to the simulation of the 8-bit pulse train 4.7.1, the time-lens trace is shorter than wanted. Further research should show the (theoretical) reason for this and then we can incorporate a compensation for it.

### 6.2.3 Experiment III: Pulse burst

This experiment shows the measurement of a pulse burst of four 1 ps Gaussian pulses with 6.25 ps separation, which is generated by spectral filtering the 38 MHz modelocked source [47]. The signal has a center wavelength of  $\lambda_s = 1564.5\text{ nm}$  and the pump is a 870 fs Gaussian with center wavelength at  $\lambda_p = 1548\text{ nm}$ . The applied dispersions are the following:  $D_{\text{signal}} = 0.15[\text{km}] \times 16[\frac{\text{ps}}{\text{km nm}}]$  and  $D_{\text{idler}} = 0.3[\text{km}] \times 16[\frac{\text{ps}}{\text{km nm}}]$ . The results are shown in figure 6.6. As can be seen each pulse in the pulse-burst (black) does not have equal amplitude. We are confident that the amplitudes of the pulses in the pulse burst are varying, however due to the complex spectral structure of the pulse burst and the limited resolution of the FROG, the retrieval algorithm finds it difficult to achieve accurate matching between the measured spectrogram and the retrieved spectrogram, and thus does not give accurate amplitude information. Therefore a different independent measurement system is required (required future work) to verify the varying amplitudes of the input pulse burst. However this

figure gives us an indication that our time lens oscilloscope has the capability to measure a pulse train accurately and gives amplitude information that can otherwise be lost in sampling oscilloscope measurement techniques for example. Again the idler width is smaller than wanted.

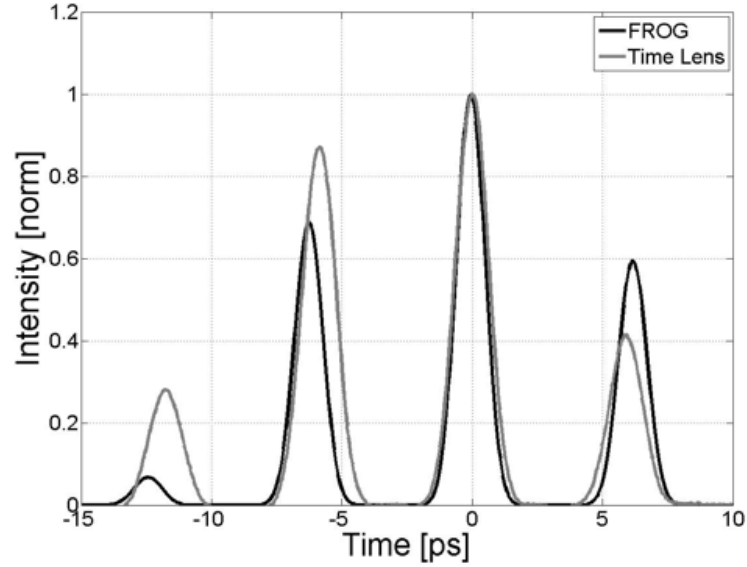


**Figure 6.6:** Input signal as shown by a FROG measurement (black) and the frequency-to-time converted idler spectrum (grey).

#### 6.2.4 Experiment IV: Sensitivity to the Fourier transform condition

As shown in section 4.3.2, aberrations originate when we deviate from the exact Fourier transform condition 3.8. The experimental results in figure 6.7 show the measurement of a 1 ps Sech signal at 1564.5 nm, using a 870 fs Gaussian pump at 1548 nm, while deviating from the Fourier transform condition. Again we set  $D_{signal} = 0.15[km] \times 16[\frac{ps}{km\ nm}]$  and  $D_{signal} = 0.3[km] \times 16[\frac{ps}{km\ nm}]$ . When we don't obey the Fourier transform condition exactly, the ratio of the (time) phase slope of the pump and signal 6.1, deviates from the ideal value 0.5. As expected the aberrations grow worse with increasing deviation from the ideal slope ratio of 0.5 .

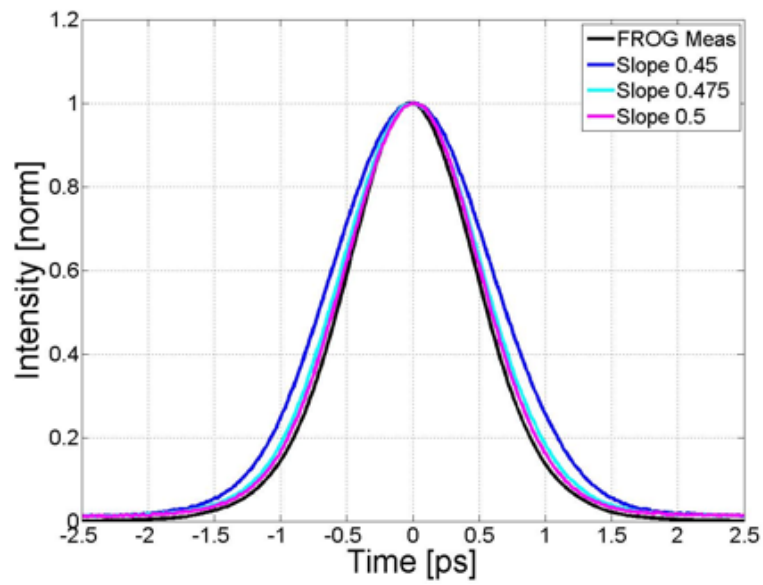


**Figure 6.7:** Aberrations arise for the measurement of the input 1 ps Sech pulse (black) for a variation in the slope ratio which is ideally 0.5 .

## Chapter 7

# Conclusions and future directions

In this thesis work we demonstrated how we can use a temporal imaging set-up, working in the Fourier transform regime, to measure the waveform of signals with sub-picosecond accuracy. We did a detailed investigation of the specific FWM time-lens set-up as reported in [1] which uses dispersive fiber as the dispersive element and a silicon chip as the nonlinear medium for FWM. We have discussed all design parameters via simulations in Matlab<sup>®</sup> and derived the key steps of the design process of a time-lens oscilloscope. The results of the investigation show that one needs an alternative to the dispersive fibers to reduce aberrations caused by third-order dispersion, which is unavoidable in optical fiber. Furthermore, more flexibility is required to satisfy the Fourier-transform condition more exactly. Deviation from the Fourier-transform condition is an additional source of unwanted aberrations. Therefore we proposed a new reconfigurable set-up using a Waveshaper<sup>®</sup> as the dispersive element. The Waveshaper<sup>®</sup> facilitates the imposition of purely second order dispersion and satisfies the Fourier-transform more flexibly, so that aberrations are drastically reduced.

In the ideal case, the proposed set-up uses two Waveshapers<sup>®</sup> and a chalcogenide chip for FWM. The fundamental limits of this set-up were determined and theoretically overall performance can compete the results presented in [1]. The maximum resolution of 78 fs over a record length of 100 ps offers a much better theoretical record-length-to-resolution ratio of 1280 versus the reported 450. Future implementation of the ideal set-up is needed to verify its actual performance.

Due to bandwidth constraints, the ideal set-up was not yet implemented during this thesis project. The combination of the laser source and available Waveshapers<sup>®</sup> restricted the bandwidth we could allocate to the signal and pump spectrum. As a result, the signal and pump spectrum were relatively narrow and positioned close to each other. Therefore we

couldn't justify the use of the dispersion-engineered chalcogenide chip, which suffers high insertion losses, over HNLFF as the nonlinear medium for FWM. The bandwidth constraint is alleviated by using a separate signal source and two Waveshapers® working in a separate wavelength range (L and C band). Using a separate signal and pump source does require an efficient solution to synchronise the signal and pump pulses just before the nonlinear medium.

Two experiments were designed and simulated using FWM in HNLFF, taking into account the given bandwidth constraint and to serve as a proof-of-concept. We demonstrate that the Waveshaper® can indeed be used to create a more flexible time-lens architecture with reduced aberrations. The experimental results show the successful measurement of a 1 ps Sech input signal with femtosecond accuracy, in agreement with the simulations. The measurement of more complicated input signals indicated that the time-lens is capable of measuring amplitude variations with high accuracy.

Although the influence of most of the design parameters have been characterised in this thesis work, further (theoretical) research is needed. We didn't look closely into the dynamic range of the set-up and how the FWM conversion efficiency/bandwidth affects the generated idler bandwidth. Both would indicate how using the chalcogenide chip influences the performance of the set-up. More experiments should be designed to put the ideal set-up to the test, especially to assess its capability in measuring amplitude-varying signal trains. This would clearly prove the advantage of the time-lens oscilloscope over alternative measurement schemes such as FROG and optical sampling.

# Appendix A

## A.1 Phase function thin lens

A thin lens acts as a phase transformer. Because the lens has a different refractive index  $n$  than the surrounding air ( $n_{air} = 1$ ), the phase shift the light gets during transit, depends on the time spent in the lens. We consider a thin lens so that a light ray propagating in the  $z$ -direction which enters the lens at a transverse position  $(x,y)$ , leaves the lens at the same transverse position. The resulting phase shift for each transverse position  $(x,y)$  is given by:

$$\phi(x, y) = k n \Delta(x, y) + k [\Delta_0 - \Delta(x, y)] = k \Delta_0 + k (n - 1) \Delta(x, y) \quad (\text{A.1})$$

The parameter  $\Delta$  is the thickness of the lens measured along the  $z$ -axis. In the first equality, the first term describes the phase shift due to traveling through the lens and the second term accounts for the phase shift in air.

We use the scalar theory of light so we consider a single component of the electric or magnetic field vector, which we represent by  $U(\mathbf{r})$ . We can relate the field  $U_{in}(x, y)$  at the input of the lens with the output field  $U_{out}(x, y)$  of the lens via the transfer function  $t(x,y)$  which expresses a position-dependent phase shift:

$$U_{out}(x, y) = t(x, y) U_{in}(x, y) = e^{-i\phi(x,y)} U_{in}(x, y) \quad (\text{A.2})$$

With the use of the paraxial approximation it is possible to find an expression for the thickness of the lens in function of its shape. We can write [11]:

$$\Delta(x, y) = \Delta_0 - \frac{x^2+y^2}{2} \left( \frac{1}{R_1} - \frac{1}{R_2} \right)$$

in which  $R_1$  is the radius of curvature of the input surface of the lens and  $R_2$  is the radius of curvature of the output surface of the lens.

After defining the focal distance of a thin lens  $f$  as:



$$\frac{1}{f} = (n - 1) \left( \frac{1}{R_1} - \frac{1}{R_2} \right)$$

we end up with the final form of the transfer function  $t(x,y)$  which describes the thin-lens action

$$t(x, y) = e^{-ikn\Delta_0} e^{\frac{ik}{2f}(x^2+y^2)} \quad (\text{A.3})$$

## A.2 Impulse response temporal imaging system

We consider the imaging system as a linear system and consequently write:

$$A(z, \tau) = \int_{-\infty}^{\infty} h(\tau; \tau_0) A(0, \tau_0) d\tau_0 \quad (\text{A.4})$$

where  $h(\tau; \tau_0)$  is the response of the system at time  $\tau$  after insertion of a delta-impulse applied at  $\tau_0$ . The input waveform  $A(0, \tau) = \delta(\tau - \tau_0)$  serves as a weighting function. The first step in the imaging setup is the input dispersion and the field after the dispersive element with length  $L_1$  is:

$$A(L_1, \tau) = G1(L_1, \tau) * \delta(\tau - \tau_0) = G1(L_1, \tau - \tau_0) \quad (\text{A.5})$$

The lens has a finite aperture time and if we introduce a pupil function  $P(\tau)$ , we can write its transmittance as  $P(\tau) H(\tau)$ . After the lens the field is (in the time domain):

$$A(L_1 + \epsilon, \tau) = G1(L_1, \tau - \tau_0) P(\tau) H(\tau) \quad (\text{A.6})$$

After the output dispersive element with length  $L_2$ , the impulse response results in:

$$h(\tau; \tau_0) = G1(L_1, \tau - \tau_0) H(\tau) P(\tau) * G2(L_2, \tau) \quad (\text{A.7})$$

We first expand the convolution in this expression:

$$h(\tau; \tau_0) = \int_{-\infty}^{\infty} G1(L_1, \tau' - \tau_0) H(\tau') P(\tau') G2(L_2, \tau - \tau') d\tau' \quad (\text{A.8})$$

Now we insert the transfer functions as found in figure 2.7:

$$h(\tau; \tau_0) = \frac{1}{4\pi i \sqrt{ab}} \int_{-\infty}^{\infty} P(\tau') e^{i \frac{(\tau' - \tau_0)^2}{4a}} \cdot e^{i \frac{(\tau - \tau')^2}{4b}} \cdot e^{i \frac{\tau'^2}{4c}} d\tau' \quad (\text{A.9})$$

The terms in  $\tau$  are now put outside the integral and we combine the exponential terms in  $\tau'$  and  $\tau'^2$  which results in:

$$h(\tau; \tau_0) = \frac{1}{4\pi i \sqrt{ab}} e^{i \frac{(\tau_0^2/a + \tau^2/b)}{4}} \int_{-\infty}^{\infty} P(\tau') e^{\frac{i\tau'^2}{4} (1/a + 1/b + 1/c)} e^{\frac{-i\tau'}{2} (\tau_0/a - \tau/b)} d\tau' \quad (\text{A.10})$$

This is the final shape of the impulse response and by choosing the right combination of the parameters a,b,c we end up either in the magnifying regime either the fourier-transfer regime.

### A.3 Magnification regime

We now show how stretching of a pulse can be established if the so-called temporal imaging condition is obeyed. We start with considering an input pulse with envelope  $A(z, \tau)$  and spectrum  $A(z, \Omega)$  which at the end of the input dispersion looks like:

$$A(L_1, \tau) = F^{-1} A(0, \Omega) G1(L_1, \Omega) \quad (\text{A.11})$$

Sending this pulse through the lens results in:

$$A(L_1 + \epsilon, \tau) = F^{-1} A(0, \Omega) G1(L_1, \Omega) H(\tau) \quad (\text{A.12})$$

Finally after the output dispersion the envelope is:

$$A(L_2, \tau) = \frac{1}{2\pi} F^{-1} [(A(0, \Omega) G1(L_1, \Omega)) * H(\Omega)] \cdot G2(L_2, \Omega) \quad (\text{A.13})$$

Inserting the correct expressions for the various transfer functions 2.7 results in:

$$A(L_2, \tau) = \sqrt{\frac{c}{b+c}} e^{\frac{i\tau^2}{4(b+c)}} \frac{1}{2\pi} \int_{-\infty}^{\infty} A(0, \Omega) \cdot e^{-i(1/a+1/b+1/c)\Omega^2} \cdot e^{i(\frac{c}{b+c})\tau\Omega'} d\Omega' \quad (\text{A.14})$$

If the sum  $1/a+1/b+1/c$  equals zero the quadratic phase in  $\Omega'$  is removed and we end up with

$$A(L_2, \tau) = \sqrt{\frac{c}{b+c}} e^{\frac{i\tau^2}{4(b+c)}} \frac{1}{2\pi} \int_{-\infty}^{\infty} A(0, \Omega) \cdot e^{i(\frac{c}{b+c})\tau\Omega'} d\Omega' \quad (\text{A.15})$$

which is a Fourier transform with a scaled time  $\tau' = \tau \cdot \frac{c}{b+c} = \frac{\tau}{M}$  if we define M as follows:

$$M \equiv \frac{b+c}{c}$$

The magnifying power of the system is shown by the result of the Fourier transform:

$$\boxed{A(L_2, \tau) = \frac{1}{2\pi\sqrt{M}} e^{\frac{i\omega_0\tau^2}{2MfT}} A(0, \tau/M)} \quad (\text{A.16})$$

The above equation is the principal result of the magnifying regime of a temporal imaging system.

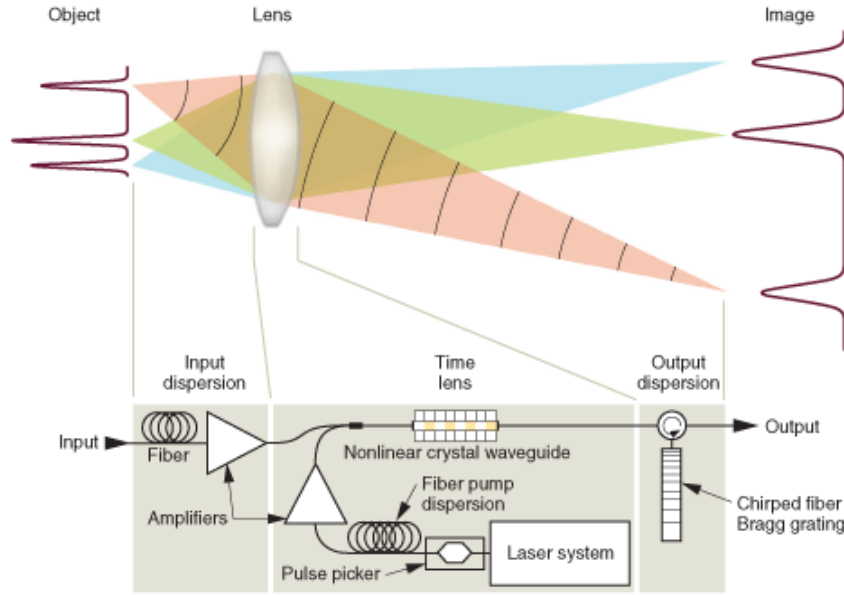


**Figure A.1:** Example of a time-lens implementation working in the magnifying regime [48].

We now focus on the condition which led to this basic result, namely:

$$\frac{1}{a} + \frac{1}{b} = -\frac{1}{c} \quad (\text{A.17})$$

Replacing the parameters a,b,c by their expressions as given by figure 2.7 results in:

$$\frac{1}{L_1 \beta_{21}} + \frac{1}{L_2 \beta_{22}} = -\frac{\omega_0}{f_T} \quad (\text{A.18})$$

which is the temporal imaging condition. This expression is completely similar to the well-known lens-law (with  $d_i$  the image distance and  $d_0$  the object distance):

$$\frac{1}{d_0} + \frac{1}{d_i} = \frac{1}{f} \quad (\text{A.19})$$

Rewriting M via the imaging condition yields an expression for M in function of the input and output dispersion parameters:

$$M = \frac{b+c}{c} = -\frac{b}{a} = -\frac{L_2 \beta_{22}}{L_1 \beta_{21}} \quad (\text{A.20})$$

Again the similarity to the spatial case  $M = -d_i/d_0$  is striking.

## A.4 Waveguide parameters

### SMF

```

pD.wl0 = 1.550e-6;           % centre wavelength [m]
pD.Aeff = 86.6e-12;         % effective area [m^2]
gamma = 1.063*10^-3;        % nonlinear coefficient [1/W/m]
D=16.7;                      % dispersion [ps/nm/km]
D=D*10^-12/(10^-9*10^3);    % dispersion [s/m/m]
S=0.06;                      % dispersion slope [ps/nm^2/km]
S=S*10^-12/(10^-18*10^3);   % dispersion slope [s/m^2/m]
pD.beta2 = -D*(pD.wl0)^2/(2*pi*c); % 2nd-order dispersion [s^2/m]
pD.beta3 = S*(pD.wl0^2/(2*pi*c))^2; % 3rd-order dispersion [s^3/m]
pD.n2 = gamma*pD.wl0*pD.Aeff./(2*pi); % nonlinear index [m^2/W]

```

**Figure A.2:** Parameters of the simulated standard single mode fiber.

### DCF

```

pDC.wl0 = 1.550e-6;         % centre wavelength [m]
pDC.Aeff = 86.6e-12;        % effective area [m^2]
gamma = 1.063*10^-3;        % nonlinear coefficient [1/W/m]
D=87;                       % dispersion [ps/nm/km]
D=D*10^-12/(10^-9*10^3);    % dispersion [s/m/m]
S=0.025;                    % dispersion slope [ps/nm^2/km]
S=S*10^-12/(10^-18*10^3);   % dispersion slope [s/m^2/m]
pDC.beta2 = -D*(pDC.wl0)^2/(2*pi*c); % 2nd-order dispersion [s^2/m]
pDC.beta3 = S*(pDC.wl0^2/(2*pi*c))^2; % 3rd-order dispersion [s^3/m]
pDC.n2 = gamma*pDC.wl0*pDC.Aeff./(2*pi); % nonlinear index [m^2/W]

```

**Figure A.3:** Parameters of the simulated dispersion compensating fiber.

### HNLF

```

pH.wl0 = 1.550e-6;         % centre wavelength [m]
pH.Aeff = 9.7e-12;         % effective area [m^2]
gamma = 0.025;             % nonlinear coefficient [1/W/m]
D=-0.08;                   % dispersion [ps/nm/km]
D=D*10^-12/(10^-9*10^3);  % dispersion [s/m/m]
S=0.026;                   % dispersion slope [ps/nm^2/km]
S=S*10^-12/(10^-18*10^3); % dispersion slope [s/m^2/m]
pH.beta2 = -D*(pH.wl0)^2/(2*pi*c); % 2nd-order dispersion [s^2/m]
pH.beta3 = S*(pH.wl0^2/(2*pi*c))^2; % 3rd-order dispersion [s^3/m]
pH.n2 = gamma*pH.wl0*pH.Aeff./(2*pi); % nonlinear index [m^2/W]

```

**Figure A.4:** Parameters of the simulated highly nonlinear fiber.

### Chalcogenide chip

```
pC.wl0 = 1.550e-6;           % centre wavelength [m]
L = 0.057;                  % waveguide length [m]
pC.Aeff = 3.4172e-12;      % effective area [m^2]
gamma = 3.5007;            % nonlinear coefficient [1/W/m]
pC.beta2 = -0.15569*1e-24; % 2nd-order dispersion [s^2/m]
pC.beta3 = 0.001878*1e-36; % 3rd-order dispersion [s^3/m]
pC.n2 = gamma*pC.wl0*pC.Aeff./(2*pi); % nonlinear index [m^2/W]
```

**Figure A.5:** Parameters of the simulated chalcogenide chip.

# Bibliography

- [1] M.A. Foster, R. Salem, D.F. Geraghty, A.C. Turner-Foster, M. Lipson, and A.L. Gaeta. Silicon-chip-based ultrafast optical oscilloscope. *Nature*, 456(7218):81–84, 2008.
- [2] M.T. Kauffman, W.C. Banyai, A.A. Godil, and D.M. Bloom. Time-to-frequency converter for measuring picosecond optical pulses. *Applied Physics Letters*, 64:270, 1994.
- [3] <http://en.wikipedia.org/wiki/Diffraction>, accessed: 2/06/2009.
- [4] P. Naulleau and E. Leith. Stretch, time lenses, and incoherent time imaging. *Applied Optics*, 34(20):4119–4128, 1995.
- [5] E. Treacy. Optical pulse compression with diffraction gratings. *IEEE Journal of quantum Electronics*, 5(9):454–458, 1969.
- [6] S.A. Akhmanov, A.S. Chirkin, K.N. Drabovich, A.I. Kovrigin, R.V. Khokhlov, and A.P. Sukhorukov. Nonstationary nonlinear optical effects and ultrashort light pulse formation. *IEEE Journal of Quantum Electronics*, 4:598–605, 1968.
- [7] B.H. Kolner. Space-time duality and the theory of temporal imaging. *IEEE Journal of Quantum Electronics*, 30(8):1951–1963, 1994.
- [8] H. Haus. Waves and fields in optoelectronics. *Prentice-Hall, Inc. Englewood Cliffs, NJ 07632, USA, 1984, 402*, 1984.
- [9] G.P. Agrawal. *Nonlinear fiber optics*. Springer, 2001.
- [10] C.V. Bennett and B.H. Kolner. Principles of Parametric Temporal Imaging-Part I: System Configuration. *IEEE Journal of Quantum Electronics*, 36(4):430–437, 2000.
- [11] Roel Baets. *Microphotonics course (taught at UGent)*. 2007.
- [12] B.H. Kolner. Generalization of the concepts of focal length and f-number to space and time. *Journal of the Optical Society of America A*, 11(12):3229–3234, 1994.

- [13] R. Salem, M.A. Foster, A.C. Turner-Foster, D.F. Geraghty, M. Lipson, and A.L. Gaeta. High-speed optical sampling using a silicon-chip temporal magnifier. *Optics Express*, 17(6):4324–4329, 2009.
- [14] J. Azaña, N.K. Berger, B. Levit, and B. Fischer. Spectral Fraunhofer regime: time-to-frequency conversion by the action of a single time lens on an optical pulse. *Applied optics*, 43(2):483–490, 2004.
- [15] K. Yamada, H. Fukuda, T. Tsuchizawa, T. Watanabe, T. Shoji, and S. Itabashi. All-optical efficient wavelength conversion using silicon photonic wire waveguide. *IEEE Photonics Technology Letters*, 18(9):1046–1048, 2006.
- [16] T.T. Ng, J.L. Blows, J.T. Mok, R.W. McKerracher, and B.J. Eggleton. Cascaded four-wave mixing in fiber optical parametric amplifiers: Application to residual dispersion monitoring. *Journal of Lightwave Technology*, 23(2):818, 2005.
- [17] TT Ng, F. Parmigiani, M. Ibsen, Z. Zhang, P. Petropoulos, and DJ Richardson. Compensation of Linear Distortions by Using XPM With Parabolic Pulses as a Time Lens. *IEEE Photonics Technology Letters*, 20(13):1097–1099, 2008.
- [18] M. Nakazawa, T. Hirooka, F. Futami, and S. Watanabe. Ideal distortion-free transmission using optical Fourier transformation and Fourier transform-limited optical pulses. *IEEE Photonics Technology Letters*, 16(4):1059–1061, 2004.
- [19] J.W. Goodman. *Introduction to Fourier optics*. Roberts & Co, 2005.
- [20] C.V. Bennett and B.H. Kolner. Aberrations in temporal imaging. *IEEE Journal of Quantum Electronics*, 37(1):20–32, 2001.
- [21] <http://www.patentstorm.us/patents/6421161/description.html>, accessed: 9/05/2009.
- [22] A.A. Godil, B.A. Auld, and D.M. Bloom. Time-lens producing 1.9 ps optical pulses. *Applied Physics Letters*, 62:1047, 1993.
- [23] T.T. Ng, F. Parmigiani, M. Ibsen, Z. Zhang, P. Petropoulos, and D.J. Richardson. Linear-distortion compensation using XPM with parabolic pulses. In *Optical Fiber Communication and the National Fiber Optic Engineers Conference, 2007. OFC/NFOEC 2007. Conference on*, pages 1–3, 2007.
- [24] P. Petropoulos, M. Ibsen, A.D. Ellis, and D.J. Richardson. Rectangular Pulse Generation Based on Pulse Reshaping Using a Superstructured Fiber Bragg Grating. *Journal of Lightwave Technology*, 19(5):746, 2001.

- [25] R. Salem, M.A. Foster, A.C. Turner, D.F. Geraghty, M. Lipson, and A.L. Gaeta. Optical time lens based on four-wave mixing on a silicon chip. *Optics Letters*, 33(10):1047–1049, 2008.
- [26] C. Rulliere. *Femtosecond laser pulses: principles and experiments*. Springer, 2005.
- [27] <http://www.orc.soton.ac.uk/viewpublication.html?pid=3591>, accessed: 9/05/2009.
- [28] R. Trebino. *Frequency-resolved optical gating: the measurement of ultrashort laser pulses*. Kluwer Academic Publishers, 2002.
- [29] <http://www.physics.gatech.edu/gcuo/Tutorial/Autocorrelation.html>, accessed: 2/06/2009.
- [30] <http://www.physics.gatech.edu/gcuo/Tutorial/FROG.html>, accessed: 2/06/2009.
- [31] D.J. Kane and R. Trebino. Characterization of arbitrary femtosecond pulses using frequency-resolved optical gating. *IEEE Journal of Quantum Electronics*, 29(2):571–579, 1993.
- [32] Michaël A.F. Roelens. PhD thesis: Precise Intensity and Phase Characterisation of Optical Telecommunication Signals, 2006.
- [33] K.W. DeLong, R. Trebino, J. Hunter, and W.E. White. Frequency-resolved optical gating with the use of second-harmonic generation. *Journal of the Optical Society of America B*, 11(11):2206–2215, 1994.
- [34] H. Stark. Image recovery: theory and application. *Orlando, FL, Academic Press, Inc., 1987, 562*, 1987.
- [35] A. Baltuska, M.S. Pshenichnikov, and D.A. Wiersma. Second-harmonic generation frequency-resolved optical gating in the single-cycle regime. *IEEE Journal of Quantum Electronics*, 35(4):459–478, 1999.
- [36] M.J.W. Rodwell, S.T. Allen, R.Y. Yu, M.G. Case, U. Bhattacharya, M. Reddy, E. Carman, M. Kamegawa, Y. Konishi, J. Puskas, et al. Active and nonlinear wave propagation devices in ultrafast electronics and optoelectronics [and prolog]. *Proceedings of the IEEE*, 82(7):1037–1059, 1994.
- [37] Jurgen Van Erps and Feng Luan. High-resolution optical sampling of 640Gb/s signals using four-wave mixing in dispersion-engineered highly nonlinear As<sub>2</sub>S<sub>3</sub> planar waveguides. *to be submitted*, 2009.
- [38] Michael R.E. Lamont, Martijn C. de Sterke, and Benjamin J. Eggleton. Dispersion engineering of highly nonlinear As<sub>2</sub>S<sub>3</sub> waveguides for parametric gain and wavelength conversion. *Optics express*, 15(15):9458–9463, 2007.



- [39] M.D. Pelusi and A. Suzuki. Higher-order dispersion compensation using phase modulators. *Journal of Optical and Fiber Communications Reports*, 3(2):90–110, 2006.
- [40] SJ Madden, DY Choi, DA Bulla, AV Rode, B. Luther-Davies, VG Ta'Eed, MD Pelusi, and BJ Eggleton. Long, low loss etched As<sub>2</sub>S<sub>3</sub> chalcogenide waveguides for all-optical signal regeneration. *Optics Express*, 15(22):14414–14421, 2007.
- [41] Michaël A.F. Roelens. Dispersion trimming in a reconfigurable wavelength selective switch. *IEEE Journal of lightwave technology*, 26(1):73–78, 2008.
- [42] Finisar. White paper: Pulse burst generation using the Waveshaper 4000E multiport optical processor. Source: [www.finisar.com](http://www.finisar.com), accessed at 26/04/2009 .
- [43] M. Pelusi, F. Luan, T.D. Vo, M.R.E. Lamont, S.J. Madden, D.A. Bulla, D.Y. Choi, B. Luther-Davies, and B.J. Eggleton. Photonic-chip-based radio-frequency spectrum analyser with terahertz bandwidth. *Nature Photonics*, 2009.
- [44] V. Ta'Eed, N.J. Baker, L. Fu, K. Finsterbusch, M.R.E. Lamont, D.J. Moss, H.C. Nguyen, B.J. Eggleton, D.Y. Choi, S. Madden, et al. Ultrafast all-optical chalcogenide glass photonic circuits. *Optics Express*, 15(15):9205–9221, 2007.
- [45] R. Adams, M. Rochette, T.T. Ng, and B.J. Eggleton. All-optical in-band OSNR monitoring at 40 Gb/s using a nonlinear optical loop mirror. *IEEE Photonics Technology Letters*, 18(3):469–471, 2006.
- [46] V.R. Almeida, C.A. Barrios, R.R. Panepucci, and M. Lipson. All-optical control of light on a silicon chip. *Nature*, 431(7012):1081–1084, 2004.
- [47] M.A. Roelens, J.A. Bolger, D. Williams, and B.J. Eggleton. Multi-wavelength synchronous pulse burst generation with a wavelength selective switch. *Optics Express*, 16(14):10152–10157, 2008.
- [48] <https://www.llnl.gov/str/June07/Bennett.html>, accessed: 2/06/2009.

# List of Figures

1.1	<b>a.</b> A spatial optical Fourier transform processor. <b>b.</b> A temporal optical Fourier transform processor. <i>M.A. Foster et al. Nature 456, 81-84 (2008)</i> [1] . . . . .	2
2.1	Duality between the assumptions for paraxial diffraction and narrow-band dispersion. [7] . . . . .	5
2.2	Diffraction of a monochromatic wave when passing through a slit [3]. . . . .	6
2.3	Narrowband dispersion causes the pulse to spread out in time with travelled distance. . . . .	8
2.4	Magnifying and Fraunhofer regime of a temporal imaging system. . . . .	9
2.5	The action of a thin lens depends on the sign of the focal distance [11]. . . . .	10
2.6	The time aperture defines the time-window through which the parabolic phase is applied. . . . .	12
2.7	Transfer-functions for dispersion and time-lens action in the time and frequency domain. . . . .	13
2.8	Set-up temporal imaging system working as a magnifier. . . . .	13
2.9	Fourier transform regime [14]. . . . .	15
2.10	<b>a.</b> Frequency-to-time regime and <b>b.</b> Time-to-frequency regime [14]. . . . .	15
2.11	Setup temporal imaging system working as a time-to-frequency converter. . .	16
2.12	An idler is generated during FWM of the pump and signal pulse[15]. . . . .	17
2.13	Space-time diagram showing aberrations due to higher order dispersion [20]. .	22
3.1	<b>a.</b> Sinusoidal phase modulation <b>b.</b> Parabolic phase modulation. [17] . . . . .	25
3.2	<b>a.</b> Experimental set-up using a EO modulator as time-lens <b>b.</b> Measurement result showing a resolution of 3 ps [2]. . . . .	26

3.3	<b>a.</b> Experimental set-up using XPM as the time-lens mechanism <b>b.</b> Determination of the operation point for the average pump power so to obey the Fourier transform and reconstruction condition[23]. . . . .	28
3.4	<b>a.</b> Input signal pulse width after varying input dispersion <b>b.</b> Signal pulse width after total set-up, showing complete compensation of the distortions caused by the input dispersion[23]. . . . .	29
3.5	Silicon-chip-based optical oscilloscope using FWM as the time-lens mechanism[1].	30
3.6	Evolution of the signal (left column) and pump (right column) in time and frequency domain before (upper 2 rows) and after (lower 2 rows) their respective dispersive elements. . . . .	31
3.7	Characterization of the record length and resolution of the optical oscilloscope by scanning a 342 fs Gaussian input signal through the record length[1]. . . .	33
3.8	Single-shot measurement of the optical oscilloscope compared with the multiple-shot cross-correlator [1]. . . . .	34
3.9	Working principle of an autocorrelator [29]. . . . .	35
3.10	The spectrogram trace of a Gaussian pulse varies according to its frequency chirp [30]. . . . .	36
3.11	Principle of sampling an optical signal by four-wave mixing with a pump pulse train of low repetition frequency [37]. . . . .	37
4.1	Temporal imaging via the FWM time-lens set-up which is investigated in this thesis work. . . . .	39
4.2	<b>a.</b> Frequency-to-time converted idler spectrum (green) reflecting the input pulse (blue) via the ideal time-lens set-up with 50 m SMF without TOD and <b>b.</b> with 50 m SMF with TOD. . . . .	42
4.3	<b>a.</b> Frequency-to-time converted idler spectrum (green) reflecting the input pulse (blue) via the ideal time-lens set-up with 50 m DCF without TOD and <b>b.</b> with 50 m DCF with TOD. . . . .	42
4.4	<b>a.</b> Evolution of a 500 fs Gaussian (blue) after 100 m DCF (green) <b>b.</b> Evolution of a 250 fs Gaussian (blue) after 40 m DCF (green). . . . .	43
4.5	Dispersive fiber length (DCF) after which TOD aberrations come into play as a function of the initial pulse width for Gaussian pulses. . . . .	44

4.6	Impact of deviating 1%, 5%,10% from the Fourier transform condition on the frequency-to-time converted idler spectrum for a <b>a.</b> super-Gaussian pulse and <b>b.</b> Sech pulse. . . . .	45
4.7	Evolution of the input and pump pulse after dispersion D and 2D respectively.	46
4.8	Spectrum signal and pump after the FWM process. . . . .	47
4.9	<b>a.</b> Normalized spectrum idler and <b>b.</b> Frequency-to-time converted spectrum idler, both reflecting the Sech shape. . . . .	47
4.10	Blue region shows the valid choice of initial $\tau_{pump}$ and $\tau_{signal}$ so that the pump and signal temporally overlap after a dispersion of respectively 2D and D. . .	51
4.11	Broadening with distance in an anomalous dispersive fiber for different signs of C [9]. . . . .	52
4.12	<b>a.</b> 1.5 ps super-Gaussian (m=2) signal (blue) and 400 fs Gaussian pump squared (green) after dispersion of respectively D and 2D in DCF <b>b.</b> Idler shape is affected by the slope of the (squared) pump pulse. . . . .	53
4.13	<b>a.</b> 2.2 ps super-Gaussian (m=2) signal (blue) and 600 fs Gaussian pump squared (green) after dispersion of respectively D and 2D in DCF <b>b.</b> Idler shape is affected by the slope of the (squared) pump pulse. . . . .	53
4.14	Degree of flatness of the pump in function of the fraction $F = \frac{\tau_{p0}}{\tau_{s0}}$ for Gaussian pulses. . . . .	54
4.15	Spectral separation signal, pump and idler. . . . .	55
4.16	Most stringent no-spectral-overlap condition for each combination of $(\Delta\lambda_s, \Delta\lambda_i)$ when $\Delta\lambda_{conversion} = 150\text{nm}$ , $\lambda_s = 1530\text{nm}$ and $\Delta\lambda_{m1} = \Delta\lambda_{m1} = 5\text{nm}$ . . . . .	56
4.17	Walkoff as a function of the center wavelength separation $\Delta\lambda$ of the pump and signal for 30 m of HNLF. . . . .	57
4.18	Design strategy for Gaussian signal and pump. . . . .	59
4.19	<b>a.</b> Multiple-bit shot configuration <b>b.</b> Single-bit shot configuration. . . . .	62
4.20	Frequency-to-time converted idler spectrum reflecting the 8-bit pulse train of a 80 Gb/s channel. . . . .	63
4.21	Frequency-to-time converted idler spectrum reflecting the amplitude modulated 8-bit pulse train of a 80 Gb/s channel. . . . .	63
4.22	Waveshaper <sup>®</sup> set-up for optimal performance of the time-lens oscilloscope. .	64

5.1	OSA Spectrum of the source Laser (Magi) directly following 1 m of SMF (dotted), then following the Waveshaper <sup>®</sup> used for pulse Shaping (black) and then following the Waveshaper <sup>®</sup> used for introducing dispersion (grey). . . . .	67
5.2	<b>a.</b> FROG measured temporal profiles of laser source directly, following the DWP without any phase or attenuation settings, following the DWP with phase compensation, and via a WDM filter <b>b.</b> FROG measured spectral profiles as outlined in (a). . . . .	68
5.3	Waveshaper <sup>®</sup> set-up. . . . .	68
5.4	Schematic representation of fourier-domain pulse shaping [42]. . . . .	69
5.5	Structure of an <i>As2S3</i> ridge waveguide[38]. . . . .	70
5.6	Walk-off for different $\Delta\lambda = \lambda_s - \lambda_p$ and for different spacing of $\lambda_s$ towards the zero dispersion wavelength at 1551 nm for 30 m of HNLF. . . . .	72
5.7	Spectrum after four-wave-mixing with signal at 1562 nm, pump pulse at 1549 nm and idler at 1536 nm. . . . .	73
5.8	Simulated spectrum of the generated idler in the first experiment. . . . .	73
5.9	Input signal and spectrum for the second experiment. . . . .	74
5.10	Spectrum after four-wave-mixing with signal at 1563 nm, pump pulse at 1548 nm and idler at 1533 nm. . . . .	75
5.11	Simulated spectrum of the generated idler in the second experiment. . . . .	76
6.1	Pump and signal temporal and spectral profiles with a dispersion D of 16 ps/nm/km for L=50 m (signal) and L=100 m (pump). . . . .	79
6.2	<b>a.</b> First derivative of the phase of the signal <b>b.</b> First derivative of the phase of the pump. . . . .	80
6.3	Comparison of the FROG and time lens oscilloscope measurement (OSA) of a 1 ps transform limited Sech pulse (theoretical). . . . .	80
6.4	Result of experiment 1 in the new set-up: the idler (blue) is a perfect reproduction of the input signal which is represented by the FROG trace (black). . . . .	81
6.5	Generated input signal by the Waveshaper <sup>®</sup> (black) and resulting idler signal (light grey) . . . . .	82
6.6	Input signal as shown by a FROG measurement (black) and the frequency-to-time converted idler spectrum (grey). . . . .	83

---

6.7	Aberrations arise for the measurement of the input 1 ps Sech pulse (black) for a variation in the slope ratio which is ideally 0.5 . . . . .	84
A.1	Example of a time-lens implementation working in the magnifying regime [48].	90
A.2	Parameters of the simulated standard single mode fiber. . . . .	91
A.3	Parameters of the simulated dispersion compensating fiber. . . . .	91
A.4	Parameters of the simulated highly nonlinear fiber. . . . .	91
A.5	Parameters of the simulated chalcogenide chip. . . . .	92